Crystal engineering and thin-film deposition strategies towards improving the performance of kesterite photovoltaic cell

Article *in* Journal of Materials Research and Technology · March 2021

DOI: 10.1016/j.jmrt.2021.03.047

CITATIONS
4

READS
277

8 authors, including:

Kelechi Nwambaekwe
University of the Western Cape
5 PUBLICATIONS **6** CITATIONS
SEE PROFILE

Penny Mathumba
Mintek
9 PUBLICATIONS **56** CITATIONS
SEE PROFILE

Sodiq Tolulope Yussuf
Olabisi Onabanjo University
15 PUBLICATIONS **17** CITATIONS
SEE PROFILE

Onyinyechi Uhuo
University of the Western Cape
5 PUBLICATIONS **5** CITATIONS
SEE PROFILE

JOURNAL OF MATERIALS RESEARCH AND TECHNOLOGY 2021;12:1252–1287

Available online at www.sciencedirect.com

jmr&t Journal of Materials Research and Technology

journal homepage: www.elsevier.com/locate/jmrt

Review Article

Crystal engineering and thin-film deposition strategies towards improving the performance of kesterite photovoltaic cell

Kelechi C. Nwambaekwe[*], *Vivian Suru John-Denk*[**], *Samantha F. Douman, Penny Mathumba, Sodiq T. Yussuf, Onyinyechi V. Uhuo, Precious I. Ekwere, Emmanuel I. Iwuoha*[***]

University of the Western Cape Sensor Laboratories (SensorLab), 4th Floor Chemical Sciences Building, Robert Sobukwe Road, Bellville, 7535, Cape Town, South Africa

ARTICLE INFO

Article history:
Received 21 December 2020
Accepted 14 March 2021
Available online 23 March 2021

Keywords:
Alloying
Bandgap
Chalcogenides
Crystal lattice
Photovoltaics

ABSTRACT

With high absorption coefficient (10^4 cm^{-1}), optimal bandgap (~1.5 eV), low toxicity and the abundance of its constituent elements, kesterite (Cu_2ZnSnS_4 or CZTS) displays the properties of an ideal photovoltaic material. Kesterite is structurally analogous to chalcopyrite (Cu_2InGaS_2 or CIGS) and can thus be produced through the already established techniques for the synthesis of commercial CIGS. Though CIGS- and CdTe-based thin-film solar cells have attained levels of power efficiency values (up to ~22%) that compare with that of crystalline silicon-based wafer solar cell, they contain rare earth elements (indium, tellurium and Cd) that are toxic. This article reviews the crystal structure formation and properties of CZTS. Material synthesis, thin-film deposition methodologies and different layers that have been developed for kesterite-based photovoltaic (PV) cell are reported. Factors that hinder high-power conversion efficiency, including large open-circuit voltage deficit ($V_{oc,def}$), are discussed. Strategies, such as alloy formation, which have been employed to overcome the limitations of using kesterite in PV cell applications are presented, together with the future direction in the quest for improving the performance of kesterite PV cell devices.

* Corresponding author.
** Corresponding author.
*** Corresponding author.
E-mail addresses: 3705852@myuwc.ac.za (K.C. Nwambaekwe), 3377067@myuwc.ac.za (V.S. John-Denk), eiwuoha@uwc.ac.za (E.I. Iwuoha).

https://doi.org/10.1016/j.jmrt.2021.03.047

1. Introduction/Background

The earliest work on solar cell was in the year 1839. Edmond Becquerel experimented with two metal plates (later identified to be copper-cuprous oxide thin-film solar cell) drenched in a fluid. He found that these metals were capable of discharging a consistent current when shone with sunlight. In 1870s, Willoughby Smith et al. discovered photovoltaic impact in selenium [1]. Some years thereafter, C.E. Fritts put a sheet of amorphous selenium on a metal support, holding the selenium in place with a transparent thin layer of gold [1]. He explained that the selenium clusters produced current that were continuous, steady and of significant force when sunlight was shone on it. At this point in time, there was a lot of distrust for his assertions of converting solar energy to electrical energy. To prove the veracity of his findings, he sent his sample to Werner Siemens in Germany (reputable specialists in electricity at that time) who confirmed his assertions'. In any case, the efficiencies of the amorphous selenium and copper-cuprous oxide were less than 1% [2]. The advent of quantum mechanics boosted the recognition of single-crystal semiconductor, shedding more light to p/n junction behavior. In the year 1954, Chapin et al. found, designed and produced a single crystal silicon solar cell with 6% efficiency [2,3]. This efficiency was improved on few years after to 15%. This breakthrough was significant as solar cell provided a light weight low-support remote electric power source for Sputnik which was launched in 1957. In recent times, silicon solar cells are used for powering space station.

Growing concern due to the depleting nature and the environmental impact of the use of fossil fuel energy has led to research poised towards sustainable and environmentally friendly energy sources. Renewable energy sources such as hydropower (accounts for 70% of global renewable energy source) [4,5], wind, biomass, and solar energy have been explored as alternatives to fossil fuel [6–10]. It has been reported that solar energy when harnessed, would produce in a day the total amount of energy generated globally in a year [11,12]. This raises the call to evaluate materials that would efficiently absorb solar energy and convert them into other useful energies. Since its intensively researched usefulness in solar cell application, silicon has seen wide range of application in this field [13,14]. Si photovoltaic (PV) modules dominate the industry accounting for over 90% of globally produced PV modules.

There are some downsides to the use of Si solar cells. As an indirect bandgap material, Si solar cells allows less space for modification of parameters that can enhance its performance. It also requires a thick layer of around 180–300 μm to absorb photons and has almost reached its theoretical efficiency limit [11,12,15–18]. These drawbacks makes the production of Si solar cells expensive which has led to intensified efforts at researching thin-film solar cell materials that are less expensive than Si solar cells. Environmentally friendly and efficient materials are needed to take care of the clean energy supply issues as the conventional energy sources (coal and crude oil) are being restricted for use and will run out soon. Solar cell production has seen three generational stages. The first generation is cost and energy intensive which involves single and multicrystalline (mc) Si solar cells which are produced on a wafer bearing either single crystal or crystal grains [19]. The power conversion efficiency (PCE) of a single crystal Si solar cell is at 25% while that of multicrystalline Si solar cell is 21% [20]. The second-generation solar cells comprises of an amorphous silicon (a-Si), mc-Si, CdTe and CIGS thin-films. The PCE of CIGS and CdTe are 18% and 21% respectively [20]. The PCE of a-Si and mc-Si thin films are 10% and 11% respectively [20]. Although the second-generation solar cells show less efficiency than their predecessor, they are advantageous for their less expensive, easy to integrate in housing and very flexible for use in adaptable substrates [19]. The convenience of the adaptable and portable nature of thin-film solar cells can be seen in Fig. 1 where a compact solar cell panel is used to charge a cell phone. The third-generation of solar cells comprises of nanocrystal solar cells, organic solar cells, hybrid (organic and inorganic) solar cells, dye synthesized solar cells, perovskites and kesterite solar cells. This generation of solar cells are novel advances known to be cost and energy effective and suitable for adaptable substrates but are marred by lower PCE values and instability as is the case with organic and perovskite solar cells thereby hindering their commercialization. If these issues can be improved on, this generation of solar cells can greatly rival the already commercialized solar cells as they will less expensive [20].

Thin films (Fig. 2) provide suitable pathway for electrical energy delivery from solar energy. They can easily be set up in forest regions, solar fields, traffic and road light etc. and they cost less when compared to the more established silicon wafer cells [22].

Figure 3 above shows the scheme of the cross-section of a thin film solar cell. The structure and working principle of a thin-film solar cell is same as that of a Si wafer cell, only differing in the flexible thin arrangements of the different layers and the type of absorber layer material used [23]. The fundamental component of a PV cell is the semiconductor

Fig. 1 – Flexible thin-film solar panel charging an iPhone 4S mobile device.

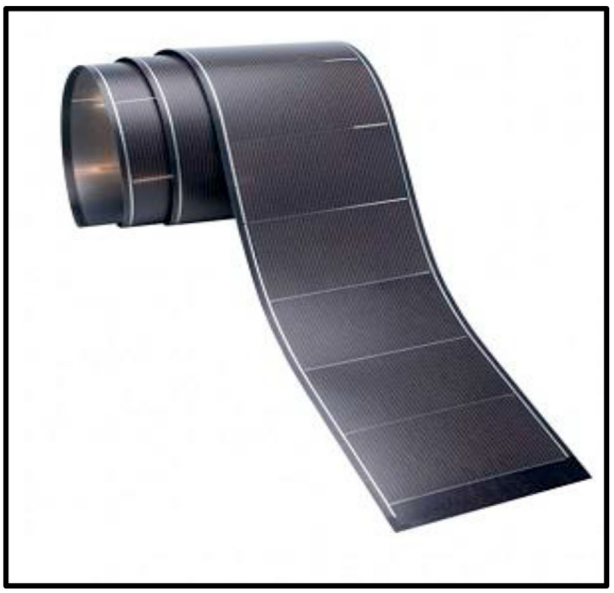

Fig. 2 – Thin-film solar cell illustrating its adaptability and flexibility [21].

materials (Fig. 4). A p-type semiconductor is formed when a silicon, gallium or indium is doped with a trivalent element like boron B. Holes (positive charge carriers) are the major charge carriers in this type of semiconductor.

For n-type semiconductors, electrons are the major charge carriers. They carry negative charges. They are formed when silicon or any other semiconductor is doped with a pentavalent element like phosphorus, P or antimony, Sb. The n-type and the p-type join together to shape a PV cell. In the absence of the light source, few atoms are energized and move over the junction. This causes a slight drop in voltage at the junction. As the light source is introduced, more molecules become energized leading to a huge current at the output. The current produced can be stored in rechargeable battery and used for several applications [23]. The old solar panel innovation uses Si semiconductor for the generation of the p-type and n-type layer. In relation to thin-film layer solar cells, the Si semiconductor materials are replaced by either CIGS or CdTe [19].

2. Types of thin-film solar cells

The first generation of PV cells were based on monocrystalline and multicrystalline silicon with indirect energy bandgap of 1.12 eV advantageous in the production and preparation of high purity Si wafers. For an mc-Si solar cell, the first reported (in the year 1941) PCE value was around 1% [24]. Since then, the efficiency of the mc-Si solar cell has grown exponentially almost reaching its theoretical maximum of about 32%. By 2014, the efficiency of 25.6% was reached via a single-crystalline Si cell [25]. An efficiency of 21.25% was recorded for mc-Si cells by Trina Solar group in late 2015 [26]. Si-based solar cells dominate the PV industry, having almost 90% of all innovations, yet the cost of electrical energy produced by the PV cell is still high when compared to other sources. The major contributing factor to the high cost of Si solar cells is the use of large amount of material (usually Si-wafers which is almost 90% of the cost) [27]. Si solar cells have low absorption coefficient (~10^2 cm^{-1}) and requires large amount of the wafers (about 100–200 μm) to absorb photons. Strategies were adopted to find ways to reduce the thickness of these wafers and at present, ~180 μm thickness has been achieved. Other materials and techniques have been explored to minimize the cost of production of PV cells. Producing thin-film materials that can be adopted in PV cell has emerged the most consequential in reducing the cost of PV cells which has led to the successful birth of some second-generation PV devices. The overall thickness of these thin-film devices are in few microns and these materials are also characterized by direct bandgaps with high absorption coefficient. These devices are manufactured on inexpensive substrates (e.g., glass, plastic, metal foils) and their synthesis procedures does not require high

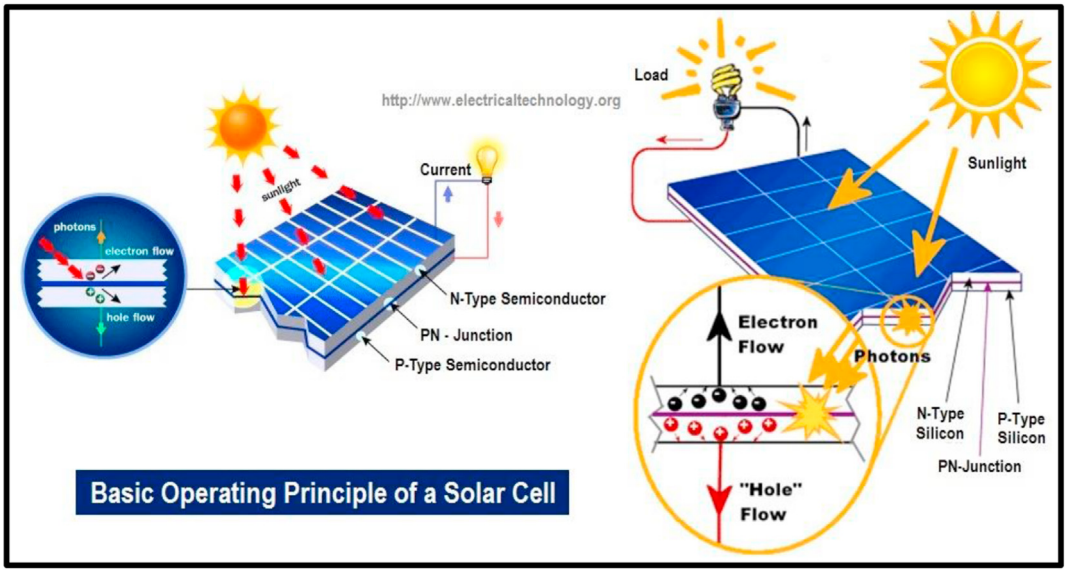

Fig. 3 – Schematic cross-sectional illustration of a silicon solar cell [23].

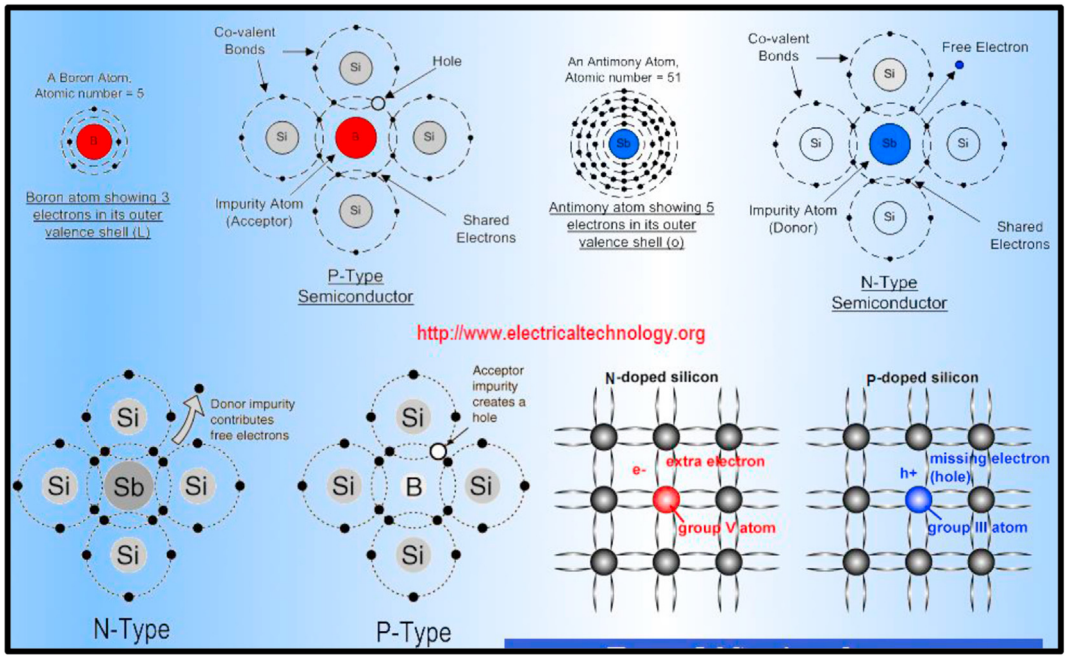

Fig. 4 – Types of semiconductor materials [23].

level of purity as is the case of Si cells. In this way, the synthesis procedures and various deposition methods are less difficult and more affordable. Thin-film solar cells depend for the most part on heterojunctions of doped unique materials where normally, a thin n-type semiconductor as a buffer layer is deposited over a p-type semiconductor, which represents the effective absorber layer to frame the p-n intersection (junction). A p-type material is favored for the effective absorbing layer, where the electron hole-pairs (EHPs) are generated, in light of the fact that the diffusion length of electrons in a p-type semiconductor is bigger than the diffusion length of holes in an n-type semiconductor. The n-type layer must be thin and made of a wide-band material to enable the incident light to go through to the absorber layer. For that, a CdS layer around 50 nm thick with energy bandgap of 2.4 eV is normally utilized. Two strong delegate materials for thin-film solar cells that show device efficiencies practically identical to those of mc-Si cells are cadmium telluride (CdTe) and copper indium-gallium diselenide, $Cu(InGa)Se_2$ (CIGS). These two materials have gotten to commercialization point for large scale manufacturing. Also, amorphous silicon (a-Si) solar cells are mass produced. Regardless of a-Si devices' low efficiency contrasted with CdTe and CIGS cells, they have application because of their minimal cost of production where low efficiencies are acceptable [19].

2.1. *Amorphous silicon (a-Si)*

Amorphous silicon (a-Si) thin films are deposited through plasma-enhanced chemical vapor deposition (PECVD) at low temperatures with silane (SiH_4) gas [28]. They can be deposited on substrates such as glass, plastic or metal foils. The amorphous nature of the material entails an arbitrary arrangement which impacts its electronic properties. In order to enhance the quality of the material, hydrogen is used to passivate bonds that emanate from the irregular arrangement of the atoms. The hydrogenated amorphous silicon (a-Si:H) has bandgap value of 1.7 eV with absorption coefficient of ~10^5 cm^{-1}, which allows for a broader absorption of solar radiation in few micrometers. Initial PCE obtained for an a-Si:H solar cell with a thickness of 1 μm was 2.4% with cell architectural arrangement of p-I-n structure [29]. The device can be made into a single- or multi-junction with a superstrate (p-I-n) setup meaning that light enters through the substrate or n-I-p substrate where the light enters through the top n-layer. Figure 5 shows the cross-sectional illustrations of single and multijunction a-Si p-I-n superstrate setup. Thin-film solar cells that are based on a-Si:H suffer drawbacks of low performance due to Staebler-Wronski effect (SWE) when exposed to sunlight [30]. Through years of intensive research studies on stabilization of the cell, a record efficiency of about 10.2% [31] has been recorded for a stabilized single junction a-Si:H PV cell. For multijunction stabilized a-Si:H cells, a PCE of 13.6% has been recorded [32].

2.2. *Cadmium telluride (CdTe)*

Cadmium telluride (CdTe) stands as a contender for thin-film PV applications as it is a chemically stable semiconductor material with broad absorption coefficient of ~10^4 cm^{-1} and direct bandgap of 1.45 eV [34]. It can be doped as p- or n-type semiconductors but for the device, it is used as a p-type semiconductor. Usually, the device takes a superstrate architecture where a transparent conducting oxide (TCO) as front layer is deposited on a glass substrate, followed by n-type cadmium sulfide (CdS) layer which acts as the window layer. The absorber layer, CdTe is then deposited as the p-type semiconductor forming the p-n junction with the cadmium sulfide layer. The CdTe absorber layer is deposited at temperatures between 400 °C and 600 °C through distinctive

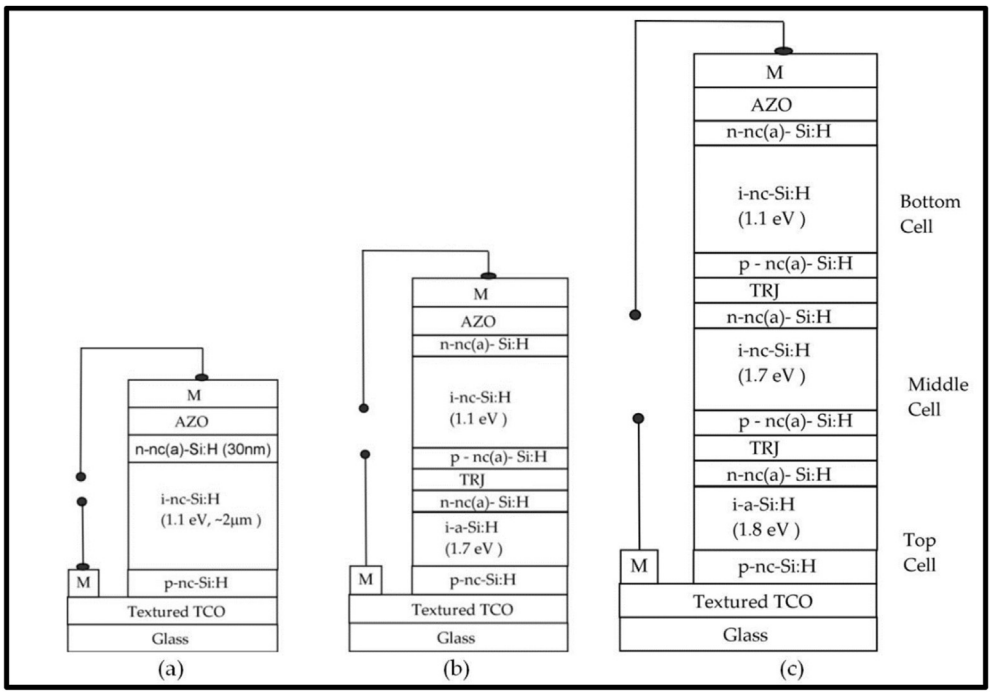

Fig. 5 – Schematic diagram of (a) single p-i-n type (b) double junction, (c) triple junction solar cell, where M stands for metal electrode [33].

deposition routes such as close-spaced sublimation (CSS); a type of thermal evaporation technique, electrodeposition technique, sputtering and screen printing [35,36]. Finally, a metal film as the back contact is deposited on the CdTe layer. Figure 6 illustrates the architecture of a conventional CdTe/CdS PV cell. The PCE of CdTe-based solar cells has expanded through the years reaching over 20%. First Solar announced in a press statement in 2016 to have achieved a world record of 22.1% PCE value for CdTe cell [37]. These advancements makes CdTe a good contender to mc-Si- wafer cells having low cost of production and high efficiency devices. The major drawbacks for the cells are the toxicity of cadmium and the shortage of tellurium which could adversely affect terawatt (TW)-scale generation in future resulting in increased cell and module costs.

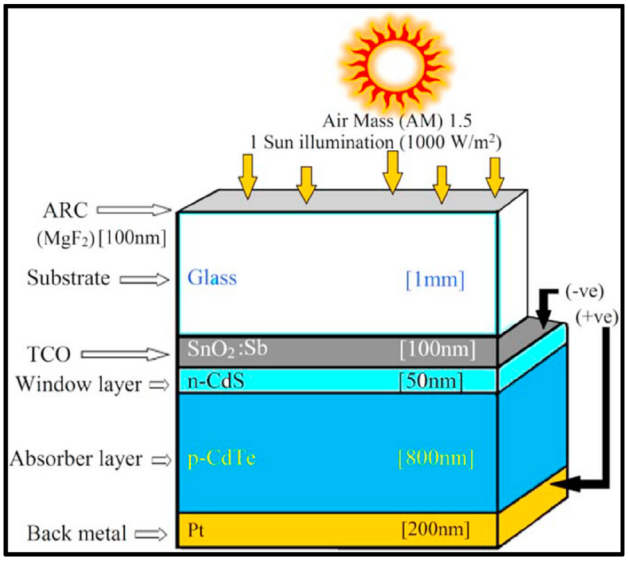

Fig. 6 – Conventional architecture of CdTe/CdS superstrate solar cell [38].

2.3. *Copper indium gallium sulfide (CIGS)*

Semiconductors such as copper indium diselenide ($CuInSe_2$), copper indium gallium diselenide ($CuIn_xGa_{1-x}Se_2$) and copper indium disulfide ($CuInS_2$) belonging to group of materials referred to as chalcopyrites show direct bandgaps (1.5 eV) and high absorption coefficient (~10^5 cm^{-1}) making them suitable for PV application. The possibility of a CdS/$CuInSe_2$ heterojunction PV framework was first explored in 1974 [39] and the first thin-film based on this heterojunction PV framework was obtained in 1976 by Kazmerski et al. with PCE value of 4.5% [40]. Thereafter, gallium (Ga) was incorporated to form a quaternary compound of copper indium gallium selenide (CIGS). CIGS is the best chalcopyrite PV cell with record PCE of 21.7% [41]. Different deposition techniques have been explored for CIGS absorber layer deposition such as sputtering, electrodeposition, spray deposition and thermal evaporation. CIGS absorber layer of the device with best record PCE value was deposited via thermal evaporation [41]. Figure 7 shows the cross-sectional design for conventional CIGS PV cell which follows the substrate architecture. The cell design entails firstly, the deposition of molybdenum (Mo) layer as the back contact unto a glass substrate, followed by the deposition of the CIGS absorber layer which serves as the p-type semiconductor. Thereafter, the n-type CdS buffer layer is deposited completing the p-n heterojunction. An intrinsic Zinc oxide (i-ZnO) layer is deposited unto the CdS buffer layer followed by

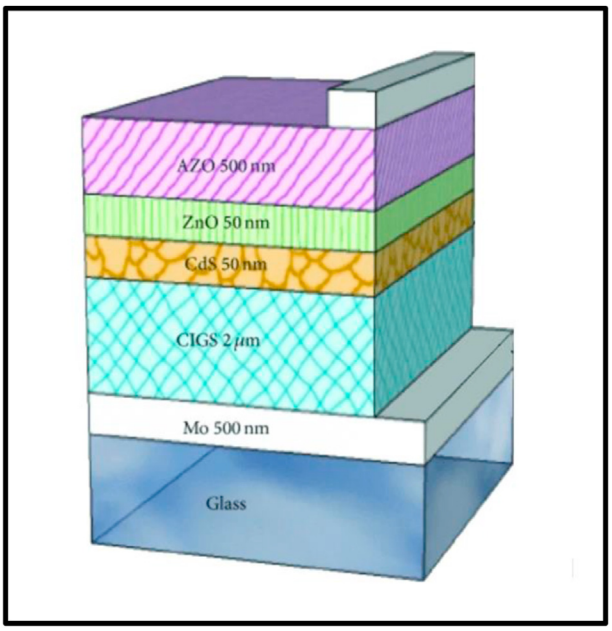

Fig. 7 – Cross -sectional architecture of a conventional of CIGS solar cell [42].

the deposition of aluminum doped zinc oxide (Al:ZnO) to form the top contact. This device with its remarkable innovations and PCE values suffers the drawback of being comprised of rare earth high-cost indium (In), thereby impacting the cell and module cost. This can lead to shortage of these devices in the near future.

3. CZTS/Se semiconductor materials

Copper zinc tin sulfide/selenide, CZTS/Se conventionally known as kesterite was discovered in Russia as a mineral containing iron and zinc in differing ratios [43,44]. This material has been researched and found to exhibit remarkable p-type semiconductive properties [43]. As a semiconductor material it exhibits great optical and electronic properties similar to that of CdTe and CIGS with optimal energy bandgap value of 1.5 eV and broad absorption coefficient of ~10^4 cm^{-1} making it a suitable absorber layer material for thin-film PV application. It is a great substitute for CIGS and CdTe as all its constituent elements are earth abundant and non-toxic [45,46]. This advantage of earth abundant and non-toxic composition gives the material a commercialization edge over the other PV devices. Earliest work in the application of CZTS materials for PV was demonstrated by Katagiri et al. through vacuum-based evaporation technique with a PCE value of 0.66%. There has been remarkable improvements in the PCE values of this material since its PV application. A PCE value of 8.4% has been achieved for CZTS devices, 11.6% for CZTSe devices and more than 10% for sulfur-selenide CZTSSe devices. The highest PCE record of 12.6% was reported for the material was reported for solid solution of CZTSSe PV devices by a group at IBM [47]. The semiconductors: CZTS and CZTSe and their alloys CZTSSe, have drawn intensive attention as the light-absorber materials in thin film solar cells since 2010 [48,49]. Both CZTS and CZTSe belong to the group I_2–II–IV–VI_4 quaternary compound semiconductors. Following theoretical material design, quaternary compounds of I_2–II–IV–VI_4 where the anions and cations are of tetrahedral coordination, can be structured via two-step cation substitution from II–VI binary compounds in the zincblende structure with tetrahedral coordination [48] as depicted in Fig. 8. For example, the zincblende-structured ZnS mutates into the chalcopyrite-structured $CuInS_2$ through replacing two Zn by one Cu and one In, and the chalcopyrite-structured $CuInS_2$ further mutates into the kesterite-structured CZTS through replacing two In by one Zn and one Sn, giving the mutation from binary compound semiconductors to the quaternary compound semiconductors. By choosing different component elements, a series of I_2–II–IV–VI_4 quaternary compounds can be derived. The mutation derivation of new ternary and quaternary compound semiconductors is also possible from the III–V semiconductors such as GaN and GaP, from recently designed series of new nitrides and phosphides [50].

4. Properties and limitations of CZTS/Se

4.1. *Properties of CZTS/Se*

The first synthesis and analysis of single crystal of CZTS was achieved in 1967 [52]. Not much relevance was given to the findings of that study until recently in 2007 when government subsidies were released towards research into new materials for solar energy, as this period saw a huge price hike in highly pure polycrystalline silicon PV cells. Since then, the investigations of CZTS properties has been based on their crystalline, optical-electrical and size control morphological properties. Here we discuss the findings and highlight the advantages as well as limitations of the materials in relation to their application for PV cell purposes. Given the formation route from binary II–VI semiconductors to I_2–II–IV–VI_4 quaternary semiconductors as described in Fig. 8 with zinc blende and wurtzite structures [48], the crystal structures of these I_2–II–IV–VI_4 semiconductors also take the zinc blende or wurtzite crystal structures of these II–VI binary semiconductors as seen in Fig. 9 [53]. Through the octet rule, two ternary structures such as chalcopyrites and CuAu-like can be

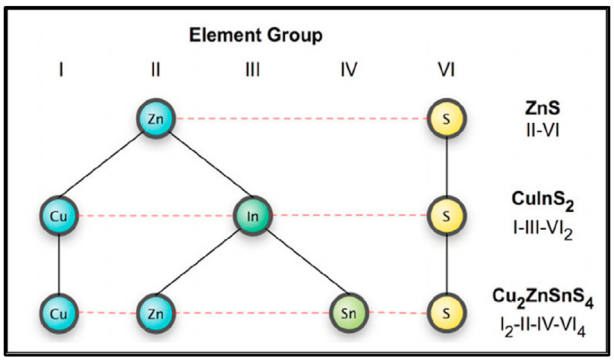

Fig. 8 – Link between binary, ternary and quaternary semiconductors to give CZTS. Reproduced with permission [51]. (Copyright John Wiley & Sons).

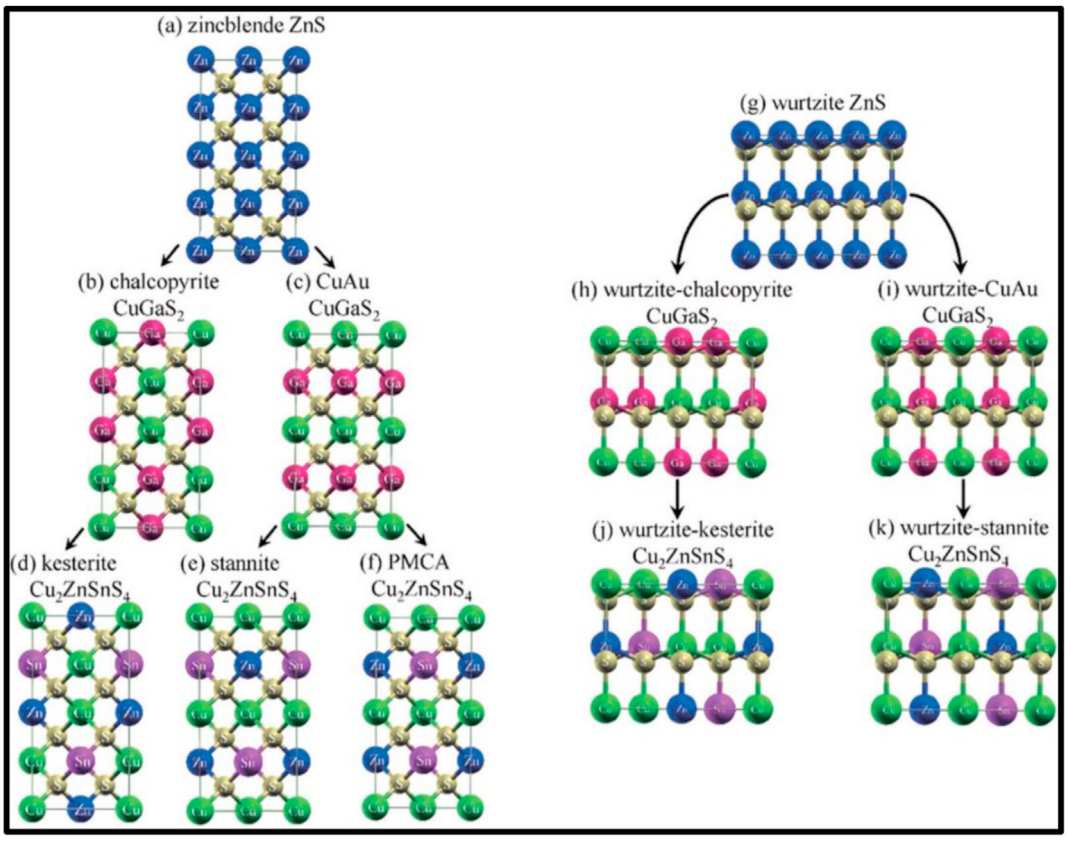

Fig. 9 – The crystal structure mutation from (a) zinc blende ZnS to (b) chalcopyrite $CuGaS_2$ and (c) CuAu-like $CuGaS_2$, then to (d) kesterite Cu_2ZnSnS_4, (e) stannite Cu_2ZnSnS_4, and (f) PMCA-Cu_2ZnSnS_4, and the mutation from (g) wurtzite ZnS to (h) wurtzite-chalcopyrite $CuGaS_2$ and (i) wurtzite-CuAu $CuGaS_2$, then to (j) wurtzite-kesterite Cu_2ZnSnS_4 and (k) wurtzite-stannite Cu_2ZnSnS_4 [53,65].

derived from the zincblende crystal structure [53,54]. The chalcopyrites and CuAu further forms the quaternary crystal structures of kesterite and stannite, respectively [53,54]. CZTS and related semiconductor materials exist in these zincblende and CuAu derived kesterite and stannite phases [54]. The kesterite and stannite phases are of body-centered tetragonal modifications showing space groups of *I*4: no.82 and *I*42m: no 121, respectively [54]. They are referred to as pseudocubics commonly described as two sulfur face-centered cubic (FCC) lattices which are stacked on each other with Cu, Zn and Sn filling up half the tetrahedral voids of the FCC lattice. The major difference in these two structures arises from the way these cations are stacked in the structures. With the kesterite structure, the stacking starts with two alternating cation layers which contain Cu and Zn or Cu and Sn. While the stannite structure consists of a layer of Cu alternating with a layer of Zn and Sn. Also, the Zn and Sn atoms on the same layer in the stannite structure switch their positions in every other layer. The chalcogens in these structures also present some unique assumptions. When looking at the accessible information on x-ray diffraction on CZTS and CZTSe from the International Council on Diffraction Data (ICDD), it present the idea that the sulfide compound crystalize into the kesterite structure, while the selenide compound occurs in stannite structure. As X-ray diffraction cannot be used to sufficiently differentiate both structures as it is limited in differentiating the Cu and Zn molecules, neutron measurements can collaborate with the cores and can recognize Cu and Zn molecules [55]. In an exhaustive neutron diffraction investigation of different $Cu_2ZnSn(S_{1-x}Se_x)_4$ compounds, it was demonstrated that the sulfide and additionally the selenide occur in the kesterite structure, not in the stannite structure [55]. There is also the crystal structure mutation into the wurtzite structure. As seen in Fig. 9 (g, h, i, j and k), the binary wurtzite structure leads to the formation of two ternary wurtzite structures which in turn forms two quaternary wurtzite structures. For CZTS materials, the quaternary wurtzite structures are named based on the most stable state in relation to their zincblende derivations. For instance, if the stannite state is more stable, then the structural name becomes wurtzite-stannite while if kesterite state is more stable it becomes wurtzite-kesterite [56]. From theoretical estimations of total energies of the new quaternary structures, the kesterite structure has low energy than the other structures which has been elaborated by the Madelung energy and strain energy of kesterite structures in CZTS, CZTSe and other derived quaternary semiconductor materials. As a result of the already established thermodynamic stability, kesterite is the phase mostly desired and applied in PV devices.

The kesterite $Cu_2ZnSn(S_{1-x}Se_x)_4$ semiconductor offers a high absorption coefficient and tunable band gap energy. The absorption coefficients α of the CZTS-based kesterite semiconductor are as high as 10^4–10^5 cm^{-1} [57]. Taking at least $\alpha = 10^4$ cm^{-1} and 2.5 μm thick, CZTS film can absorb in excess of 90% of the incident light without reflection losses. The bandgap of kesterite can be tuned from 1.0 eV at $x = 1$–1.5 eV at $x = 0$ [57]. Estimation of the electronic band structure of CZTS reveals an immediate bandgap at the gamma point of the Brillouin zone [58]. The bandgap has been hypothetically computed via density functional theory calculations in various approximations [54,59–62]. Every single forecast for the kesterite structure concurs immensely with the hypothetically bandgaps, though the bandgaps in stannite structure are around 100 meV lower [63]. The extent of the bandgap of CZTS can be explained by the chemical behavior of the valence and conduction band states, and specifically, the low binding energy of the filled Cu 3d valence band [64]. For all Cu-based chalcogenides, including the quaternary kesterite and ternary chalcopyrite compounds, the valence band maximum (V_{BM}) is an antibonding condition of the anion p and Cu d orbitals [60]. Since the valence p level of S has less value of energy than Se, the V_{BM} of the sulfide CZTS is lower than that of the selenide CZTSe. In any case, valence band offset (V_{BO}) between the sulfide CZTS and selenide CZTSe is very little (<0.2 eV), lower than that of ZnS and ZnSe (~0.52 eV [120]). This distinction is from p-d hybridization in Cu-based chalcogenides on the grounds that the hybridization is more grounded in the shorter Cu–S bond and pushes the antibonding V_{BM} level of the sulfide up in respect to that of the selenide. The conduction band maximum (C_{BM}) is comprised of a solitary band beginning from the Sn 5S and the S or Se p orbital [64].

The regular band arrangements, ascertained with reference to the energy contrast of deep atomic-like center states over the kesterite/CdS heterojunction [66], are plotted in Fig. 10. Contrary to silicon, where either particle of phosphorus or boron is deliberately doped to deliver n-type and p-type semiconductors, respectively, CZTS-based materials are self-doped through the formation of characteristic, interstitial

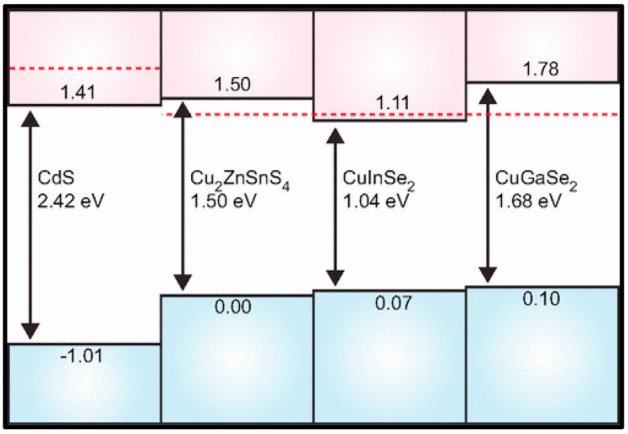

Fig. 10 – The estimated band arrangements for CdS, CZTS, CZTSe, $CuGaSe_2$ and $CuInSe_2$. CdS acts as n-type window layer [75].

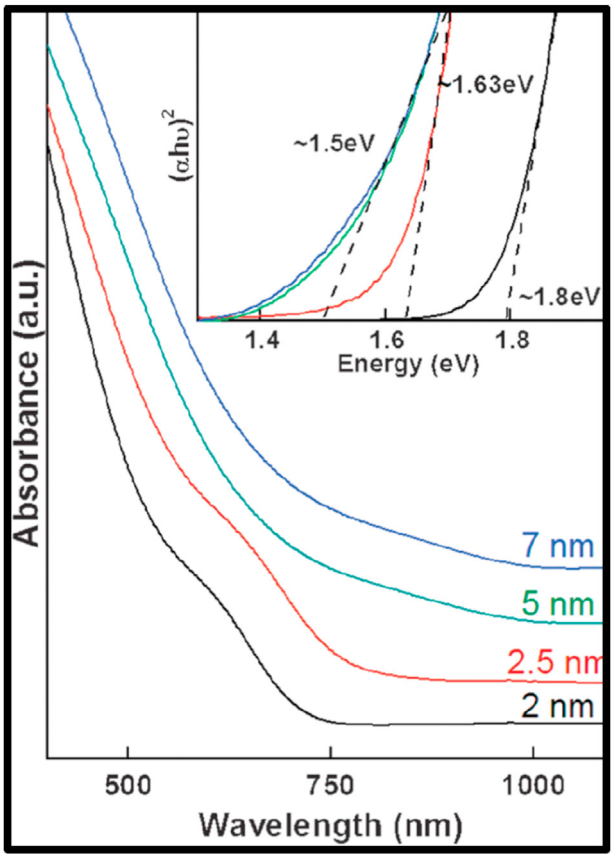

Fig. 11 – The UV–Vis–NIR absorption measurement CZTS nanoparticles with different size. The inset displays the Tauc plot for the corresponding absorbance curves. Reproduced with permission [77] (Copyright Royal Society of Chemistry RSC).

and antisite deformity at the time of their growth [67]. The formation energies of most acceptor deformity are lower than those of the donors clarifying the experimentally observed p-type conductivity and indicates that n-type doping in these compounds will be problematic. In any case, the least energy defect is Cu_{Zn} antisite, which is not quite the same as $CuInSe_2$ where the dominant deformity is the Cu vacancy (V_{Cu}) [68]. This Cu_{Zn} antisite defects infers a more profound contributor level than V_{Cu} in the bandgap of CZTS and causes huge bandgap energy decrease, which is negative for CZTS solar cell efficiency. Hence, it is important to reduce the formation energy and improve the population of shallow V_{Cu} relative to Cu_{Zn} via copper-poor and zinc-rich composition. The hole density of typical kesterite materials is around 1016 cm^{-3} [69–71], which is characteristic of CIGSe in high efficiency CIGSe solar cells. Hole density of 1018–1019 cm^{-3} also has been reported [72–74], due to the presence of $Cu_xS(e)$ secondary phases leading to the films being useless degenerate semiconductor.

Size and shape are two vital parameters for nanoparticles because they give information in relation to the properties of the nanoparticles. An important example can be cited from CdSe nanocrystals where the absorption edge of CdSe nanocrystals blue shifts as the size increases from 17 Å to 150 Å,

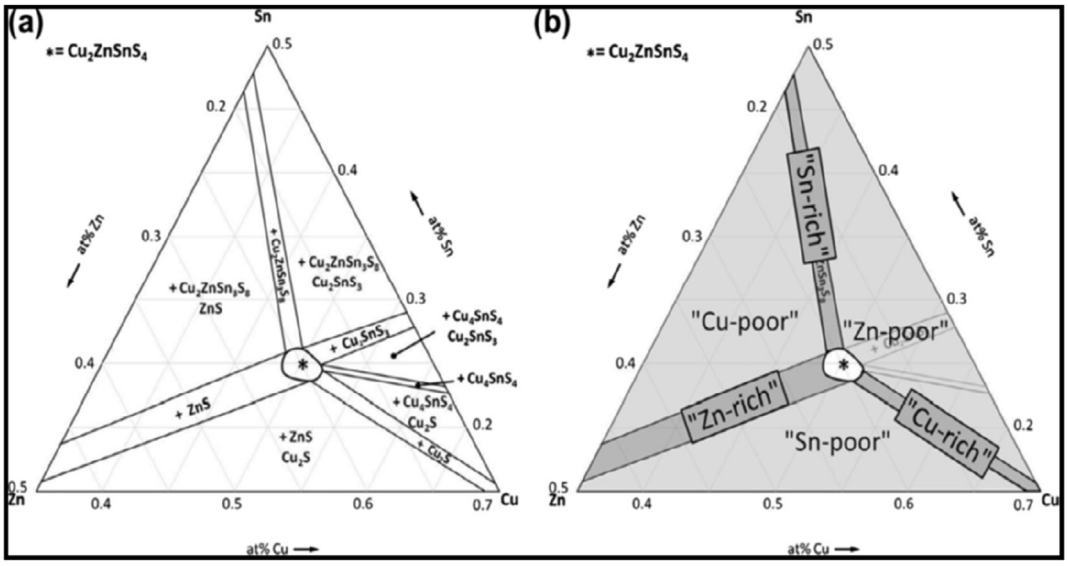

Fig. 12 – (a) Phase diagram of the formation of CZTS alongside expected secondary phases (b) Phase diagram with hints of possible secondary phases in relation to composition conditions. Reproduced with permission [93]. (Copyright Elsevier).

showing a decrease in the energy band gap [76]. The size control of CZTS nanoparticles by tuning the amount of oleylamine and adjusting the reaction temperature was revealed by Khare et al. [77]. In their work, the Cu, Zn, and Sn diethyl dithiocarbamate complexes were used as the metal precursors. The HRTEM micrographs analysis of their work shows that the synthesized CZTS nanoparticles had sizes of 2 nm, 2.5 nm, 5 nm and 7 nm. The optical absorption of the UV–Vis–NIR absorption measurement of CZTS nanoparticles with crystal size corresponding to the different sizes obtained is shown in Fig. 11. The band gaps are estimated based on the $(\alpha h\nu)^2$ vs. $h\nu$ plot in Fig. 11 to be 1.8 eV (2 nm), 1.63 eV (2.5 nm), 1.5 eV (5 nm) and 1.5 eV (7 nm) respectively. The higher band gap energy than the usual 1.5 eV for particles size of 2 nm and 2.5 nm provides the evidence for quantum confinement. Beside kesterite structure, CZTS can also form wurtzite structure. Several research groups have disclosed the synthesis of wurtzite structures. Lu et al. prepared wurtzite CZTS nanoparticles in nanoprisms and nanoplates shape [78]. Singh et al. was able to form mono-dispersed wurtzite CZTS nanorods [79]. The size and shape control of CZTS wurtzite are easier than the kesterite phase, which is due to slow reaction dynamics for the formation of wurtzite structure.

4.2. *Limitations of CZTS/Se*

Kesterite shows properties that highlights its potential for PV application as it possesses optimal direct bandgap value of 1.5 eV, composition of earth abundant and non-toxic elements, but some critical factors are limiting the material from reaching its full potential [80–82]. Any change in the structural, compositional, microstructural, optical, and electrical properties can cause huge impact on the performance of the kesterite PV device as these properties are very much connected to each other [83–85]. This means that the amount of chalcogen in the kesterite material affects its optical properties. Bandgap which is derived from optical properties is affected by the additions of sulfur and selenium in the kesterite material. An increased amount of sulfur expands the bandgap value of the kesterite material while the addition of selenium narrows it [85,86]. Increased crystallinity which can be achieved through the annealing process, improves the optical properties. Major backdrops of the kesterite material during its fabrication and synthesis are the formation of secondary phases and structural defects [82,87]. There is also the case of the interfacial defects at the device level.

From calculated equilibrium space as seen in Fig. 12a, a single phase kesterite formation occupies a small region (middle) in the phase diagram [66,88–90]. This is a major factor that must be considered in the fabrication or synthesis of the kesterite material. This plays into why there is a high probability for the formation of secondary phases alongside the kesterite phase during fabrication/synthesis of the kesterite absorber layer [82,91,92]. To get a high efficiency for the kesterite PV device, a copper poor and zinc rich composition is ideal [81]. With the small region occupied by kesterite in the phase diagram, it becomes extremely difficult to obtain with this ideal composition, a single phased kesterite absorber layer without the interference or formation of secondary phases [81,84,85].

From the phase diagram in Fig. 12b, the condition of the chemical composition of the fabricated or synthesized kesterite results in the formation of peculiar secondary phases as depicted in Fig. 12a. If there is a Cu-rich situation, it will result in the formation of Cu_2S secondary phase. Care is to be taken not to deviate from the middle region as any slight deviation will lead to the formation of any of these secondary phases; ZnS, Cu_2S, or Cu_2SnS_3 to name a few [86].

A hypothetical estimation from the chemical-potential diagram (Fig. 13) reveals some of the secondary phases that are often obtained while revealing how small the stable region of formation of CZTS is. The chemical-potential range for zinc and tin in kesterite compounds is small where μ_{Zn} is ~ 0.2 eV wide and μ_{Sn} around 0.6 eV wide [46]. These small values for

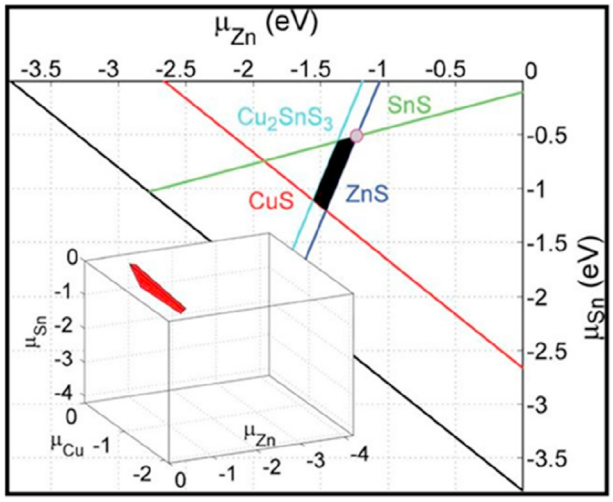

Fig. 13 – The calculated chemical potential region (black area) of CZTS in a 2D Cu-rich plane (the inset represents the stable 3D region). Reproduced with permission [51]. (Copyright John Wiley & Sons).

these elements in kesterite compounds suggest the need for stricter chemical potential control of Zn and Sn during synthesis/fabrication process.

The chemical-potential space suggests under regulated conditions, a Cu-rich diffusion is more suitable for obtaining a single phase kesterite contrary to the Cu-poor conditions (allows for the creation of a copper deficient phase near the CdS interface referred to as an Ordered Defect Compound (ODC) which passivates the surface, therefore reducing interface recombination at the CZTS/CdS junction) that give high efficiency devices [46,83,94–96]. This means that under regulated conditions, the Cu-poor and Zn-rich conditions will result in formation of secondary phases such as ZnS or ZnSe depending on the chalcogen used. Due to the narrow accessible range of μ_{Zn}, a Zn-rich will result in the formation of ZnS while Zn-poor will result in the formation of Cu_2SnS_3 secondary phases. The major challenge for the kesterite device becomes the issue of its composition conditions and phase control during synthesis/fabrication [46,86,97]. One of the effects of a Cu-rich composition is that of inducing high electrical conductivity in the kesterite device leading to shunt losses which adversely affects the PV cell [86]. It cannot be overstated how important it is having precise control of the elemental composition. There are also the intrinsic defects in the kesterite absorber layer which can affect the performance of the cell. These defects contribute to charge trapping and recombination losses [84]. Kesterite as a p-type semiconductor material has huge copper vacancies, V_{Cu} (located at ~ 0.02 eV above the valence band maximum, V_{BM}) and Cu_{Zn} (located at 0.10 eV above the V_{BM}) antisite defects. These defects are dependent on formation energy. V_{Cu} produces deep donor level in the bandgap which causes reduction in bandgap energy [46]. This relates to why the copper-poor and zinc-rich composition is ideal for high performance of the cell. Control of these defects is critical as they dramatically affect the optical and electrical properties of the kesterite compound which in return affects the general performance of the cell. Smooth and compact microstructures are ideal for better cell performance as porous microstructures deliver a charge recombination situation at the grain boundaries which results in poor cell performance [98–100]. The presence of secondary cell formation at certain conditions such as exposure to high temperatures where kesterite phase is not stable must be controlled as these secondary phases can either enhance or reduce the carrier concentration directly influencing the electrical properties of the cell and hence its performance [66,96,101,102]. At the kesterite device in general, there has been reports of interfacial conditions that add to the low performance of the cell [81,103]. The formation of MoS_2 layer just between the Mo-layer and the kesterite-absorber layer during device fabrication has been widely reported [81,85,104]. This new layer formation must be controlled as it contributes to a restriction of the charge carriers leading to increased series resistance in the PV cell. The major hurdle to be overcome in kesterite PV cell performance is the large V_{oc} deficit which is reported to be a major factor to the low cell performance of the device [105]. Theoretical reports show that this deficit arises from two major examined factors; (i) Fluctuations in the bandgap which results in lower than expected average bandgap, and (ii) Fluctuations due to electrostatic potentials which do not change the bandgap in any position rather causes non-local recombination as they are parallel shifts in conduction and valence band energies [86]. This deficit is linked to interface recombination and band tailing resulting in electrostatic fluctuations which contributes to reduced lifetime of the minority carrier. The antisite defects contribute to the two fluctuations listed earlier and so strategies to mitigate these defects must be employed during cell synthesis and fabrication [86,106].

Given its small area of composition, binary and ternary secondary phases can form in addition to CZTS throughout the growth period. These phases consist of ZnS, SnS, SnS_2, CuS, Cu_2S, and Cu_2SnS_3. Formation of secondary phases was suggested to be associated with the film composition [107]. As stated in the previous section, the best copper-poor and zinc-rich composition for the CZTS device results in ZnS or ZnSe phases present within the CZTS or CZTSe compound. Many published works stated the formation of this secondary phase in copper-poor and zinc-rich composition [108,109]. ZnS and ZnSe crystallize in the sphalerite and wurtzite structure composing of wide bandgap (around 3.6 eV for ZnS [108]), and they will build insulator areas in the absorber layer of the solar cell.

Depending on its concentration, ZnS can limit the active area (where the electron-hole pairs are produced) and influence current accumulation. Because of the low conductivity of ZnS and ZnSe, they don't impact the V_{oc} of the device, yet could cause an expansion in the series resistance [110]. The copper sulfide phases (CuS and Cu_2S) are expected in CZTS samples with Cu-rich composition. They have a chalcocite structure and show p-type nature with good metallic conduction, which is due to a high concentration of holes in the valence band [111–113]. Their presence is detrimental to the solar cell because they can shunt the device. Tin sulfide phases can evolve in Sn-rich CZTS films as SnS or SnS_2. The SnS compound is a semiconductor with application in optoelectronic and PV fields. The material exhibits both p- and n-type conduction [114] with a bandgap of 1.2–1.7 eV [115–119]. Tin

disulfide (SnS_2) is an n-type material with direct bandgap of 2.18–2.44 eV [115,117,118]. Although no harmful effects were reported of SnS phases on solar cell performance, a high concentration of the n-type semiconductor in the p-type active layer can build a second diode that hinders carrier collection and thus reduces fill factor. Cu_2SnS_3 (CTS) is a ternary secondary phase that forms in CZTS material with Zn-poor composition. The compound is a p-type semiconductor with metallic character [120], crystallizing in different crystal structures including cubic, monoclinic, and hexagonal forms [121,122]. However, the cubic form requires temperatures higher than 775 °C to crystallize [123]; therefore, it is unlikely to be detected in kesterite films, which are prepared in lower temperatures. Depending on the crystallographic structure, the optical bandgap is in the range of 0.93–1.35 eV [124]. As $Cu_{2-x}S$ phases, CTS is harmful to the solar cell because of its high conductivity, which could decrease the shunt resistance, and its low bandgap could reduce the V_{oc}. The x-ray diffraction (XRD) is viewed as the essential method for identifying elements and compounds. In any case, it has some constraint while distinguishing phases with comparable crystal structure in a compound. This case is available in the CZTS material since ZnS, CTS, and CZTS show diffraction peaks at similar positions (Fig. 14) because of the similitude in the crystal structure and lattice parameters [125]. Other secondary phases, for example, CuS and SnS, can be identified effectively by XRD [126].

Raman spectroscopy is generally utilized as an integral method to identify auxiliary phases in CZTS. The kesterite CZTS displays two sharp peaks at 288–289 cm^{-1} and 338–239 cm^{-1}, a shoulder with a primary peak at 351 cm^{-1}, and a broad peak between 368 and 373 cm^{-1} [127]. For the cubic zinc sulfide phase, one sharp peak shows up at 352 cm^{-1} and a weaker one at 271 cm^{-1} [112]. Raman shifts of monoclinic CTS show up at 290 cm^{-1} and 352 cm^{-1} [113], and of the cubic CTS at 267 cm^{-1}, 303 cm^{-1}, and 356 cm^{-1} [128,129]. The tetragonal CTS indicates two sharp peaks at 337 cm^{-1} and 352 cm^{-1}, and a broad peak between 280 cm^{-1} and 290 cm^{-1} with peak maximum at 297 cm^{-1}. Table 1 records the places of Raman shift for CZTS and the generally observable auxiliary phases. Note that the greater part of previous attempts to obtain the properties of CZTS by Raman spectroscopy were performed via blue and green wavelength excitations of 488, 514.5, and 532 nm, which are normally used for Raman estimations. Latest investigations uncovered extra Raman modes by utilizing nonstandard excitation wavelengths. Dimitrievska et al. [130] explored Raman scattering estimations of CZTS utilizing six distinctive excitation wavelengths from near infrared to ultraviolet and discovered 18 peaks attributed to CZTS which was credited to the 27 optical modes expected for CZTS. Considering that the ZnS stage has its fundamental Raman peak at 352 cm^{-1} and that CZTS displays one peak nearly at a similar position (351 cm^{-1}), it makes it hard to differentiate/recognize ZnS from CZTS. The trouble in separating ZnS from CZTS utilizing Raman scattering was explained to be as a result of utilizing excitation wavelengths in the visible region [108]. It has been shown tentatively that the ZnS auxiliary phase can be effectively recognized from CZTS by using an ultraviolet excitation wavelength of 325 nm [128] (see Table 2).

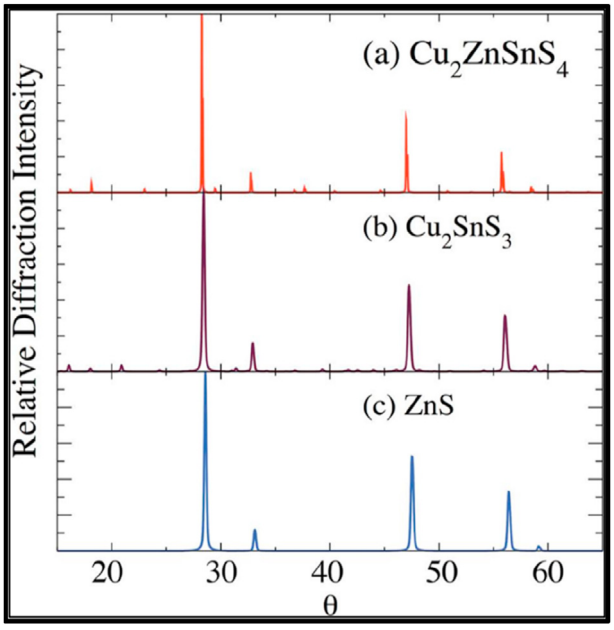

Fig. 14 – Simulated X-ray diffraction spectra of kesterite CZTS, CTS, and ZnS showing overlap of the main peaks. Reproduced with permission [51]. (Copyright John Wiley % Sons).

5. Synthesis routes for CZTS/Se nanoparticles

Since the advent of nanotechnology, many materials have been synthesized in the nanoscale to improve their properties. As we will discuss later in the next section on the different deposition methods, the synthesis of CZTS nanoparticles through simple chemical reactions presents a much easier and cost-effective route for obtaining kesterite materials which are subsequently deposited through any of the non-vacuum methods for PV applications. Here we present some of the chemical reaction routes that have successfully led to the synthesis of CZTS nanoparticles especially yielding the pure phase of kesterite. Table 1 summarizes the various parameters that were employed by various groups (including the

Table 1 – Raman shift positions of CZTS and of the common secondary phases.

Phase	Raman Shifts (cm^{-1})	References
CZTS	287, 338, 351, 368	[131]
Monoclinic CTS	290, 352	[122]
Cubic CTS	267, 303, 356	[123]
Tetragonal CTS	297, 337, 352	[120]
Orthorhombic Cu_3SnS_4	318	[121]
$Cu_{2-x}S$	264, 475	[111]
Cubic ZnS	275, 352	[132]
SnS	163, 189, 220	[118]
SnS_2	215, 315	[118]
Sn_2S_3	52, 60, 307	[118]
Hexagonal MoS_2	287, 383, 409	[127]

Table 2 – Parameters and bandgap obtained from different synthesis routes for CZTS/Se compounds.

Compound	Synthesis route	Chalcogen Source	Important parameter	Bandgap	Phase	Ref.
CZTS	Hot-Injection	Elemental sulfur in oleylamine	Oleylamine mixtures of cations and sulfur were injected at 300 °C and held for 75 min.	1.5 eV	Kesterite	[146]
CZTS	Hot-Injection	Elemental S in TOP	TOP-S was injected at temperature of 275 °C at different times of 1, 8 and 15 min.	2.64 eV (1) 1.54 eV (8) 1.43 eV (15)	$Cu_{2-x}S$-Orthorhombic (1) Cu_2SnS_3-Tetragonal (8) Kesterite (15)	[147]
CZTSe	Hot-Injection	diphenyl selenide	$SnCl_2$ mixed with oleic acid and oleylamine injected at 250 °C for 1 h.	1.38 eV	Kesterite Wurtzite	[148]
CZTS	Hot-Injection	Na_2S	Sulfur precursor injected at 80 °C and increased to 190 °C and held for 2 h.	1.37 eV	Kesterite	[45]
CZTS	Hot-Injection	t-DDT	TOPO used as stabilizer and t-DDT was injected at 150 °C and allowed for 1 h.	1.59 eV	Wurtzite	[149]
CZTS	Solvothermal	Elemental Sulfur	Ethylenediamine as solvent. Reaction occurred in teflon stainless steel at 180 °C for 15 h.	1.5 eV	Kesterite	[141]
CZTS	Microwave Solvothermal	Na_2S	Ethylene glycol Mixed with PVP as solvents. Reaction was performed at 300 W microwave power-180 °C for 15 min and 1 h, and 160 °C for 1 h.	1.25–1.30 eV	Kesterite	[138]
CZTS	Solvothermal	Elemental sulfur	Reaction Performed in a Teflon stainless steel autoclave at 200 °C for 24 h	1.52 eV	Kesterite	[150]
CZTS	Solvothermal	Thiourea	PVP and ethylene glycol used as solvents. Reaction was performed in a teflon stainless steel at 180 °C for 30 h and calcined at 450 °C for 3 h	1.5 eV	Non-Calcined (Secondary phases) Calcined (Kesterite)	[145]
CZTS	Microwave Solvothermal	Thiourea	Ethylenediamine and deionized water. Performed at 160 °C –240 °C for 1 h.	1.45 eV and 1.50 eV	Cu_2S and Wurtzite <200 °C. Kesterite >200 °C.	[151]

(*continued on next page*)

Table 2 – (continued)

Compound	Synthesis route	Chalcogen Source	Important parameter	Bandgap	Phase	Ref.
CZTS	Microwave Hydrothermal	Na_2S	Water and 3-mercaptoacetic acid (MAA) used as solvent. Performed at 100 °C for 1 h at microwave power of 500 W.	1.40 eV	Kesterite	[140]
CZTS	Hydrothermal	Thiourea	Ethylenediamine as solvents. Reaction was performed in a teflon stainless steel autoclave at 180 °C for 16 h.	1.7 eV	Kesterite	[133]
CZTS	Hydrothermal	Na_2S	Ethylenediamine and de-ionized water as solvent. Reaction was performed in a teflon stainless steel at 220 °C for 12, 18 and 24 h.	1.53 eV (18 h) 1.55 eV (24 h)	Kesterite/Secondary phases (18 h) Kesterite (24 h)	[137]

ones not mentioned in the discussions below) in synthesizing kesterite nanoparticles.

5.1. *Hydrothermal synthesis*

Hydrothermal synthesis is an environmentally friendly method of synthesizing nanoparticles as it uses water and small amount of organic solvent [133]. This method is very attractive in the synthesis of kesterite nanoparticles as it boosters the environmental friendliness of both the method of synthesis and the composition of the material. This method entails a conventional route and microwave route [134–138]. The conventional route uses autoclave while the microwave route uses a microwave. In recent times, many researchers have obtained kesterite nanoparticles via this method. Vanalakar et al. synthesized CZTS nanoparticles by using sodium sulfide as sulfur precursor and the chlorides of the Cu, Zn and Sn as the cation precursors. The sulfur precursor and cation precursors were dissolved in de-ionized water and ethylenediamine (acting as a binder to prevent high agglomeration) was added to the precursor solution and after stirring transferred to a Teflon teel stainless autoclave and heated at 220 °C for 12, 18 and 24 h [137]. The CZTS materials that were obtained at the different times were named based on the reaction times such as CZTS-12, CZTS-18 and CZTS-24. The study explored the effect of reaction time on the synthesis outcome of the CZTS nanoparticles. From XRD analysis of these nanoparticles, the formation of secondary phases reduced as the reaction time increased, with CZTS-12 forming three secondary phases, CZTS-18 forming one secondary phase and CZTS-24 formed no secondary phase and had higher peak intensity indicative of improved crystallinity as seen in Fig. 15a. The size of the nanoparticles were observed to decrease as the reaction time increased with CZTS-18 having particle sizes ranging from 25 to 50 nm while CZTS-24 had particle sizes in the range of 20–30 nm. The bandgap values for CZTS-18 and CZTS-24 were 1.53 eV and 1.55 eV, respectively. These bandgap values are optimal for PV cell application. They were able to demonstrate the importance of reaction time in hydrothermal synthesis route (a green synthesis route) on the formation of pure phased kesterite nanoparticles and their properties suitable for PV application [137]. Phaltane et al. synthesized CZTS nanoparticles through hydrothermal route by using thiourea as the sulfur source and chloride salts of the cations as their precursors. In their synthesis, they utilized a 2:1:1:8 ratio for the Cu, Zn, Sn and S precursors, respectively [139]. These precursors were dissolved in a mixed solvent of 1:1 ethanol to water content. This was subsequently transferred into an autoclave and sealed. The synthesis reaction was performed at 210 °C for 24 h in a muffle furnace. The kesterite phase was confirmed by the XRD and Raman spectroscopy analysis of the synthesized products. Direct bandgaps of 1.4 eV and 1.53 eV was obtained for synthesized and annealed powder samples, respectively. The CZTS powder was applied as a photocatalyst for the degradation of aqueous methylene blue solution. They observed that the degradation of methylene blue solution increased by 50% on addition of CZTS as light was irradiated into the methylene aqueous solution for 45 min with

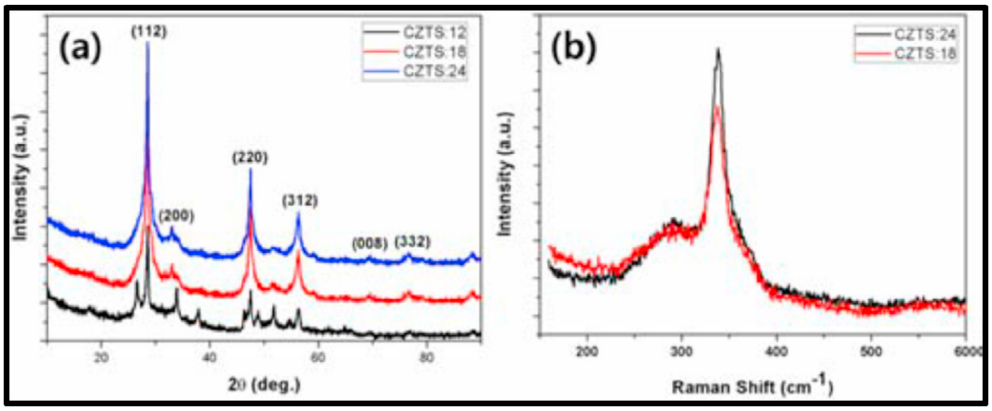

Fig. 15 – (a) PXRD pattern of the CZTS samples and (b) Raman spectrum of CZTS samples. Reproduced with permission [137]. (Copyright John Wiley and Sons).

calculated degradation rate of 0.018 min^{-1} [139]. In their work, they were able to show that at elevated temperature (during annealing), there was observable improved crystallinity.

Tiong et al. explored the hydrothermal synthesis of CZTS using hydrated salts of the metals and different sulfur sources such as nonahydrate of sodium sulfide, thioacetamide or thiourea to determine the effect of sulfur source on the formation of the kesterite phase [134]. The reaction involved the dissolution of the precursors in a mixture containing thioglycolic acid (TGA) and Milli-Q water under vigorous stirring. They observed that the sulfur precursors used in the synthesis method showed significant effect on the phase purity and crystal structure of the synthesized CZTS materials. Kesterite pure phase was obtained when they used Na_2S as the sulfur source in the hydrothermal synthesis while a mixture of kesterite and wurtzite phases were observed when organic sulfur sources such as thioacetamide was used. From XRD refinement analysis of the mixed phase CZTS nanocrystals obtained from the use of thioacetamide, they determined that the kesterite phase accounted for 74% and the rest as wurtzite phase. Also, the bandgap (E_g)of the mixed phase material (1.58 eV) was slightly higher than that of the pure kesterite phase material (1.51 eV). The nanocrystals obtained using Na_2S as the sulfur precursor were used to form thin-films and annealed at temperatures of 550 °C and 600 °C and analyzed for photocatalytic purposes. The film obtained at 600 °C showed a higher and more stable photocurrent during photoelectrochemical analysis which was attributed to the larger grains (which leads to reduction of recombination between electron hole pairs in the film) obtained at this temperature than that obtained for 550 °C.

Martini et al. prepared three solutions as while synthesizing kesterite nanoparticles. The first solution contained a mixture of the chloride salt of tin in distilled water with the addition of HCl to adjust the pH to 0.5. The second solution contained the acetate dihydrate of zinc and copper acetate monohydrate in distilled water [140]. The third solution contained sodium sulfate in distilled water. The first solution was mixed with the second solution with the addition of 3-mercaptoacetic acid (MAA) in dropwise fashion. Color changes from purple to light yellow were observed. The pH of this solution was adjusted to 6.0 with the addition of NH_4OH and was then mixed with the third solution prepared above. A dark-red solution resulted from this mixture and was heated up to 100 °C using a microwave irradiation with flow rate of 18.5 ml/min and a power of 500 W applied. The obtained

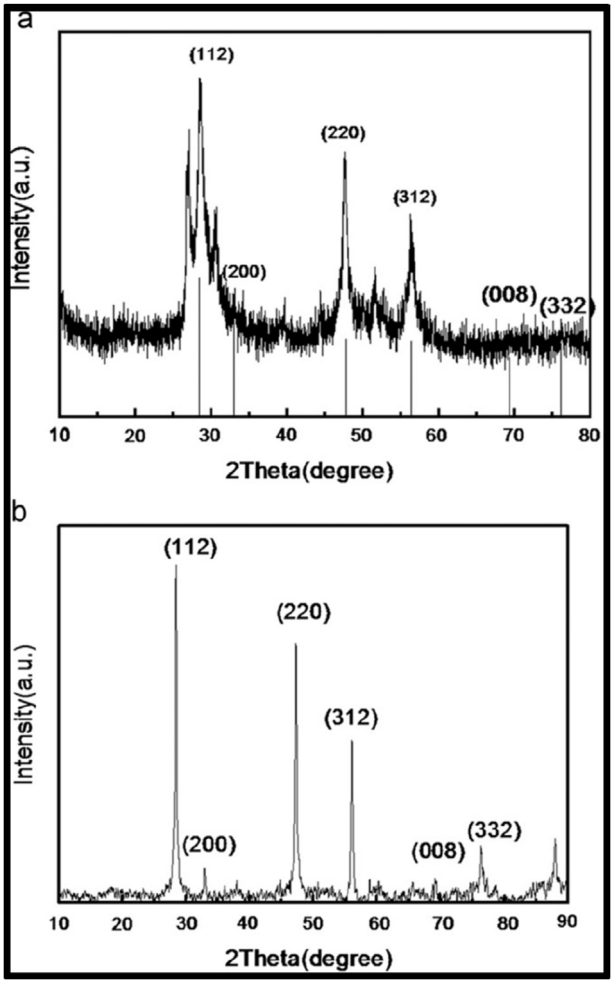

Fig. 16 – XRD pattern of as-synthesized (a) and annealed (b) CZTS nanoparticles. Reproduced with permission [141]. (Copyright Elsevier).

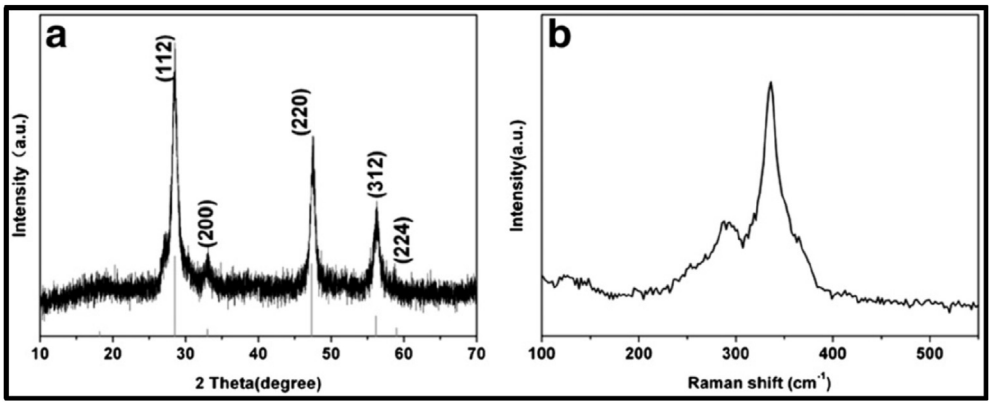

Fig. 17 – (a) XRD pattern of CZTS nanocrystals, the gray line shows the simulated pattern of kesterite CZTS (JCPDS 26-0575) and (b) Raman scattering spectra of CZTS nanocrystals. Reproduced with permission [154]. (Copyright Elsevier).

nanoparticle through its XRD analysis revealed a semi-amorphous nature due to the low temperature used during synthesis, however, on treating nanoparticles in vacuum to higher temperature of 300 °C, three prominent kesterite peaks were observed with 2 additional peaks belonging to the secondary phase of copper sulfide. The formation of the kesterite phase at the elevated temperature of treatment (300 °C) was further confirmed from Raman spectra where the most intense peak at 337 cm^{-1} corresponds to the A1 vibration mode of kesterite. The copper sulfide peaks were not observed in the Raman spectra partly due to low intensity of its signals. Bandgap value of 1.4 eV was obtained which is close to optimal bandgap value for thin-film PV cells making the method a suitable route of synthesizing CZTS nanoparticles that are applicable for PV cells [140].

5.2. *Solvothermal synthesis*

The method entails developing of crystal materials from a non-aqueous solution usually in an autoclave at high temperatures and pressure. This method is like hydrothermal synthesis only differing in the use of non-aqueous solvents. Just like hydrothermal synthesis, the solvothermal synthesis also involves conventional and microwave synthesis route where the conventional route involves the use of autoclave and microwave route uses a microwave. Many researchers have successfully synthesized kesterite nanoparticles via this method [138,141–144].

Mali et al. used hydrated chloride salts of tin (IV), copper (II) and anhydrous chloride salt of zinc (II) as cation precursor for the synthesis of kesterite nanoparticles. Ethylene glycol was used as solvent with the addition of polyvinylpyrrolidone (PVP) as capping agent and thiourea as sulfur source [145]. The synthesis involved the dissolution of the cation precursors, the capping agents and thiourea in ethylene glycol and transferred to a Teflon stainless-steel autoclave. The autoclave was maintained at 180 °C for 30 h after which it was cooled to room temperature. The indexed XRD patterns for the products obtained at 180 °C gave peaks that were attributed to the kesterite phase and peaks of some secondary phases. The calcined product at 450 °C gave strong peaks indexed to kesterite phase with no secondary phases revealing the formation of pure kesterite phase at elevated temperatures. The kesterite phase for the calcined product was further confirmed via micro-Raman spectrum obtained for the product showing an intense peak at 338 cm^{-1} which has been reported for kesterite phases. The absence of other peaks confirms the successful synthesis of the pure kesterite phase. An optical bandgap of ~1.5 eV was obtained from the ultraviolet visible (UV–vis) absorption analysis agreeing with the optimal bandgap of kesterite [145].

Cao et al. used sulfur powder as their sulfur source, zinc acetate as zinc source and the chlorides of copper and tin as their copper and tin source, respectively [141]. These precursors were transferred into a Teflon stainless-steel autoclave which was filled to 80% capacity with ethylenediamine and afterwards sealed. The autoclave was maintained at 180 °C for 15 h and cooled naturally to room temperature. Further annealing of the final product improved the crystallinity of the product as the XRD of the as-synthesized product gave peaks attributed to secondary phase ZnS while the annealed product gave peaks that are attributed only to the kesterite phase (Fig. 16). UV–vis absorption spectrum of the nanoparticles was used to obtain the optical bandgap of the kesterite material through Tauc plot. The bandgap obtained was ~1.5 eV which strongly corresponds to the optimal bandgap value for kesterite materials and suitability for PV device application [141].

Patro et al. followed the microwave-assisted solvothermal synthesis route. They used chloride salts of zinc and copper and hydrated chloride of tin as the cation sources and thiourea as the sulfur source [144]. For the synthesis, weighed elemental sources were sequentially added to ethylene glycol (solvent) at room temperature under vigorous stirring until all the precursors were dissolved. The dissolved mixture was transferred to a quartz tube and placed in a microwave synthesizer operating at 2.45 GHz. The temperature of operation was 180 °C for 30 min [144]. The final product was then vacuum dried at 70 °C for 3 h. Subsequently the sample was annealed at 500 °C for 30 min. XRD patterns for both synthesized and annealed products gave characteristics peaks of kesterite phase with no secondary phase peaks with improved crystallinity at elevated temperature of 500 °C. SAED patterns obtained were indexed to planes consistent with the XRD

data. The kesterite phase was further confirmed from Raman spectra which gave intense peak at 329 cm^{-1} and weak peak at 284 cm^{-1} which are characteristic peaks of kesterite phase. This confirms no formation of secondary phases. From UV–vis spectrum, the estimated bandgap of the CZTS sample was 1.67 eV. These properties make the sample suitable for PV application [144].

5.3. *Hot-injection synthesis*

The synthesis of kesterite nanoparticles were first reported via hot-injection method. The process entails the rapid injection of the sulfur precursor to already reacting cation precursor as the reaction reaches a certain temperature. Nucleation takes place leading to formation of the kesterite particles. The first attempt at synthesizing CZTS nanocrystals was by Riho et al. In their work, organic salts of the cations were used and elemental sulfur powder as the sulfur source. Oleylamine was used to dissolve the cation precursors and the sulfur precursor in different reaction vessels at specific temperatures. Trioctylphosphine oxide (TOPO) was heated to 300 °C and the sulfur and cation precursors were rapidly injected into heated TOPO. They were able to successfully synthesize CZTS nanocrystals through the method. The XRD and differential thermal analysis (DTA) of the nanocrystals confirmed pure crystal phase of kesterite. They obtained a bandgap of 1.5 eV which is suitable for PV application. The success of their work opened up the research route to the possibility of successfully synthesizing CZTS materials via solution process and from their continued work through the method was able to synthesize tunable CZTSSe nanocrystals [146,152,153].

Dong et al. used copper (II) chloride, zinc chloride and tin (II) chloride as precursors for copper, zinc, and tin, respectively. sodium sulfide was used as sulfur source while diethylene glycol (DEG) was used as solvent [45]. From the results obtained, nanoparticles of sizes ranging from 10 to 20 nm were obtained. The morphologically, the nanoparticles agglomerated to form larger particles. The XRD reported in their work revealed presence of broad Bragg's peaks which are attribute to the small particle sizes of the nanoparticles. The XRD results also confirmed the successful synthesis of the kesterite phase. The XRD of the kesterite nanoparticles became sharper after sintering the as-synthesized nanoparticles to a temperature of 500 °C for 2 h. Raman spectroscopy confirmed that the nanoparticles were of the pure kesterite phase as there were no peaks for secondary phases. The thermal gravimetric analysis (TGA) of the nanoparticles obtained showed the material was stable at elevated temperature of up to 600 °C. A bandgap of 1.37 eV was obtained which is close to the optimal direct bandgap value for PV application [45].

With thiourea as the sulfur source and oleylamine as the solvent for synthesis, Wei et al. synthesized spindle-like kesterite nanoparticles through hot injection method. In their synthesis, hydrated salts of copper and tin and anhydrous zinc chloride were used as precursor for the cation component of the material [154]. The XRD spectrum obtained gave three broad peaks at $2\theta = 28.5°$, 47.6° and 56.3°, which were assigned to planes of (112), (220) and (312), respectively of the tetragonal arrangement of kesterite phase. Raman spectra analysis confirmed the kesterite phase as the only phase obtained for the nanoparticles with shifts of 338 cm^{-1} and 289 cm^{-1} characteristic of kesterite phase (Fig. 17) [154].

6. Fabrication of kesterite thin-film PV cells

6.1. *Device architecture*

One important advantage kesterite material enjoys is the availability of mode of synthesis and device fabrication because of its analogous crystal structure with CIGS. Time that would have been spent finding ways to synthesis and fabricate the kesterite device has been cut short because of this advantage. Most of the successful routes of synthesizing and fabricating CIGS materials can be easily applied to obtain kesterite materials [83,155–157]. The fabrication of the kesterite PV device follows similar device stacking that has been reported for CIGS. Soda-lime glass (SLG) has been used successfully for CIGS solar cells and have been found to exhibit special advantageous effect as substrate for the device. It has become substrate choice for kesterite PV devices. It has been found that Na from the glass diffuses through the Mo layer into the CIGS or CZTS absorber layers. There has not been a full understanding of the role Na plays in improving the device performance rather it has been attributed with passivation of surface grain boundary defects and increased charge carrier concentration. Although CZTS can be grown on other substrates, yet its growth on these other substrates such as metal or flexible plastic substrates will require the addition of external sodium. The back contact is the first layer to be deposited in the architecture of CZTS PV cell. SLG substrate is coated with molybdenum forming the back contact of the device. Some other back contacts such as indium doped tin oxide (ITO) and fluorine doped tin oxide (FTO) have been explored and reported. Molybdenum back contacts are widely reported and advantageous as back contact for CZTS devices as they are stable at high temperatures, has high resistance to

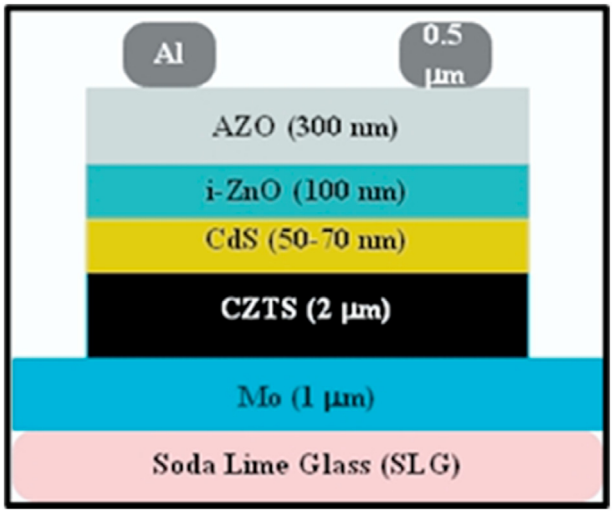

Fig. 18 – Schematic drawing of device architecture of kesterite PV cell showing the different layers and their thickness.

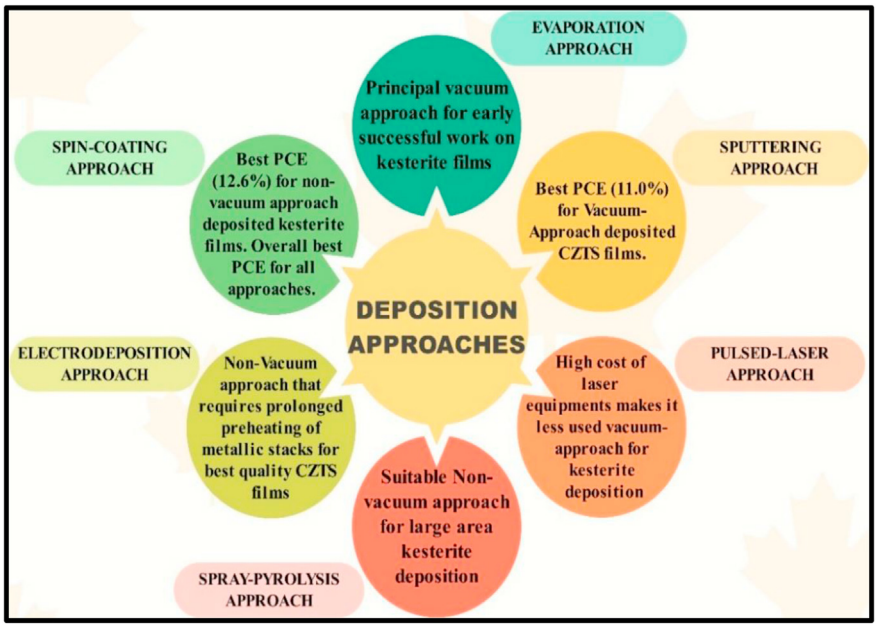

Fig. 19 – Schematic overview of peculiarity of various thin-film deposition approaches in relation to kesterite.

the formation of alloys with copper and has great adhesion with the kesterite absorber layer [158–160]. The basic functions of the back contact layer is to act as the charge extractor for the holes created by the absorber layer. The kesterite absorber layer is deposited directly on the molybdenum back contact to a thickness of about ~2 μm. The deposition of the kesterite absorber layer can be achieved through physical and chemical deposition routes [84,135]. The physical deposition routes are sputtering, pulsed-layer deposition, electron beam evaporation, and spin coating while the chemical deposition routes are chemical vapor deposition, CVD and plasma enhanced chemical vapor deposition, PECVD [84]. In the device stacking as earlier mentioned, the kesterite layer serves as the p-type semiconductor component which produces electron hole pairs (EHP). The kesterite deposited molybdenum soda lime glass is immediately annealed in a sulfur atmosphere to improve its crystallinity. After annealing the kesterite absorber layer, the buffer layer comprised of cadmium sulfide, CdS (n-type) sometimes supplanted with zinc sulfide (ZnS) due to the toxic nature of cadmium is deposited via chemical bath method (thickness for CdS is maintained at 50 nm to minimize series resistance R_s in the device) [80,84,161]. The window layer of intrinsic zinc oxide (i-ZnO) with a thickness of 80–100 nm is then deposited through sputtering. The reason for using the i-ZnO layer is to minimize shunting pathways and prevent intermixing between the absorber and the transparent conductive oxide (TCO) when the thin CdS layer does not provide complete coverage of the underlying CZTS layer. A layer of transparent conductive oxide (TCO) which provides electrical front contact usually aluminum doped zinc oxide (AZO) is deposited afterwards. To choose a good TCO it must possess high transmittance and high electrical conductivity. At the final stage, Ni/Al contacts are deposited on the TCO for charge extraction [86]. The final architecture of the CZTS PV device can be seen in Fig. 18 below.

The structure of a kesterite solar cell is quite complex because it contains several compounds as stacked films that may react with each other. Fortunately, no detrimental interface reactions occur at ambient temperatures. The formation of MoS(e)2 at the back contact/CZTSSe interface during CZTSSe thin film growth is inevitable through reactions between Mo and chalcogen at high chalcogen partial pressure or CZTSSe in the absence of chalcogen excess [134], which may facilitate an electrical quasi-ohmic contact and improve the adhesion of CZTSSe to Mo back contact, but leads to a high series resistance and accordingly reduces the device efficiency if not thin enough [135], similar to the case of CIGSe solar cells [136]. A mild diffusion of Cd into kesterite has been reported which is believed to be beneficial to the cell performance [137]. This could be interpreted as the occupation of Cd for vacant Cu sites in the Cu-poor and Zn-rich CZTS matrix (which favors the formation of Cu vacancies [138]) according to the first-principles calculations [139] and Sardashti's report [140]. In CIGSe solar cells, a similar behavior at the CIGSe/CdS interface has been reported by many groups [141,142] and is believed to be the key factor to the success of the CBD-CdS process [143]. Similar to the role of ordered vacancy compound Cu(InGa)3Se5 (OVC) in CIGSe, Cd on Cu sites would act as substitutional donors, and therefore give result in n-type absorber surface, facilitating a more effective buried homojunction [144].

6.2. *Kesterite absorber layer deposition approaches*

Kesterite PV cell is receiving much attention due to the various techniques available for the formation of its thin-film on PV cell platforms. Figure 19 gives an overview of some of the strides peculiar to these deposition techniques as it relates to kesterite. The compositional control of the material poses a challenge to the various routes of deposition as there is no complete knowledge on how to control the progression of phases or that of the phase diagram as films are formed.

Although these challenges are daunting, remarkable PV cells have been fabricated via these routes.

6.2.1. *Vacuum deposition approaches*

Vacuum depositions are procedures used to deposit layers of material atom-by-atom or particle by-particle on a substrate. These procedures work at pressures well beneath barometrical weight (i.e., vacuum). These deposited layers can go from a thickness of one atom up to millimeters of freestanding structures. This method of deposition can further be categorized into sputtering-based and evaporation-based depositions. There have been serious challenges to the use of the method for deposition in kesterite device fabrication. The primary issue centers on element vaporization and reevaporation from films already deposited due to atmospheric pressure as a result of conditions of the vacuum process during heating. For instance, there has been studies as it relates to the evolution of Sn in the form of SnS for compounds like Cu_2SnS_3, SnS, Cu_4SnS_4 and Cu_2ZnSnS_4 [162,163].

6.2.1.1. Evaporation-based deposition. Evaporation technique has widely been reported for the deposition of the CIGS PV devices, and have resulted in remarkable efficiency for this device (22% for laboratory records) [164].

The vacuum thermal evaporation deposition technique consists in heating until evaporation of the material to be deposited. The material vapor finally condenses in form of thin film on the cold substrate surface and on the vacuum chamber walls. The analogous implication of the kesterite structure of CZTS and chalcopyrite structure of CIGS, necessitates the use of this method for the deposition of CZTS absorber layer [165]. At a substrate temperature (T_s) of 150 °C, multilayer elemental Cu/Sn/Zn with Zn as the bottom stack were evaporated as the first successful evaporated kesterite device by Katagiri et al. The multilayer stack was subsequently sulfurized at 500 °C in a Pyrex glass tube using nitrogen under 5% H_2S atmosphere. The recorded power conversion efficiency (PCE) for the device was 0.66% [57]. Since then, there has been improvements made during deposition of the kesterite absorber layer such as the use of ZnS instead of Zn for the bottom part of the metal stack resulting in an increased efficiency of 2.62% [166]. Schubert et al. introduced a fast co-evaporation process where a 1.4 μm absorber layer of CZTS was deposited on a Mo-coated SLG substrate using ZnS, Sn, Cu and S sources in 16 min. This was performed under sulfur partial pressure (~3×10^{-8} atm) at T_s of 550 °C. With the observation of CuS secondary phase from grazing incidence XRD analysis, KCN etching was applied to eliminate the secondary phase. An efficiency of 4.1% was achieved for the overall device [167].

Sequential co-evaporation process has been used for the deposition of the kesterite absorber layer. Shin et al. reported till date the highest efficiency recorded for the evaporation deposition technique for CZTS-based kesterite devices. In the process, co-evaporation of the elements was achieved at T_s of 150 °C. This was followed by a fast-high temperature annealing under N_2 atmosphere resulting in a cell efficiency of 8.4% with a CZTS absorber layer thickness of 600 nm [168].

6.2.1.2. Sputtering-based deposition. The sputtering-based deposition route is an efficient route for deposition of layers for thin film devices. It involves introducing a controlled gas, usually chemically inert argon, into a vacuum chamber, and electrically energizing a cathode to establish a self-sustaining plasma. The exposed surface of the cathode, called the target, is a slab of the material to be coated onto the substrates. It has been reported for CIGS devices and have been applied in the fabrication of kesterite-based devices [164]. Sputtering can be done as sequential sputtering or co-sputtering. The two sputtering strategies have been used successfully in the growth of high quality CZTS absorbers which has led to improved device efficiencies [169–172]. Sequential sputtering provides easy control of the chemical composition of the films by regulating the thickness of each element while co-sputtering allows the deposition of homogeneous mixture of the elements and helps in minimizing the diffusion of elements during annealing. The highest efficiency presently recorded for CZTS-based PV cells (11.6%) was achieved via sputtering method [170]. Several other works reported through this method of deposition have efficiencies above 10%. Ito et al. first reported CZTS thin-film deposition via argon beam sputtering from the quaternary material pressed target [72]. With no post sulfurization treatment, crystalline material was reported at T_s as low as 90 °C. Although no device efficiency was provided for their work, open circuit voltage of 165 mV was reported for the work. Subsequently, some works have reported successful thin film deposition through RF magnetron sputtering process where the metal layers are sequentially deposited followed by sulfurization at high temperatures to obtain the suitable tetragonal kesterite phase [76,173]. Zhang et al. through sulfurization with elemental sulfur in inert atmosphere of nitrogen sputtered stacked Cu/Sn/Zn (with Zn as at the bottom of the stack) metal layers at temperatures of 300 °C for 1 h and 550 °C for 3 h [173]. Lower temperature of 300 °C was used to minimize volatility of the metals prior to increasing the temperature to 500 °C [173]. The RF-sputtering and sulfurization of metal multilayers in a two-zone vacuum furnace was explored by Yoo et al. One zone was used the metal multilayer film and the other zone used for sulfurization at 570 °C for 20 min. The aim of sulfurization zone is to convert the metals into sulfide films. In order to control the stoichiometry of the metal components, the thickness of individual metal precursor layers was varied, they found that with Cu-poor stoichiometry no secondary phase was formed but by following the correct stoichiometry of CZTS, $Cu_{2-x}S$ secondary phase was formed [174]. Katagiri et al. achieved the best sputtering route for the deposition of CZTS, where they co-sputtered Cu, binary ZnS and SnS precursors. Substrate rotation enabled them to obtain fine blend and homogeneity of the precursors during sputtering with the samples subjected to final high annealing temperature of 580 °C for 3 h in nitrogen using 20% of H_2S [175]. A year after their previous work, Katagiri et al. achieved a high efficiency device of 6.8% via method mentioned above [176]. Through extensive research in the co-sputtering deposition of pure-CZTS, great efficiency improvement for the method having reached highest efficiency of 11.04% [170]. This was achievable through the use of binary compounds or mixed metallic

compound targets in inert atmosphere during sputtering. While both sputtering methods differing in the amount of chalcogen used in the starting precursor, they have significantly contributed to improved efficiencies for the device [170].

6.2.1.3. Pulsed laser deposition (PLD). The first CZTS thin films through PLD was produced by Moriya et al. and achieved a low PCE of 1.74% [177]. Over the years, there has been significant increases in the efficiency obtained for PLD-CZTS devices. Ganuskh et al. achieved the largest efficiency value of 5.4% for this process [178]. In their work, 0.4–1 μm thickness of CZTS films was deposited via PLD on a SLG substrate already coated with Mo in vacuum compartment (with pressure of 9.8×10^{-10}atm). Overall stoichiometric composition of Cu_2ZnSnS_4 as composite target is hit with a laser beam of KrF. The obtained films were annealed with sulfur overpressure at temperature range of 500–600 °C in a graphite box [178]. These two steps were very useful in achieving an efficiency of 5.2% [179] by Cazzaniga et al. and subsequently by Ganuskh et al. [178]. Schou et al. described an observation for the stoichiometry of PLD-CZTS deposited films highlighting the importance of laser energy per unit area (J cm^{-2}) on the blend target. For the best record for the PLD-CZTS deposited film, the desirable Cu-poor and Zn-rich composition was obtained for at affluence range of 0.7–1.0 J cm^{-2} [180]. The common trend observed was that at high fluence, Cu-rich composition was obtained while low fluence led to Cu-poor composition [180]. The repeated cleaning of the vacuum widows and the sturdy reliance on fluence in more technical way influences the concerning issues raised in the use of PLD for the synthesis of the kesterite absorber layer. Another great influence on its use for the kesterite absorber layer and in the PV-industry generally is the high cost of laser equipment.

6.3. *Non-vacuum deposition approaches*

The mix of minimized and effective cost of deposition approaches achieved in non-vacuum approaches and plentiful as well as prompt accessibility of CZTS elemental materials offer an improved possibility of getting remarkable development in photovoltaics. The process involves the choice of suitable solvent to dissolve the metal precursors (usually salts of constituent metal) with that of sulfur and subsequently using one of the non-vacuum deposition approaches to deposit the kesterite absorber layer. The highest solution-based efficiency obtained for the kesterite PV cell was achieved by using hydrazine, an inorganic solvent devoid of carbon and oxygen as solvent of choice [181]. Other solvents that have yielded good efficiencies for the kesterite devices have been reported. Protic solvents like 2-methoxyethanol in combination with monoethanolamine (used as stabilizer) have been used for sol gel preparation of the precursor materials in readiness for deposition [182,183]. The deposition of the sol-gel formed is preferably the spin coating method. Efficiency of 8.8% has been reported for protic solvent method of preparing kesterite precursor materials [184]. Aprotic solvents such as dimethyl-sulfoxide (DMSO) and dimethylformamide (DMF) have been used with thiourea as sulfur source [185–187]. The precursors are made into molecular inks and deposited on the Mo-coated substrate. Efficiencies of over 11% have been reported for spin coated deposition approach [188–191]. For nanoparticle inks, they usually form colloidal dispersions which can present difficulty in forming uniform film on the substrate during deposition [192]. This approach however has been explored through the synthesis of the kesterite nanoparticle by any of the synthesis routes already reported in section 4 and dispersed in suitable solvents like ethanol. The nanoparticle inks can be deposited through spin-coating followed by annealing at high temperature in the presence of nitrogen which has yielded efficiencies from 5 to 7%. Here we detail parts of the non-vacuum methodologies that have yielded high-performing devices via solution-processing approach.

6.3.1. *Spray pyrolysis approach*

Early attempts were reported for non-vacuum deposition of kesterite thin-films through spray pyrolysis. The spray pyrolysis method favors large area deposition as it is compatible with low viscose inks. Alcoholic solvents are most suited for spray pyrolysis due to their low surface tension and help substantially for even spread of film during deposition as opposed to water (could have been most suited and safest choice) which has high surface tension and can cause large droplet size and dismembering of film as it dries [193,194]. In their work, Ito et al. subjected substrates to temperatures of 280 and 360 °C in order to examine the pure state of the obtained phase and the effect of varying ratios of the metals by utilizing metal chlorides and thiourea as metal and sulfur sources, respectively [195]. This deposition was considerably deficient of sulfur deficient when water was used as solvent. Subsequent annealing at elevated temperature of 550 °C in ~5% H_2S and argon inert atmosphere gave ostensible stoichiometry. Other related works have been investigated and reported since the use of the spray pyrolysis approach on CZTS [196–200]. These reports substantially explored the type of precursor, T_s, treatments after heating and the pH of solution. For instance, T_s as a parameter investigated in this sense, impacts the morphology and elemental distribution of the final film [201]. In general, spray pyrolysis of the kesterite films lead to formation of small grain sized particles with high coarse surface [202]. This surface can affect the interface of the CZTS and CdS layers in preparing substrate configuration of PV cells. By using nanoparticle inks in a mixture of 90% water and 10% ethanol efficiency of 10.8% was obtained [203], while 11.0% and 9.8% efficiencies have been realized for molecular inks with DMF and DMSO as solvents, respectively [191,204].

6.3.2. *Electrodeposition approach*

For non-vacuum approaches for metal film formation, electrodeposition is an effective large-scale production approach and has successful utility in the electronics industry. In the PV industry, it is useful for profitable deposition of CdTe. In the kesterite deposition strategy which usually involve a 2-stage approach, such stages are applied to electrodeposition process for kesterite films. The two-stage approach involves firstly the deposition of the metallic component of the kesterite composition and subsequently chalcogenization [205,206]. Pioneering work of Scragg et al. involved the

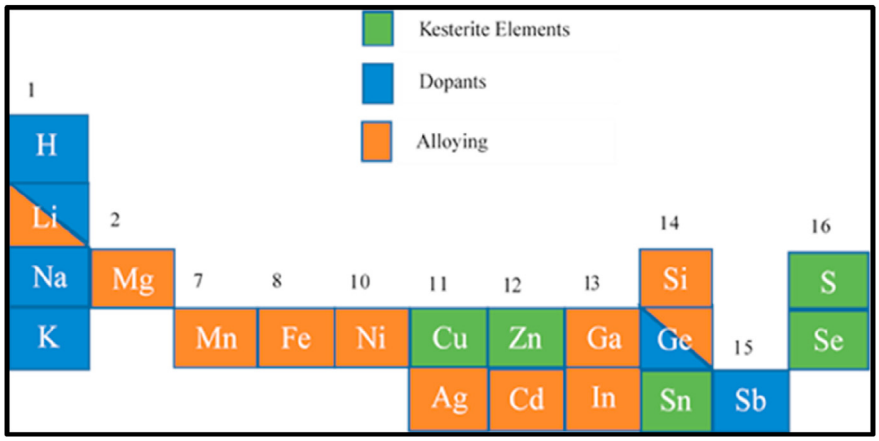

Fig. 20 – Cut out from Periodic table showing doping and alloying elements that can be used in kesterite compounds.

electrodeposition of stacked electroplated Zn/Sn/Cu where Cu is at the bottom [69]. The electrodeposited metals were subsequently transferred to a quartz tube furnace for sulfurization at a temperature of 550 °C for 2 h using elemental sulfur in an argon atmosphere. PCE of 0.8% was obtained for the deposition. This study was behest with high series resistance (10 Ω cm^2), high shunt conductance (7 mS cm^{-2}) in dark conditions and pronounced conjugation in the space charge region [69]. The electrodeposition of the precursors has been achieved through different classifications. For the classification that is based on the number of steps of electrodeposition (often referred to as stacked elemental layers SEL), 2-approaches have been explored [69]. These include: sequential electrodeposition of the (a) elemental metallic layers, (b) stacked alloys in form of CuZn/CuSn and the combination of (a) and (b) above in a successive manner [207–210]. and single electrochemical step to form precursors which includes co-electrodeposition that involves the deposition of CuSnZn compound and one pot electrodeposition involving the incorporation of the chalcogen source into the electrolyte with the sole aim of obtaining the kesterite compound (CZTS or CZTSe) [205].

Through Sequential electrodeposition method, Jiang et al. obtained cell efficiency of 8.1% for sulfurized kesterite. They pointed out the importance of prolonged preheating treatment of the electrodeposited Cu/Sn/Zn stacks for ~3.3 h, thereby obtaining highest quality of CZTS films and PV cells [211,212]. Recent times have seen the replacement of water electrolytes with non-aqueous solvent. As an example, Dale et al. reported that ionic liquids allow for higher temperature usage and expansion of the electrochemical potential window [213]. This is advantageous as it makes room for the usage of high current densities during electrodeposition as there is no evolution of competing electrochemical hydrogen [213]. In another work, Steichen et al. reported an improved rate of average metallic deposition of 100 nm s^{-1} using liquid metal salts [214]. For co-electrodeposited films of CZTS, citrate salts as complexing agents have been replaced with pyrophosphates [215–218], with other works studying the effect of cell configuration on the stoichiometric uniformity of electrodeposited Cu–Zn–Sn alloys [219]. In order to obtain improved efficiencies for co-electrodeposited films, the use of electrolytes that contain quaternary-salt has been reported as an effective approach. A cell efficiency of 5.5% was reported by Ge et al. [220] for CZTS PV cell and has since reported an improved efficiency of 7.1% with great layer uniformity with reference to film morphology and stoichiometry by conducting systematic investigation, refined plating parameters and optimizing electrolyte [221].

6.3.3. *Spin-coating and doctor-blade approaches*

Spin coating and doctor-blade methods have been reported as routes of deposition for the kesterite absorber layers. These are useful for small cell investigations [181]. For spin-coated kesterite films, synthesized nanoparticles of CZTS are dissolved or dispersed in suitable solvent and subjected to high-speed spinning to achieve the desirable uniform spreading of the particles on the substrate. The spin-coated substrates are then annealed so as to eliminate the solvents. The spin-coating is repeated severally to achieve desirable film thickness [194,222,223]. These inks must be less viscose [194]. The solution-processed synthesis of kesterite through the use of hydrazine solvent employed the spin-coating approach for kesterite film deposition and has thus far achieved the best efficiency (12.6%) for kesterite PV cells [181]. On the other hand, doctor-blade approach requires very viscose inks [224]. These inks are dropped on the surface of the substrate and the ink is spread on the surface of the substrate by the movement of a blade at certain distance and constant velocity. For the ink to be highly viscose for effective use in doctor-blade coating, additives are often used. These additives are usually organic additives which sometimes leaves carbon and oxygen impurities in the deposited films thereby requiring addition high temperature annealing for their removal [224]. This becomes a problem on itself for the device as well as low yield usually encountered for fabrication of nanoparticle [225]. The highest efficiency reported for doctor-blade deposition approach is 9.3% [226].

Table 3 – List of device efficiencies reported for kesterite solar cells through alloying (cation substitutions).

Material	Alloying Element	Absorber layer Deposition method	Device Architecture	Crystal Structure	Band Gap (eV)	η (%)	Ref.
ACZTSSe	Ag (3%)	Spin-coating	Ag/ITO/i-ZnO/CdS/ACZTSSe/Mo/SLG	Kesterite	1.073	10.4	[241]
ACZTSe	Ag (10%)	Co-evaporation	MgF_2/Ni–Al/AZO/i-ZnO/CdS/ACZTSe/NaF/Mo/SLG	Kesterite	1.01	10.2	[242]
ACZCTS	Ag (5%), Cd (25%)	Spin-coating	SLG/Mo/ACZCTS/CdS/ITO/Ag	Kesterite	1.4	10.8	[281]
LCZTSSe	Li (6%)	Spin-coating	SLG/SiO_x/Mo/LCZTSSe/CdS/i-ZnO/AZO/Ni–Al/MgF_2	Kesterite	1.13	11.6	[246]
LCZTSSe	Li (12%)	Spin-coating	SLG/Mo/LCZTSSe/CdS/i-ZnO/ITO/Al	Kesterite	1.23	6.7	[282]
CZCTS	Cd (40%)	Magnetron sputtering	MgF_2/Al/ITO/i-ZnO/CdS/CZCTS/Mo/SLG	Kesterite	1.38	11.5	[247]
CZCTS	Cd (40%)	Spin-coating	Ag/AZO/i-ZnO/CdS/CZCTS/Mo/SLG	Kesterite	1.36	9.2	[248]
CMZTS	Mn (15%)	Spin-coating	SLG/Mo/CZTS/CMZTS/CdS/ITO/Ag	Kesterite	1.23	5.73	[259]
CMZTSSe	Mn (5%)	Spin-coating	SLG/Mo/CMZTSSe/CdS/i-ZnO/AZO/Ni–Al	Kesterite	1.06	8.9	[260]
CZGTSSe	Ge (25%)	Spray Pyrolysis	SLG/Mo/CZGTSSe/CdS/i-ZnO/ITO/Ni–Al	Kesterite	1.2	11.0	[191]
CZGTSSe	Ge (22%)	Co-evaporating	SLG/Mo/CZGTSSe/CdS/i-ZnO/AZO/Ag	Kesterite	1.11	12.3	[274]
CZSiTSe	Si (50%)	Ceramic route	No solar cell for silicon substituted kesterite materials	Kesterite and Wurtzite-stannite	1.3–1.7 eV	–	[280]

7. Strategy towards improved CZTS/Se (kesterite) PV performance (elemental subsitutions)

The crystal and device layer defects previously discussed have contributed to the low performance of the kesterite PV cell. To control these defects, research has gone into finding strategies to control/eliminate these defects. These research are channeled towards comprehending and elucidating the phase stability of the kesterite material, the link between processing guidelines and the effects they have on achieving high device performance and formation of single phased kesterite. The alloying of kesterite compounds with new metals has become one of the strategies adopted to tackle the antisite defects and large V_{oc} deficit. This strategy has been used in other solar cell devices like CIGS and CdTe [227–230]. This approach is important as it can tune the properties of the materials as well contribute to band engineering [105,231]. In this review we will be looking at some of the metals or cations that have been used as substitutions to the already existing metals in the kesterite compound, what impact they have had in giving insight into the realizing of improved devices. In substituting these constituent cationic elements, a sequential process is followed to maintain the overall valence state as well as the charge neutrality of the kesterite compound. Kesterite compounds take the form of I_2-II-IV-VI_4 composition [86,104]. This means it contains elements composed of 2 atoms with +1 oxidation state, 1 atom with +2 oxidation state, 1 atom with +4 oxidation state and 4 atoms of group 6 elements of −2 oxidation state. In maintaining this balanced neutral oxidation state, cations such as lithium and silver has been used to substitute copper; cadmium, iron, manganese and nickel, all in their +2 oxidation states have been explored as elemental substitutions for zinc; while germanium and silicon have been used to substitute tin in the kesterite material (see Fig. 20). Table 3 below presents comparative results and various parameters used in achieving some of the world record efficiencies for various alloyed compounds of the kesterite material and various deposition techniques that achieved these results.

7.1. *Impact of copper substitution in kesterite PV application*

Given the effect the Cu_{Zn} antisite defect has on the kesterite compounds and the large V_{oc} deficit of the PV devices of the kesterite compounds, silver (Ag) has been explored as suitable substitute for copper in all the variations of kesterite [232–234]. The use of Ag in-place of Cu through theoretical studies have established some improved properties due to the large atomic size of Ag thereby eliminating or reducing the Cu_{Zn} defect [105,232]. From reports, it is also useful for the reduction of the large V_{oc} deficit by reducing the concentration of defects experienced by most copper-based kesterite PV cells. In improving the properties of the kesterite compounds, silver zinc tin sulfides (AZTS) has been reported to give a larger grain size, high mobility and lower carrier density when compared to CZTS [104]. A high concentration of Ag/Sn ratio produces better cell performance than high concentration of

Cu/Sn ratio. Theoretical evaluations have found that due to very low concentration of Ag_{Zn} antisite defects, the Ag-based kesterite devices exhibit intrinsic or weak n-type conductivity [235,236]. This is attainable as Ag-based kesterite show high concentration of donor defects probably Zn_{Ag} as its dominant defect [237]. Some studies have reported tendency for silver-kesterite alloys of copper silver zinc tin sulfide selenide ($(Ag,Cu)_2ZnSn(S,Se)_4$, (ACZTSSe)), to change from p-type to n-type semiconductors with increasing atomic concentration of Ag to Cu. This was the case from the investigation by Shon et al. where they fabricated a kesterite device with architecture of FTO/AZTSe/MoO_3/ITO. They obtained a cell performance of 5%. This device exhibited n-type semiconductive properties due to the complete replacement of copper with silver. In a heterojunction PV cell ACZTSSe has been used as n-type layer with CZTS acting as the p-type layer [238]. An efficiency of 4.5% was achieved. Another theoretical evaluation found that 20% efficiency can be achieved by an architecture of an n-type CdS, p-type ACZTS and p^+-type CZTS [239]. Experimentally, Wong et al. fabricated a device based on the CdS/ACZTS/CZTS architecture. They obtained a device that had a V_{oc} gain of 50 mV and a device efficiency of 7.2% when compared to the device with CdS/CZTS architecture which gave a device efficiency of 4.9%. They also reported that the device made from ACZTS alone as the absorber layer gave a lower efficiency as a result of increased Ag content [240]. A 3% Ag to Cu ratio of ACZTSSe device was fabricated through solution processed technique and a 10.4% efficiency was achieved [241]. Another group achieved a 10.2% efficiency for ACZTSe device with 10% Ag ratio to Cu through co-evaporation technique [242]. These improvements to the antisite defects as well as reduced V_{oc} deficits of the kesterite solar cells have paved way for more research into optimizing and use of Ag as a viable substitute for Cu. The optimization study must establish control measures for amount of Ag suitable for a near commercialization efficiency for the kesterite device. It has been reported as well that almost 50% Ag content results in n-type semiconductive properties which will require a revitalization of the kesterite heterojunction architecture so as not to have band offset with CdS which is an n-type semiconductor in the conventional kesterite architecture [105,231].

Amongst the alkali group elements, Li^+ ions show better compatibility for Cu^+ replacement due to its ionic radius that is very close to Cu^+ ions [243]. It is also characterized by low energy of substitution for Li_{Cu} [243]. For a fully substituted compound with composition of Li_2ZnSnS_4, it exhibits a wider bandgap of 2.87 eV. In their work Yang et al. prepared alloyed $Li_xCu_{2-x}ZnSn(S,Se)_4$ thin films through a water-based precursor solution approach [244]. They observed a bandgap tuning range of 1.13 eV–1.31 eV when varying the ratio of Li/Cu from 0 to 0.29. Through obtained XRD results, increase in the Li/Cu ratio resulted in a shift to lower 2 theta value indicative of increased lattice parameters. This is the case as earlier stated the covalent radius for Li^+ ions are bigger (1.33 Å) than that of Cu^+ ions (1.27 Å) and thus infers the successful incorporation of lithium ions and replacement of copper ions in the crystal [243]. It was also observed that increase in the Li/Cu ratio resulted to a linear increase in the c-axis lattice parameter which obeys the Vegard's law. They also speculated the replacement of the body center Cu ion by that of lithium. Grain growth was observed to show no significant change as the ratio increased, indicative that lithium has no effect on the surface morphology of the films from the results obtained through cross section SEM. The architecture for their device was quartz/Mo/$Li_xCu_{2-x}ZnSn(S,Se)_4$. The obtained bandgap values increased with increasing 0 to 0.29 Li/Cu ratio (1.13–1.31 eV). To investigate this wider bandgap values, valence band maximum was obtained for the thin films for the varying Li/Cu ratio through ultraviolet photoemission spectroscopy (UPS). As the Li amount was increased both C_{BM} and V_{BM} moved towards lower energy with a less pronounced lower shift for C_{BM} which resulted in the wider bandgap values [244]. An increase in the conduction band offset for the interface between CdS and $Li_xCu_{2-x}ZnSn(S,Se)_4$ was observed due to the lower energy shift for the C_{BM} and V_{BM}. In taking the photovoltaic cell output for their material in relation to Li/Cu ratio, they observed an increase in the V_{oc} of the solar cells as Li was incorporated into the films. As obtained, the V_{oc} and PCE initially increased and then decreased with increasing amount of Li. At the ratio of 0.17 Li/Cu amount, the highest V_{oc} value of 459 mV was obtained with their best PCE value of 6.0%. A PCE value of 6.7% was rather obtained when the glass was changed from quartz to a soda lime glass at a Li/Cu ratio of 0.12 [244]. Quite notable in their work is the fact that the increase in Li amount did not have any change in the net carrier concentration of the absorber layer which is different for what has been observed in materials such as CIGSSe and CZTSSe solar cells when doped with the other group of alkali elements such as Na and K. Essentially, an improved carrier concentration of the absorber layer can be obtained when the defects at the grain boundaries are passivated thereby improving the crystallinity of the films, but in the case of their study, with the Li incorporating into the CZTSSe thin films and successfully replacing the corresponding Cu ions, effective hole concentration for the new material thin films didn't change with increased amount of Li.

Cabas-Vidani et al. prepared kesterite absorber layer with composition of $(Li_xCu_{1-x})_2ZnSn(S,Se)_4$ with x reaching up to 0.12 [245]. Through the combined studies such as XRD, EQE and other compositional measurements, they were able to confirm the successful incorporation of lithium and within the kesterite phase. With an increase of Li to $x = 0.07$, carrier concentration went up to 5×10^{-16} cm^{-3}. They found that the performance of the kesterite solar cell can be boosted by increased lithium fraction when in comparison with undoped absorbers. However, high lithium fraction gives no increment in the minority carrier lifetime of the absorber layer. V_{oc} deficit was decreased as a result of high majority carrier concentration as Li was incorporated. A champion PCE value of 11.6% was obtained at $x = 0.06$ with a 12.2% active area [246]. These improved effects on kesterite absorber layer makes it

necessary to further evaluate lithium alloying even at high concentrations. But methods have to be developed to minimize the loss of lithium in solution chemistry.

7.2. *Impact of zinc substitution in keserite PV application*

The close cation sizes and chemical electronic properties of Cu^{+} and Zn^{2+} in the kesterite system is the main reason for the formation of large number of Cu_{Zn} and Zn_{Cu} antisite defects [247–249]. The use of cadmium Cd as a substitute for Zn in the kesterite system is expected to increase the formation of Cu_{Cd} and Cd_{Cu} antisite defects which minimizes the disorder and band tailing observed in kesterite compounds [67,250,251]. The favorability of Cd is as a result of the large ionic radius of 0.94 Å when compared to that of Zn^{2+} and Cu^{+} which have ionic radius of 0.74 Å [252]. It has been suggested that the use of Cd to supplant Zn will inhibit or reduce the formation of the detrimental ZnS secondary phases and help in improving grain growth [104,253]. Theoretical calculations have shown that the Cd content ratio to Zn will determine how these disorders are alleviated [67,253,254]. The more the Cd content the less impact it has in mitigating the disorders. In fact, it results in detrimental outcome of phase transformation from kesterite to stannite. Low Cd content produces less disorder caused by Cu–Zn sublattices due to high formation energy of these antisite defects [67,251]. Yang et al. fabricated a device with absorber layer that has chemical composition of $Cu_2Cd_xZn_{1-x}SnS_4$ (CCZTS) thin films through spin-coating of the cation precursors on the substrate and sulfurization process. Thin films with varying Cd content were prepared and observed a phase transition from kesterite to stannite when the Cd content was high. They also reported on improved grain size for optimized Cd content. Their findings align with the theoretical evaluations earlier stated [254]. Tan et al. reported device containing $Cu_2Zn_{1-x}Cd_xSnS_4$ (CZCTS) thin film absorber layer through low cost sol-gel method. They noticed that the bandgap and crystal structure of the CZCTS were affected by the content ratio of Cd to Zn. ZnS secondary phases were dramatically reduced with improved grain size when partial substitution of Zn with Cd occurred at ratios between 0 and 40%. Through optimization of the device parameters especially the Cd ratio, the device efficiency was remarkably improved from 5.3% to 9.24% (40% Cd content) [248]. Huang et al. produced a device that achieved beyond 11% device efficiency by maintaining a 40% Cd content during alloying of the kesterite compound. They reported an improved device with reduced band tailing as a result of the incorporation of Cd into the composition [247]. The reduced band tailing was confirmed by the decrease in difference of the photoluminescence and optical bandgap together with decreased URBACH energy. They also obtained a reduced V_{oc} deficit of more than 100 mV for the best Cd-substituted kesterite (40% ratio). These reports have shown that the incorporation of Cd into the absorber layer of the kesterite PV cell is able to bring about an alteration of the characteristic acceptor defects near the valence band by making them shallower hence, improving the cell performance. They suggest positive pathway for the use of Cd as a viable substitute for Zn as a way of improving on the kesterite device when the toxic nature of Cd is not considered.

Manganese has been used to substitute zinc in this material to form compound of CMTS where M represents manganese. It has been widely reported that CMTS materials exhibit the stannite structure [255]. With large ionic radii 1.40 Å, it is suitable to tackle the Cu_{Zn} antisite defects. Its incorporation into the CZTSSe material causes a change in property, one significant change is the formation of the stannite phase rather than the kesterite phase [255]. In their work Liang et al. found that the CMTS semiconductor crystals exhibit magnetic properties and took the zinc blende and wurtzite type structures [256]. Most of the reported work of CMTS has been focused on its magnetic, optical and electrical properties. Chen et al. reported from their work that CMTS which is a non-lethal material exhibited high absorption coefficient similar to that of CZTS (10^4 cm^{-1}) with bandgap ranging from 1.0 to 1.4 eV which is close to the optimum bandgap value for solar cell applications [257]. Mn is more abundant (1100 ppm) than Zn (79 ppm) making a suitable substitute for zinc. In another of their work, Chen et al. explored the effect of varying Mn content in a sol gel prepared $Cu_2Mn_xZn_{1-x}SnS_4$ (CMZTS) thin films as it relates to the transformation from kesterite phase to stannite phase [258]. The bandgap of the material was reduced from 1.51 eV to 1.23 eV as Mn content was increased. Due to the larger Mn cation radius than that of Zn, an increase in Mn content resulted in phase transformation from kesterite to stannite. Raman shifts to lower wavenumber was also observed as Mn content was increased which is attributed to the lower bond stretching force constant. Poor cell performance has been reported for CMTS and CMTSSe materials as a result. This is attributed to high carrier concentration. For partially alloyed materials, Lie et al. fabricated a solar device via sol-gel spin coating method composed of $Cu_2Mn_xZn_{1-x}SnS_4$ (CMZTS) with device architecture of Mo/CMZTS/CdS/ITO/Ag with $x = 0$ to 1 to investigate the effect of Mn on the performance of the device [259]. With comparison to fabricated control CZTS device, there was an improvement in the device performance from 4.4% for CZTS device to 5.2% for $CM_{0.15}Z_{0.85}TS$ which is champion efficiency for materials in CMZTS composition. They also reported improvement in the V_{oc} value for CMZTS device when compared to the control CZTS device. The optimum cell efficiency was obtained at $x = 0.15$ and noticed decrease in efficiency as the Mn content was increased. Li et al. used machine learning to predict amount of Mn content for a $Cu_2Mn_xZn_{1-x}(S,Se)_4$ device that will yield better cell performance [260]. From the results obtained through this prediction they found that the cell will perform better at 8% Mn content. For the experimental result, a device with architecture of Mo/CMZTSSe/CdS/i-ZnO/Al:ZnO/Ni–Al was evaluated. A champion cell performance was obtained at 5% Mn content (8.9%). As the concentration of Mn was increased, the cell performance decreased as a result of increased carrier concentration and quenching of the radiative recombination indicative of need for better optimization for improved cell improvement. These enhancements for both CMZTS and CMZTSSe devices are attributed to refined grain growth, improved interfacial interaction between CdS layer/absorber layer and change in majority in defects from Cu_{Zn} to V_{Cu}.

The abundance and stability of iron has made it a considerable element for substitution of zinc in kesterite materials [261]. In reality, the kesterite mineral exist as an alloy composed of $Cu_2(Zn,Fe)SnS_4$ thereby making it quite an easy approach to synthesize and incorporate iron into the structure as a way to improve on this semiconductor. With properties ranging from great absorption coefficient (10^4 cm^{-1}) to bandgap between 1 and 1.5 eV, Cu_2FeSnS_4 (CFTS) shows great potential for PV application [262]. There is little literature reporting on the application of CFTS into PV devices. 0.07% solar cell efficiency was reported for an RF magnetron fabricated CFTS absorber layer with device architecture of glass/Mo/CFTS/CdS/i-ZnO/Al:ZnO [263]. However, Pal et al. reported solar cell efficiency of 2.95% through SILAR method for the absorber layer [264]. They also replaced the buffer layer with Bi_2S_3 buffer which shows a much preferable band alignment at the interface as measured from scanning tunneling spectroscopy (STS) [264]. In terms of alloying, Fe^{2+} ionic radius (0.66 Å) is similar to that of Zn^{2+} (0.64 Å) which enhances the ease of formation of solid solution of $Cu_2Fe_{1-x}Zn_xSnS_4$ (CFZTS) [265]. In literature, there has been reports of CFZTS thin films changing from kesterite to stannite phase as well as bandgap increase from 1.35 eV to 1.7 eV as Fe content was increased [266]. Moreover, detrimental effect on quasi-Fermi splitting has been reported from a combinatorial study in CFZTS materials even at low Fe content, therefore a positive use of doping Fe draws skepticism as transition metals containing partially filled d-orbitals produce deep defect states in CZTSSe as observed in CIGS devices [267,268].

Just like the case of Fe, Nickel ion (Ni^{2+}) with ionic radius of 0.69 Å which is close to that of Zn^{2+} ion (0.74 Å) can be used to substitute zinc [265]. Some studies have reported the potential of Ni substitution of Zn in CZTS compound in enhancing the electrical conductivity and reducing the optical band gap [269]. CNTS shows remarkable properties for solar cell application such as high optical absorption coefficient of 10^6 cm^{-1}, band gap value ranging from 1.5 to 1.6 eV with a zinc blende crystal structure [270]. However, first principles density functional theory calculations (DFT) projects that the defect complex seen in Cu_2NiSnS_4 (CNTS) will produce localized in-gap states [255]. Few devices have been reported with CNTS absorber layer. Rondiya et al. fabricated a material with device architecture of glass/Mo/CNTS/CdS/Al–ZnO/Al which gave an efficiency of 0.09% [270]. Ghosh et al. on the other hand reported a device with architecture ITO/ZnO-nanorods/ZnS/CNTS/Au giving an efficiency of 2.71% [271].

7.3. *Impact of tin substitution in kesterite PV application*

Germanium in the stable oxidation state of +4 can be used to successfully substitute Sn in kesterite compounds. It has seen a level of success in its use as a dopant in kesterite PV cells achieving an efficiency of 11.8% [105,171]. It is expected to deliver positively towards an improved kesterite PV cell when alloyed. Remarkable device efficiencies ranging from 9.4 to 12.3% has been reported for Ge-alloyed kesterite devices [272–275]. The first optimized Ge-alloyed kesterite with a sulfur-selenide composition CZGTSSe gave a cell efficiency of 9.4% with 30% Ge content relative to Sn [272]. This CZGTSSe device gave improved V_{oc} value when compared to CZTSSe. There was an improvement in minority carrier lifetime, which is a boost to the efficiency and device performance of the kesterite PV cell. A 10% efficient kesterite device was published by Kim et al. with 40% Ge-content by improving on the annealing process [273]. Subsequently an 11% efficient device was fabricated by Hillhouse et al. by studying through almost all possible percentage ratios substitution (ranging from 0 to 90%) of Sn with Ge [191]. The 11% efficiency was obtained at 25% Ge-content with impressive reduced V_{oc} deficit. The Ge-content above the optimal percentage gave results that has abysmal drop in cell conversion efficiency ranging from unfavorable band alignment between the kesterite and buffer CdS layer to deep defects that are 0.8 eV above the valence band as increased Ge-content increased the bandgap value [105,191]. The best Ge-alloyed kesterite gave a cell conversion efficiency of 12.3% [274], which is close to 12.6% of the state of art kesterite PV cell of CZTSSe. The 12.3% efficiency for CZGTSSe was achieved with 22% Ge-content and showed impressive reduced V_{oc} deficit. The reduction in V_{oc} deficit was due to decrease in band tailing through the control of the Ge/(Sn + Ge) ratio. Other improvements in carrier lifetime as well as high fill-factor (FF) value of 73% from the cell indicate reduced carrier recombination at the kesterite absorber layer, CdS buffer layer interface alongside the space region and improved absorbing quality [105,274]. These improvements and progress achieved with Ge-alloyed kesterites suggest a good pathway towards highly efficient and commercialization of kesterite device by controlling the Ge-content.

Another viable element that can be used in substituting tin ion (Sn^{4+}) in CZTS is the stable silicon ion, Si^{4+}. With earth abundance (2.82×10^5 ppm) that surpasses that of all kesterite elements, it has be suggested to be incorporated into kesterite lattice to replace the Sn-sites which are usually marred with volatility and minimizes the formation of Sn^{2+} [276,277]. $Cu_2ZnSiSe_4$ (CZSiSe) takes wurtzstannite crystal structure [278]. Through first principles calculations, there was reported the possibility of miscibility in varying compositional range but there has not been any experimental work to back it up [279]. Some studies have found that Si does not combine with the kesterite lattice, rather it can only form a Sn-free CZSiSe which gives very low photocurrent for complete devices [279]. Hamdi et al. is the only work that has reported successfully form alloy of $Cu_2Zn(Si_xSn_{1-x})S_4$ through ceramic route forming alloys up to $x = 0.5$. Obtained bandgap value for this compound was 1.7 eV which can be applied in tandem solar cell [280]. Although with the success of forming an alloy, there has not been any success in obtaining a working solar cell. Although tin substitution by incorporation of silicon can be achieved, synthesizing the material however is marred by elevated formation energy.

8. Further prospects: innovations for improved CZTS/Se device (kesterite) efficiency

8.1. *Back contact layer interface*

Molybdenum (Mo) have been used as the back contact for CIGS solar cells due to its stability at high processing temperatures and resistance to alloying with Cu [283–285], excellent

adhesion between the soda lime glass (SLG) substrates and CIGS absorbers, and low-resistance contact to the CIGS absorber. The importance of $MoSe_2$ was demonstrated to reduce the contact recombination and contact resistance experienced at the interface of CIGS absorber layer and Mo back contact [285]. CZTS device structure replicates that of CIGS without the consideration of the material system difference of both materials [92]. Different from the case of CIGS, the Mo thin film back contact has been demonstrated to have some detrimental effects on CZTS device performance [286]. CZTSe is not stable at high processing temperature (500–600 °C) in the presence of Mo [287]. Equation (1) shows the decomposition of $Cu_2ZnSnS(e)_4$

$$2Cu_2ZnSnS(e)_4 \leftrightarrow 2Cu_2S(e) + 2ZnS(e) + 2SnS(e) + 2S(e)_{(g)} \quad (1)$$

Equation (2) describes the reaction that generates $MoS(e)_2$ at the CZTS(e)/Mo interface:

$$Mo + 2S(e) \rightarrow MoS(e)_2 \quad (2)$$

The thermal instability of the CZTS(e)/Mo during thermal processing is given by the combination of Equations (1) and (2):

$$2Cu_2ZnSnS(e)_4 + Mo \rightarrow 2Cu_2S(e) + 2ZnS(e) + 2SnS(e) + MoS(e)_2 \quad (3)$$

The free energy change of the reaction of Equation (3) was calculated to be −100 kJ for CZTSe and −150 kJ for CZTS at 550 °C. Such negative free energy changes are indicative that the decomposition reaction is thermodynamically favorable and that the CZTS(e)/Mo interface may become unstable [286,287]. The instability of the Mo back contact can potentially cause losses of V_{oc}, J_{sc} and *FF* in the CZTS device if not mitigated by film preparation conditions or device structure [287].

Alternative back contact metals have been explored to mitigate the problem encountered with the decomposition and contact resistance of the CZTS(e)/Mo interface. The metals that have been explored include: gold (Au), tungsten (W), palladium (Pd), platinum (Pt) and nickel (Ni) [288]. Pd and Ni were observed to diffuse into the CZTSSe absorber extensively after annealing at 570 °C for 30 min, while Au did not react with the chalcogens, W reacted partially and Pt reacted completely. Therefore, Pd, Ni and Pt are not suitable as back contact materials under the conditions examined. W and Au are eligible contact materials because of their ability to enhance short circuit current (J_{sc}). In contrast to Mo, Au is a highly reflective back contact and increases the absorption of photons in the long wavelength range, therefore enhancing J_{sc} [288]. W, may serve to passivate the CZTSSe absorber and improve the collection of carriers generated deep in the absorber [200]. However, Mo remains the best choice material for a back contact, so far (i.e., it is used for all record-performing devices) and achieved the highest conversion efficiency of 4.8% in this particular study. In contrast, cells with W and Au back contacts demonstrated deteriorated efficiencies of around 3.9%. The reduced efficiency was mainly attributed to decreases in fill factor (*FF*). In the case of a W back contact, a ~350-nm-thick $W(S,Se)_2$ layer was generated, which increased the series resistance and reduced *FF*. For the Au back contact, a high density of voids was observed in the CZTSSe absorber, resulting in a very low shunt resistance and deteriorated *FF*. Of course, with all of the above results, it is important to keep in mind that the suitability of a back-contact material will significantly depend not only on the choice of metal, but also on the specific processing approach used to deposit the CIGS or CZTSSe layer on top. For some of the above-mentioned back contact choices, it is possible that with optimization of the processing for the specific back contact material (which may not be the same best conditions as for deposition on Mo), high performance may be achieved [288].

An intermediate layer between the CZTS(e)/Mo interface have been explored as a solution to the problem described above [289–292]. An ultra-thin and intentionally introduced carbon layer has recently been developed to act as an intermediate layer between the kesterite absorber and the Mo back contact [293], in order to reduce the void-induced series resistance that is likely to arise in this region of the device. The evaporated carbon intermediate layer increases J_{sc} and conversion efficiency of CZTS devices with the absorbers fabricated by two-stage preparation, i.e., non-vacuum (sol–gel) or vacuum (sputtering) methods followed by high temperature sulfurization. Meanwhile, the carbon intermediate layer does not deteriorate V_{oc} and *FF*. The transmission electron microscopy (TEM) image and corresponding energy dispersive spectroscopy (EDS) mappings of the CZTS device with a carbon intermediate layer fabricated by the sol–gel method shows that carbon adheres on the inner walls of voids. By comparing EDS line scans on the CZTS devices with and without the carbon intermediate layer, it was confirmed that the carbon sticking on the inner walls of voids arose from the intentionally introduced carbon layer rather than the precursor solution used in the sol–gel method. The carbon aggregation better connects void-containing CZTS and the Mo back contact, which reduces the series resistance R_s and leads to increased J_{sc} and improved conversion efficiency [293].

8.2. *Buffer layer interface*

Alternative buffer layers other than the toxic CdS layer has been considered to be used for better band alignment in making kesterite solar cells [294–297]. The heterojunctions formed between $Cu_2ZnSn(S_xSe_{1-x})_4$ (CZTSSe) and three Cd-free n-type buffers, ZnS, ZnO, and In_2S_3, were studied using femtosecond ultraviolet photoemission and photovoltage spectroscopy [295]. A small positive spike conformation of 0.15 eV was produced between the hydrazine-processed CZTSSe absorber and an In_2S_3 buffer layer deposited by CBD, which reduces the interface recombination and does not form a barrier for the light-generated electrons. Hence a large J_{sc} and reasonable V_{oc} and *FF* are obtained. A CZTSSe solar cell with such an In_2S_3 buffer layer achieved an efficiency of 7.19%, which was comparable to the efficiency of 7.75% made from the analogous CdS buffer layer [295].

9. Conclusion

Since the discovery of the mineral ore CZTS and its semiconductive properties, it has become vital to find ways to produce the material in large scale by finding suitable

synthesis route as well as convenient deposition approach of the kesterite absorber layer on molybdenum coated soda lime glass substrate. There are three distinctive methods used for the synthesis of kesterite nanoparticles (exploring the improved material properties towards quantum confinement as a result of reduced molecular size). These three methods (solvothermal, hydrothermal and hot injection methods) have proven successful in the synthesis of the kesterite nanoparticles. With the solvothermal and hydrothermal method needing addition heating, the takeaway is that for successful synthesis of the kesterite phase, proper choice of temperature is needed to eliminate the presence of secondary phases, as the presence of the secondary phases are detrimental to the final application of the nanoparticles. It is very vital to anneal these nanoparticles especially in the presence of sulfur to obtain pure crystalline kesterite phase. Likewise, the choice of best deposition approach for the deposition of the kesterite absorber layer is very vital for the overall performance of the device. Here we discussed the various deposition approaches that have been used for kesterite deposition and explained their contributive factors towards better performing devices. Kesterite, with properties such as optimal bandgap value of 1.5 eV, absorption coefficient of 10^4 cm^{-1} and composition of earth abundant non-toxic elements has made it an impressive p-type semiconductor material for PV application. Largely, PV cells made from this material has suffered from high V_{oc} deficit and antisite defects thereby limiting it from reaching its theoretical efficiency of 30%. Strategies such as alloying (cationic substitutions) have emerged as viable pathway to mitigate these limiting factors and eventually achieve better PCE. By exploring these strategies in this review, we were able to highlight alloying strategy of the kesterite compound and shown how remarkable outputs can be achieved by substituting the constituent atoms of the kesterite compounds with certain cationic elements. The improvements brought by these alloying elements depend on a controlled ratio. Ag and Li were used to substitute for Cu, Cd, Mn, Ni and Fe in place of Zn and Ge and Si for Sn. These elements at an optimized ratio improved the properties of the kesterite compound by lowering the large V_{oc} deficit as well as limiting the formation of the detrimental antisite defects. With the improvements reported for all the alloyed kesterite and doped ones, none has gotten to the state-of-the-art efficiency so far recorded for the solid solution compound (CZTSSe) of kesterite, which has a PCE value of 12.6%. The best alloyed kesterite came close to this value with just 22% Ge-content and gave PCE value of 12.3%.

These impressive improvements that has been reported for the alloyed kesterite compounds and devices must be explored and researched more in terms of optimization of the alloying element content to viably increase the PCE of the kesterite PV cells. Characterization techniques that are uniquely specific in exploring the crystal structure of the kesterite compounds must be adopted to fully explain the reason for the antisite defect formations, band tailing effects and the large V_{oc} deficit. With the specified information realized from this approach it becomes easier to tailor research easily to very concrete strategies that will improve the kesterite PV cells. Doping as one of the strategies has contributed to improved kesterite devices. Figure 20 shows the major dopant elements that have been used in kesterite materials. More dopants should be explored to improve the kesterite device. Doped-lanthanide oxysulfides/selenides phosphors have been explored for their good photoluminescence properties. Recently a monocrystalline silicon solar cell was improved by doping it with terbium-doped gadolinium oxysulfide and an impressive efficiency increase of about 3.6% was obtained. For the undoped silicon solar cell, an PCE of 16.43% was obtained while doping with terbium-doped gadolinium oxysulfide gave a PCE of 17.02% [298]. Given the ease of substitution in CZTS semiconductors than silicon and considering the successful improvement realized in cell efficiency for a rigid material like silicon solar cell, the flexibility of CZTS materials and ease of doping necessitates the need to explore the use of these phosphors in the kesterite PV to improve on their properties and device performance. Also, the use of group v elements as dopants for CdTe PV devices has resulted in improved device efficiency of over 20% [299,300]. Group V dopants offer a path to increase the hole density and stability. This is the case as evidenced by the results obtained which were consistent with recent diffusion experiments indicating that As, P and Sb diffuse more slowly than group I elements [300]. The binary to quaternary formation as explained in section 3 and 4, provides the pathway for consideration of the use of these group V dopants in quaternary compounds of CZTS due to their success in binary compound of CdTe devices as a way of improving the device performance of CZTS PV cells.

Declaration of Competing Interest

The authors declare that they have no known competing financial interests or personal relationships that could have appeared to influence the work reported in this paper. This research work was funded by the National Research Foundation (NRF) of South Africa Grant Reference Number: BS170512230689.

REFERENCES

[1] Perlin J. From space to Earth: the story of solar electricity. 1999. From Sp. to Earth.
[2] Fraas L, Partain L. In: Solar cells and their applications. 2nd ed. Hoboken, NJ, USA: John Wiley & Sons, Inc.; 2010. https://doi.org/10.1002/9780470636886.
[3] Chapin DM, Fuller CS, Pearson GL. A new silicon p-n junction photocell for converting solar radiation into electrical power. J Appl Phys 1954. https://doi.org/10.1063/1.1721711.
[4] 2019 Hydropower status report: sector trends and insights. 2019.
[5] Hydropower explained - U.S. Energy information administration (EIA). 2020. https://www.eia.gov/energyexplained/hydropower/. [Accessed 16 October 2020].
[6] Zrelli MH. Renewable energy, non-renewable energy, carbon dioxide emissions and economic growth in selected Mediterranean countries. Environ Econ Pol Stud 2017;19:691–709. https://doi.org/10.1007/s10018-016-0170-5.

[7] Renewable energy in africa is set to surge by 2040, IEA says. Our World; 2020. https://ourworld.unu.edu/en/renewable-energy-in-africa-is-set-to-surge-by-2040-iea-says. [Accessed 16 October 2020].
[8] South African Department of Energy. Renewable energy. Republic of South Africa: Department: Energy; 2010.
[9] National Geographic. Renewable energy, facts and information. 2019. https://www.nationalgeographic.com/environment/energy/reference/renewable-energy/ (accessed October 7, 2019).
[10] International Energy Agency. IEA - Report. Int J Renew Energy Res 2016. https://doi.org/10.1108/IJLM-10-2012-0126.
[11] Reddy KS, Mallick TK, Chemisana D. Solar power generation. Int J Photoenergy 2013;2013. https://doi.org/10.1155/2013/950564.
[12] Kannan N, Vakeesan D. Solar energy for future world: - A review. Renew Sustain Energy Rev 2016;62:1092–105. https://doi.org/10.1016/j.rser.2016.05.022.
[13] Sai Gautam G, Senftle TP, Alidoust N, Carter EA. Novel solar cell materials: insights from first-principles. J Phys Chem C 2018;122:27107–26. https://doi.org/10.1021/acs.jpcc.8b08185.
[14] Ferrazza F. In: Crystalline silicon: manufacture and properties. 3rd ed. Elsevier Ltd; 2017. https://doi.org/10.1016/B978-0-12-809921-6.00004-5.
[15] Vallejo OR, Sánchez M, Pal M, Espinal R, Llorca J, Sebastian PJ. Synthesis and characterization of nanoparticles of CZTSe by microwave-Assisted chemical synthesis. Mater Res Express 2016;3. https://doi.org/10.1088/2053-1591/3/12/125017.
[16] Lee TD, Ebong AU. A review of thin film solar cell technologies and challenges. Renew Sustain Energy Rev 2017. https://doi.org/10.1016/j.rser.2016.12.028.
[17] Auf Der Maur M, Albes T, Gagliardi A. Thin-film solar cells. In: Handb. Optoelectron. Device Model. Simul. Lasers, Modul. Photodetectors, Sol. Cells, Numer. Methods; 2017. https://doi.org/10.4324/9781315152318.
[18] Chopra KL, Paulson PD, Dutta V. Thin-film solar cells: an overview. Prog Photovoltaics Res Appl 2004. https://doi.org/10.1002/pip.541.
[19] Karazhanov S, Kharton V. Novel materials for solar cells and related technologies. Mater Lett 2018;228:450. https://doi.org/10.1016/j.matlet.2018.06.078.
[20] Green MA, Hishikawa Y, Dunlop ED, Levi DH, Hohl-Ebinger J, Yoshita M, et al. Solar cell efficiency tables (Version 53). Prog Photovoltaics Res Appl 2019;27:3–12. https://doi.org/10.1002/pip.3102.
[21] Ascent Solar thin-film named one of Time's 50 best inventions. CleanenergyauthorityCom; 2020. https://www.cleanenergyauthority.com/solar-energy-news/ascent-solar-thin-film-recognized-by-time-s-mag-112911. [Accessed 18 October 2020].
[22] Abou-Ras D, Kirchartz T, Rau U. Advanced characterization techniques for thin film solar cells. 2011. https://doi.org/10.1002/9783527636280.
[23] electricaltechnology.org. How to make a simple solar cell? Work Photovolt Cells 2017:1–10.
[24] Green MA. The path to 25% silicon solar cell efficiency: history of silicon cell evolution. Prog Photovolt Res Appl 2009. https://doi.org/10.1002/pip.892.
[25] Masuko K, Shigematsu M, Hashiguchi T, Fujishima D, Kai M, Yoshimura N, et al. Achievement of more than 25% conversion efficiency with crystalline silicon heterojunction solar cell. IEEE J Photovolt 2014. https://doi.org/10.1109/JPHOTOV.2014.2352151.
[26] Solar T. Trina solar announces new efficiency record of 21.25% efficiency for multi-crystalline silicon solar cell. 2015. https://www.trinasolar.com/us/news/trina-solar-announces-new-efficiency-record-2125-efficiency-multi-crystalline-silicon-solar (accessed February 18, 2021).
[27] Battaglia C, Cuevas A, De Wolf S. High-efficiency crystalline silicon solar cells: status and perspectives. Energy Environ Sci 2016;9:1552–76. https://doi.org/10.1039/c5ee03380b.
[28] Miles RW, Hynes KM, Forbes I. Photovoltaic solar cells: an overview of state-of-the-art cell development and environmental issues. Prog Cryst Growth Char Mater 2005. https://doi.org/10.1016/j.pcrysgrow.2005.10.002.
[29] Carlson DE, Wronski CR. Amorphous silicon solar cell. Appl Phys Lett 1976. https://doi.org/10.1063/1.88617.
[30] Staebler DL, Wronski CR. Reversible conductivity changes in discharge-produced amorphous Si. Appl Phys Lett 1977. https://doi.org/10.1063/1.89674.
[31] Matsui T, Sai H, Suezaki T, Matsumoto M, Saito K, Yoshida I, et al. Development of highly stable and efficient amorphous silicon based solar cells. In: 28th Eur. Photovolt. Sol. Energy Conf. Exhib.; 2013.
[32] Sai H, Matsui T, Koida T, Matsubara K, Kondo M, Sugiyama S, et al. Triple-junction thin-film silicon solar cell fabricated on periodically textured substrate with a stabilized efficiency of 13.6%. Appl Phys Lett 2015. https://doi.org/10.1063/1.4921794.
[33] Iftiquar MS, Chul J, Lee J, Jang J, Lee Y-J, Yi J. Single- and multiple-junction p-i-n type Amorphous silicon solar cells with p-a-Si1-xCx:H and nc-Si:H films. In: Photodiodes - from Fundam. To Appl. InTech; 2012. https://doi.org/10.5772/51732.
[34] Bai Z, Yang J, Wang D. Thin film CdTe solar cells with an absorber layer thickness in micro- and sub-micrometer scale. Appl Phys Lett 2011. https://doi.org/10.1063/1.3644160.
[35] El Chaar L, Lamont LA, El Zein N. Review of photovoltaic technologies. Renew Sustain Energy Rev 2011. https://doi.org/10.1016/j.rser.2011.01.004.
[36] Romeo N, Bosio A, Menossi D, Romeo A, Aramini M. Last progress in CdTe/CdS thin film solar cell fabrication process. Energy Procedia 2014;57:65–72. https://doi.org/10.1016/j.egypro.2014.10.009. Elsevier Ltd.
[37] Krum S. First Solar achieves yet another cell conversion efficiency world record. First Sol Media; 2016. p. 1–2.
[38] Ali MH, Moon MMA, Rahman MF. Study of ultra-thin CdTe/CdS heterostructure solar cell purveying open-circuit voltage ~1.2 v. Mater Res Express 2019;6:095515. https://doi.org/10.1088/2053-1591/ab3089.
[39] Wagner S, Shay JL, Migliorato P, Kasper HM. CuInSe2/CdS heterojunction photovoltaic detectors. Appl Phys Lett 1974;25:434–5. https://doi.org/10.1063/1.1655537.
[40] Kazmerski LL, White FR, Morgan GK. Thin-film CuInSe2/CdS heterojunction solar cells. Appl Phys Lett 1976;29:268–70. https://doi.org/10.1063/1.89041.
[41] Jackson P, Hariskos D, Wuerz R, Kiowski O, Bauer A, Friedlmeier TM, et al. Properties of Cu(In,Ga)Se2 solar cells with new record efficiencies up to 21.7%. Phys Status Solidi - Rapid Res Lett 2015. https://doi.org/10.1002/pssr.201409520.
[42] Kuo SY, Hsieh MY, Hsieh DH, Kuo HC, Chen CH, Lai FI. Device modeling of the performance of Cu(In,Ga)Se2 solar cells with V-shaped bandgap profiles. Int J Photoenergy 2014;2014. https://doi.org/10.1155/2014/186579.
[43] Vasekar P, Dhakal T. Thin film solar cells using earth-abundant materials. In: Sol. Cells - Res. Appl. Perspect. InTech; 2013. https://doi.org/10.5772/51734.

[44] Gamyanin GN, Anikina EY, Bortnikov NS, Alpatov VV. The Prognoz silver-polymetallic deposit, Sakha (Yakutia): chemistry and zoning of ore veins. Geol Ore Depos 2003.
[45] Dong H, Schnabel T, Ahlswede E, Feldmann C. Polyol-mediated synthesis of Cu2ZnSn(S,Se)4 kesterite nanoparticles and their use in thin-film solar cells. Solid State Sci 2014;29:52–7. https://doi.org/10.1016/j.solidstatesciences.2014.01.006.
[46] Azimi H, Hou Y, Brabec CJ. Towards low-cost, environmentally friendly printed chalcopyrite and kesterite solar cells. Energy Environ Sci 2014;7:1829–49. https://doi.org/10.1039/c3ee43865a.
[47] Wang W, Winkler MT, Gunawan O, Gokmen T, Todorov TK, Zhu Y, et al. Device characteristics of CZTSSe thin-film solar cells with 12.6% efficiency. Adv Energy Mater 2014;4:1301465. https://doi.org/10.1002/aenm.201301465.
[48] Katagiri H, Jimbo K, Maw WS, Oishi K, Yamazaki M, Araki H, et al. Development of CZTS-based thin film solar cells. Thin Solid Films 2009;517:2455–60. https://doi.org/10.1016/j.tsf.2008.11.002.
[49] Todorov TK, Reuter KB, Mitzi DB. High-efficiency solar cell with earth-abundant liquid-processed absorber. Adv Mater 2010;22:E156–9. https://doi.org/10.1002/adma.200904155.
[50] Cai ZH, Narang P, Atwater HA, Chen S, Duan CG, Zhu ZQ, et al. Cation-mutation design of quaternary nitride semiconductors lattice-matched to GaN. Chem Mater 2015;27:7757–64. https://doi.org/10.1021/acs.chemmater.5b03536.
[51] Walsh A, Chen S, Wei SH, Gong XG. Kesterite thin-film solar cells: advances in materials modelling of Cu 2 ZnSnS 4. Adv Energy Mater 2012;2:400–9. https://doi.org/10.1002/aenm.201100630.
[52] Nitsche R, Sargent DF, Wild P. Crystal growth of quaternary 122464 chalcogenides by iodine vapor transport. J Cryst Growth 1967;1:52–3. https://doi.org/10.1016/0022-0248(67)90009-7.
[53] Chen S, Gong XG, Walsh A, Wei SH. Electronic structure and stability of quaternary chalcogenide semiconductors derived from cation cross-substitution of II-VI and I-III-VI2 compounds. Phys Rev B - Condens Matter Mater Phys 2009;79:165211. https://doi.org/10.1103/PhysRevB.79.165211.
[54] Chen S, Gong XG, Walsh A, Wei SH. Crystal and electronic band structure of Cu2 ZnSn X4 (X=S and Se) photovoltaic absorbers: first-principles insights. Appl Phys Lett 2009;94:041903. https://doi.org/10.1063/1.3074499.
[55] Schorr S. The crystal structure of kesterite type compounds: a neutron and X-ray diffraction study. Sol Energy Mater Sol Cells 2011;95:1482–8. https://doi.org/10.1016/j.solmat.2011.01.002.
[56] Liu D, Han D, Huang M, Zhang X, Zhang T, Dai C, et al. Theoretical study on the kesterite solar cells based on Cu2ZnSn(S,Se)4 and related photovoltaic semiconductors. Chinese Phys B 2018;27. https://doi.org/10.1088/1674-1056/27/1/018806.
[57] Katagiri H, Sasaguchi N, Hando S, Hoshino S, Ohashi J, Yokota T. Preparation and evaluation of Cu2ZnSnS4 thin films by sulfurization of E-B evaporated precursors. Sol Energy Mater Sol Cells 1997. https://doi.org/10.1016/S0927-0248(97)00119-0.
[58] Bonazzi P, Bindi L, Bernardini GP, Menchetti S. A model for the mechanism of incorporation of Cu, Fe and Zn in the stannite - Këesterite series, Cu2FeSnS4 - Cu2ZnSnS4. Can Mineral 2003. https://doi.org/10.2113/gscanmin.41.3.639.
[59] Ito K, Nakazawa T. Electrical and optical properties of stannite-type quaternary semiconductor thin films. Jpn J Appl Phys 1988;27:2094–7. https://doi.org/10.1143/JJAP.27.2094.
[60] Paier J, Asahi R, Nagoya A, Kresse G. Cu2 ZnSnS4 as a potential photovoltaic material: a hybrid Hartree-Fock density functional theory study. Phys Rev B - Condens Matter Mater Phys 2009;79. https://doi.org/10.1103/PhysRevB.79.115126.
[61] Vu TV, Lavrentyev AA, Gabrelian BV, Tong HD, Parasyuk OV, Khyzhun OY. Calculations within DFT framework of the electronic and optical properties of quaternary sulfide Tl 2 PbSiS 4 , a prospective optoelectronic semiconductor. Comput Condens Matter 2019;21. https://doi.org/10.1016/j.cocom.2019.e00392.
[62] Persson C. Electronic and optical properties of Cu2ZnSnS4 and Cu2ZnSnSe4. J Appl Phys 2010;107:053710. https://doi.org/10.1063/1.3318468.
[63] Botti S, Kammerlander D, Marques MAL. Band structures of Cu2 ZnSnS4 and Cu2 ZnSnSe4 from many-body methods. Appl Phys Lett 2011;98:241915. https://doi.org/10.1063/1.3600060.
[64] Bonazzi P, Bindi L, Bernardini GP, Menchetti S. A model for the mechanism of incorporation of Cu, Fe and Zn in the stannite - Këesterite series, Cu2FeSnS4 - Cu2ZnSnS4. Can Mineral 2003. https://doi.org/10.2113/gscanmin.41.3.639.
[65] Chen S, Walsh A, Luo Y, Yang JH, Gong XG, Wei SH. Wurtzite-derived polytypes of kesterite and stannite quaternary chalcogenide semiconductors. Phys Rev B - Condens Matter Mater Phys 2010;82:195203. https://doi.org/10.1103/PhysRevB.82.195203.
[66] Siebentritt S, Schorr S. Kesterites-a challenging material for solar cells. Prog Photovoltaics Res Appl 2012;20:512–9. https://doi.org/10.1002/pip.2156.
[67] Mortazavi Amiri NB, Postnikov A. Electronic structure and lattice dynamics in kesterite-type Cu2 ZnSnSe4 from first-principles calculations. Phys Rev B - Condens Matter Mater Phys 2010. https://doi.org/10.1103/PhysRevB.82.205204.
[68] Li YH, Walsh A, Chen S, Yin WJ, Yang JH, Li J, et al. Revised ab initio natural band offsets of all group IV, II-VI, and III-V semiconductors. Appl Phys Lett 2009. https://doi.org/10.1063/1.3143626.
[69] Scragg JJ, Dale PJ, Peter LM. Towards sustainable materials for solar energy conversion: preparation and photoelectrochemical characterization of Cu2ZnSnS4. Electrochem Commun 2008. https://doi.org/10.1016/j.elecom.2008.02.008.
[70] Rincón C, Márquez R. Defect physics of the CuInSe2 chalcopyrite semiconductor. J Phys Chem Solids 1999. https://doi.org/10.1016/S0022-3697(99)00190-0.
[71] Chen S, Walsh A, Yang JH, Gong XG, Sun L, Yang PX, et al. Compositional dependence of structural and electronic properties of Cu 2ZnSn(S,Se)4 alloys for thin film solar cells. Phys Rev B - Condens Matter Mater Phys 2011;83. https://doi.org/10.1103/PhysRevB.83.125201.
[72] Ito K, Nakazawa T. Electrical and optical properties of stannite-type quaternary semiconductor thin films. Jpn J Appl Phys 1988. https://doi.org/10.1143/JJAP.27.2094.
[73] Katagiri H. Cu2ZnSnS4 thin film solar cells. Thin Solid Films 2005. https://doi.org/10.1016/j.tsf.2004.11.024.
[74] Wu X, Liu W, Cheng S, Lai Y, Jia H. Photoelectric properties of Cu 2ZnSnS 4 thin films deposited by thermal evaporation. J Semicond 2012. https://doi.org/10.1088/1674-4926/33/2/022002.
[75] Chen S, Yang JH, Gong XG, Walsh A, Wei SH. Intrinsic point defects and complexes in the quaternary kesterite semiconductor Cu2 ZnSnS4. Phys Rev B - Condens Matter Mater Phys 2010;81:245204. https://doi.org/10.1103/PhysRevB.81.245204.
[76] Seol JS, Lee SY, Lee JC, Nam HD, Kim KH. Electrical and optical properties of Cu2ZnSnS4 thin films prepared by rf

magnetron sputtering process. Sol Energy Mater Sol Cells 2003. https://doi.org/10.1016/S0927-0248(02)00127-7.
[77] Khare A, Wills AW, Ammerman LM, Norris DJ, Aydil ES. Size control and quantum confinement in Cu2ZnSnS4 nanocrystals. Chem Commun 2011;47:11721–3. https://doi.org/10.1039/c1cc14687d.
[78] Shi L, Pei C, Xu Y, Li Q. Template-directed synthesis of ordered single-crystalline nanowires arrays of Cu2ZnSnS4 and Cu2ZnSnSe4. J Am Chem Soc 2011. https://doi.org/10.1021/ja201740w.
[79] Lu X, Zhuang Z, Peng Q, Li Y. Wurtzite Cu2ZnSnS4 nanocrystals: a novel quaternary semiconductor. Chem Commun 2011;47:3141–3. https://doi.org/10.1039/c0cc05064d.
[80] Platzer-Björkman C. Kesterite compound semiconductors for thin film solar cells. Curr Opin Green Sustain Chem 2017;4:84–90. https://doi.org/10.1016/j.cogsc.2017.02.010.
[81] Liu X, Feng Y, Cui H, Liu F, Hao X, Conibeer G, et al. The current status and future prospects of kesterite solar cells: a brief review. Prog Photovoltaics Res Appl 2016;24:879–98. https://doi.org/10.1002/pip.2741.
[82] Kim J, Larina L, Chung SY, Shin D, Shin B. Atomistic consideration of earth-abundant chalcogenide materials for photovoltaics: kesterite and beyond. J Mater Res 2018;33:3986–98. https://doi.org/10.1557/jmr.2018.350.
[83] Polizzotti A, Repins IL, Noufi R, Wei SH, Mitzi DB. The state and future prospects of kesterite photovoltaics. Energy Environ Sci 2013. https://doi.org/10.1039/c3ee41781f.
[84] Delbos S. Kësterite thin films for photovoltaics: a review. EPJ Photovoltaics 2012;3:35004. https://doi.org/10.1051/epjpv/2012008.
[85] Giraldo S, Placidi M, Saucedo E. Kesterite: new progress toward earth-abundant thin-film photovoltaic. Adv. Micro-Nanomater. Photovoltaics 2019:93–120. https://doi.org/10.1016/B978-0-12-814501-2.00005-0. Elsevier.
[86] Dhawale DS, Ali A, Lokhande AC. Impact of various dopant elements on the properties of kesterite compounds for solar cell applications: a status review. Sustain Energy Fuels 2019;3:1365–83. https://doi.org/10.1039/c9se00040b.
[87] Chen S, Walsh A, Gong XG, Wei SH. Classification of lattice defects in the kesterite Cu2ZnSnS 4 and Cu2ZnSnSe4 earth-abundant solar cell absorbers. Adv Mater 2013;25:1522–39. https://doi.org/10.1002/adma.201203146.
[88] Kattan N, Hou B, Fermín DJ, Cherns D. Crystal structure and defects visualization of Cu2ZnSnS4 nanoparticles employing transmission electron microscopy and electron diffraction. Appl Mater Today 2015;1:52–9. https://doi.org/10.1016/j.apmt.2015.08.004.
[89] Chen S, Gong XG, Walsh A, Wei SH. Defect physics of the kesterite thin-film solar cell absorber Cu 2 ZnSnS4. Appl Phys Lett 2010;96:021902. https://doi.org/10.1063/1.3275796.
[90] Chen S, Gong XG, Walsh A, Wei SH. Crystal and electronic band structure of Cu2 ZnSn X4 (X=S and Se) photovoltaic absorbers: first-principles insights. Appl Phys Lett 2009. https://doi.org/10.1063/1.3074499.
[91] Valle Rios LE, Neldner K, Gurieva G, Schorr S. Existence of off-stoichiometric single phase kesterite. J Alloys Compd 2016;657:408–13. https://doi.org/10.1016/j.jallcom.2015.09.198.
[92] Yang KJ, Sim JH, Son DH, Jeon DH, Hwang DK, Nam D, et al. Comparison of chalcopyrite and kesterite thin-film solar cells. J Ind Eng Chem 2017;45:78–84. https://doi.org/10.1016/j.jiec.2016.09.005.
[93] Abermann S. Non-vacuum processed next generation thin film photovoltaics: towards marketable efficiency and production of CZTS based solar cells. Sol Energy 2013;94:37–70. https://doi.org/10.1016/j.solener.2013.04.017.
[94] Wallace SK, Mitzi DB, Walsh A. The steady rise of kesterite solar cells. ACS Energy Lett 2017;2:776–9. https://doi.org/10.1021/acsenergylett.7b00131.
[95] Kaur K, Kumar N, Kumar M. Strategic review of interface carrier recombination in earth abundant Cu-Zn-Sn-S-Se solar cells: current challenges and future prospects. J Mater Chem A 2017;5:3069–90. https://doi.org/10.1039/C6TA10543B.
[96] Just J, Sutter-Fella CM, Lützenkirchen-Hecht D, Frahm R, Schorr S, Unold T. Secondary phases and their influence on the composition of the kesterite phase in CZTS and CZTSe thin films. Phys Chem Chem Phys 2016;18:15988–94. https://doi.org/10.1039/c6cp00178e.
[97] Zhou B, Xia D, Wang Y. Phase-selective synthesis and formation mechanism of CZTS nanocrystals. RSC Adv 2015;5:70117–26. https://doi.org/10.1039/c5ra11890e.
[98] Prabhakar T, Jampana N. Effect of sodium diffusion on the structural and electrical properties of Cu2ZnSnS4 thin films. Sol Energy Mater Sol Cells 2011;95:1001–4. https://doi.org/10.1016/j.solmat.2010.12.012.
[99] González JC, Fernandes PA, Ribeiro GM, Abelenda A, Viana ER, Salomé PMP, et al. Influence of the sulphurization time on the morphological, chemical, structural and electrical properties of Cu2ZnSnS4 polycrystalline thin films. Sol Energy Mater Sol Cells 2014;123:58–64. https://doi.org/10.1016/j.solmat.2014.01.005.
[100] Lee SG, Kim J, Woo HS, Jo Y, Inamdar AI, Pawar SM, et al. Structural, morphological, compositional, and optical properties of single step electrodeposited Cu 2 ZnSnS 4 (CZTS) thin films for solar cell application. Curr Appl Phys 2014;14:254–8. https://doi.org/10.1016/j.cap.2013.11.028.
[101] Kumar M, Dubey A, Adhikari N, Venkatesan S, Qiao Q. Strategic review of secondary phases, defects and defect-complexes in kesterite CZTS-Se solar cells. Energy Environ Sci 2015;8:3134–59. https://doi.org/10.1039/c5ee02153g.
[102] Kermadi S, Sali S, Zougar L, Boumaour M, Gunder R, Schorr S, et al. An in-depth investigation on the grain growth and the formation of secondary phases of ultrasonic-sprayed Cu 2 ZnSnS 4 based thin films assisted by Na crystallization catalyst. Sol Energy 2018;176:277–86. https://doi.org/10.1016/j.solener.2018.10.045.
[103] Hong CW, Shin SW, Suryawanshi MP, Gang MG, Heo J, Kim JH. Chemically deposited CdS buffer/kesterite Cu2ZnSnS4 solar cells: relationship between CdS thickness and device performance. ACS Appl Mater Interfaces 2017;9:36733–44. https://doi.org/10.1021/acsami.7b09266.
[104] Li J, Wang D, Li X, Zeng Y, Zhang Y. Cation substitution in earth-abundant kesterite photovoltaic materials. Adv Sci 2018. https://doi.org/10.1002/advs.201700744.
[105] Romanyuk YE, Haass SG, Giraldo S, Placidi M, Tiwari D, Fermin DJ, et al. Doping and alloying of kesterites. J Phys Energy 2019;1:044004. https://doi.org/10.1088/2515-7655/ab23bc.
[106] Nagai T, Shimamura T, Tanigawa K, Iwamoto Y, Hamada H, Ohta N, et al. Band Alignment of the CdS/Cu 2 Zn(Sn 1-x Ge x)Se 4 heterointerface and electronic properties at the Cu 2 Zn(Sn 1-x Ge x)Se 4 surface: X = 0, 0.2, and 0.4. ACS Appl Mater Interfaces 2019;11:4637–48. https://doi.org/10.1021/acsami.8b19200.
[107] Chen S, Gong XG, Walsh A, Wei SH. Defect physics of the kesterite thin-film solar cell absorber Cu 2 ZnSnS4. Appl Phys Lett 2010. https://doi.org/10.1063/1.3275796.
[108] Vigil-Galán O, Espíndola-Rodríguez M, Courel M, Fontané X, Sylla D, Izquierdo-Roca V, et al. Secondary phases

dependence on composition ratio in sprayed Cu 2ZnSnS4 thin films and its impact on the high power conversion efficiency. Sol Energy Mater Sol Cells 2013. https://doi.org/10.1016/j.solmat.2013.06.008.
[109] Redinger A, Hönes K, Fontań X, Izquierdo-Roca V, Saucedo E, Valle N, et al. Detection of a ZnSe secondary phase in coevaporated Cu2 ZnSnSe4 thin films. Appl Phys Lett 2011. https://doi.org/10.1063/1.3558706.
[110] Wang K, Shin B, Reuter KB, Todorov T, Mitzi DB, Guha S. Structural and elemental characterization of high efficiency Cu2 ZnSnS4 solar cells. Appl Phys Lett 2011. https://doi.org/10.1063/1.3543621.
[111] Wagner R, Wiemhöfer HD. Hall effect and conductivity in thin films of low temperature chalcocite Cu2S at 20°C as a function of stoichiometry. J Phys Chem Solids 1983. https://doi.org/10.1016/0022-3697(83)90013-6.
[112] Nozaki H, Shibata K, Ohhashi N. Metallic hole conduction in CuS. J Solid State Chem 1991. https://doi.org/10.1016/0022-4596(91)90085-V.
[113] Liang W, Whangbo MH. Conductivity anisotropy and structural phase transition in Covellite CuS. Solid State Commun 1993. https://doi.org/10.1016/0038-1098(93)90689-K.
[114] Ogah OE, Zoppi G, Forbes I, Miles RW. Thin films of tin sulphide for use in thin film solar cell devices. Thin Solid Films 2009. https://doi.org/10.1016/j.tsf.2008.11.023.
[115] Thangaraju B, Kaliannan P. Spray pyrolytic deposition and characterization of SnS and SnS2 thin films. J Phys D Appl Phys 2000. https://doi.org/10.1088/0022-3727/33/9/304.
[116] Calixto-Rodriguez M, Martinez H, Sanchez-Juarez A, Campos-Alvarez J, Tiburcio-Silver A, Calixto ME. Structural, optical, and electrical properties of tin sulfide thin films grown by spray pyrolysis. Thin Solid Films 2009. https://doi.org/10.1016/j.tsf.2008.11.026.
[117] Deshpande NG, Sagade AA, Gudage YG, Lokhande CD, Sharma R. Growth and characterization of tin disulfide (SnS2) thin film deposited by successive ionic layer adsorption and reaction (SILAR) technique. J Alloys Compd 2007. https://doi.org/10.1016/j.jallcom.2006.12.108.
[118] Hu X, Song G, Li W, Peng Y, Jiang L, Xue Y, et al. Phase-controlled synthesis and photocatalytic properties of SnS, SnS 2 and SnS/SnS2 heterostructure nanocrystals. Mater Res Bull 2013;48:2325–32. https://doi.org/10.1016/j.materresbull.2013.02.082.
[119] Avellaneda D, Nair MTS, Nair PK. Photovoltaic structures using chemically deposited tin sulfide thin films. Thin Solid Films 2009. https://doi.org/10.1016/j.tsf.2008.11.043.
[120] Tiwari D, Chaudhuri TK, Shripathi T, Deshpande U, Rawat R. Non-toxic, earth-abundant 2% efficient Cu2SnS3 solar cell based on tetragonal films direct-coated from single metal-organic precursor solution. Sol Energy Mater Sol Cells 2013. https://doi.org/10.1016/j.solmat.2013.02.017.
[121] Wu C, Hu Z, Wang C, Sheng H, Yang J, Xie Y. Hexagonal Cu2 Sn S3 with metallic character: another category of conducting sulfides. Appl Phys Lett 2007;91:143104. https://doi.org/10.1063/1.2790491.
[122] Berg DM, Djemour R, Gütay L, Siebentritt S, Dale PJ, Fontane X, et al. Raman analysis of monoclinic Cu 2SnS 3 thin films. Appl Phys Lett 2012. https://doi.org/10.1063/1.4712623.
[123] Chino K, Koike J, Eguchi S, Araki H, Nakamura R, Jimbo K, et al. Preparation of Cu 2SnS 3 thin films by sulfurization of Cu/Sn stacked precursors. Jpn J Appl Phys 2012;51:10NC35. https://doi.org/10.1143/JJAP.51.10NC35.
[124] Baranowski LL, Zawadzki P, Christensen S, Nordlund D, Lany S, Tamboli AC, et al. Control of doping in Cu2SnS3 through defects and alloying. Chem Mater 2014. https://doi.org/10.1021/cm501339v.
[125] Shin SW, Pawar SM, Park CY, Yun JH, Moon JH, Kim JH, et al. Studies on Cu2ZnSnS4 (CZTS) absorber layer using different stacking orders in precursor thin films. Sol Energy Mater Sol Cells 2011. https://doi.org/10.1016/j.solmat.2011.07.005.
[126] Fernandes PA, Salomé PMP, Da Cunha AF. Study of polycrystalline Cu2ZnSnS4 films by Raman scattering. J Alloys Compd 2011. https://doi.org/10.1016/j.jallcom.2011.04.097.
[127] Fernandes PA, Salomé PMP, da Cunha AF. Growth and Raman scattering characterization of Cu2ZnSnS4 thin films. Thin Solid Films 2009. https://doi.org/10.1016/j.tsf.2008.11.031.
[128] Berg DM, Arasimowicz M, Djemour R, Gütay L, Siebentritt S, Schorr S, et al. Discrimination and detection limits of secondary phases in Cu2ZnSnS4 using X-ray diffraction and Raman spectroscopy. Thin Solid Films 2014. https://doi.org/10.1016/j.tsf.2014.08.028.
[129] Fontań X, Calvo-Barrio L, Izquierdo-Roca V, Saucedo E, Ṕrez-Rodriguez A, Morante JR, et al. In-depth resolved Raman scattering analysis for the identification of secondary phases: characterization of Cu2 ZnSnS4 layers for solar cell applications. Appl Phys Lett 2011. https://doi.org/10.1063/1.3587614.
[130] Dimitrievska M, Fairbrother A, Fontané X, Jawhari T, Izquierdo-Roca V, Saucedo E, et al. Multiwavelength excitation Raman scattering study of polycrystalline kesterite Cu2ZnSnS4 thin films. Appl Phys Lett 2014. https://doi.org/10.1063/1.4861593.
[131] Just J, Ltzenkirchen-Hecht D, Frahm R, Schorr S, Unold T. Determination of secondary phases in kesterite Cu 2ZnSnS 4 thin films by x-ray absorption near edge structure analysis. Appl Phys Lett 2011;99:2011–4. https://doi.org/10.1063/1.3671994.
[132] Nilsen WG. Raman spectrum of cubic ZnS. Phys Rev 1969. https://doi.org/10.1103/PhysRev.182.838.
[133] Verma S kant, Agrawal V, Jain K, Pasricha R, Chand S. Green synthesis of nanocrystalline Cu 2 ZnSnS 4 powder using hydrothermal route. J Nanoparticles 2013;2013:1–7. https://doi.org/10.1155/2013/685836.
[134] Tiong VT, Zhang Y, Bell J, Wang H. Phase-selective hydrothermal synthesis of Cu2ZnSnS4 nanocrystals: the effect of the sulphur precursor. CrystEngComm 2014;16:4306–13. https://doi.org/10.1039/c3ce42606h.
[135] Shi Z, Jayatissa AH. One-pot hydrothermal synthesis and fabrication of kesterite Cu2ZnSn(S,Se)4thin films. Prog Nat Sci Mater Int 2017;27:550–5. https://doi.org/10.1016/j.pnsc.2017.09.006.
[136] Das S, Sa K, Alam I, Mahakul PC, Raiguru J, Subramanyam BVRS, et al. Synthesis and characterizations of Cu 2 ZnSnS 4 nanoparticles/carbon nanotube composite as an efficient absorber material for solar cell application. AIP Conf. Proc. 2018;1961. https://doi.org/10.1063/1.5035199.
[137] Vanalakar SA, Agwane GL, Gang MG, Patil PS, Kim JYH, Kim JYH. A mild hydrothermal route to synthesis of CZTS nanoparticle inks for solar cell applications. Phys Status Solidi Curr Top Solid State Phys 2015;12:500–3. https://doi.org/10.1002/pssc.201400261.
[138] Yan X, Michael E, Komarneni S, Brownson JR, Yan ZF. Microwave-hydrothermal/solvothermal synthesis of kesterite, an emerging photovoltaic material. Ceram Int 2014;40:1985–92. https://doi.org/10.1016/j.ceramint.2013.07.108.
[139] Phaltane SA, Vanalakar SA, Bhat TS, Patil PS, Sartale SD, Kadam LD. Photocatalytic degradation of methylene blue by hydrothermally synthesized CZTS nanoparticles. J Mater Sci Mater Electron 2017;28:8186–91. https://doi.org/10.1007/s10854-017-6527-0.

[140] Martini T, Chubilleau C, Poncelet O, Ricaud A, Blayo A, Martin C, et al. Spray and inkjet fabrication of Cu2ZnSnS4 thin films using nanoparticles derived from a continuous-flow microwave-assisted synthesis. Sol Energy Mater Sol Cells 2016;144:657–63. https://doi.org/10.1016/j.solmat.2015.09.046.
[141] Cao M, Shen Y. A mild solvothermal route to kesterite quaternary Cu2ZnSnS 4 nanoparticles. J Cryst Growth 2011;318:1117–20. https://doi.org/10.1016/j.jcrysgro.2010.10.071. North-Holland.
[142] Kannan AG, Manjulavalli TE, Chandrasekaran J. Influence of solvent on the properties of CZTS nanoparticles. Procedia Eng 2016;141:15–22. https://doi.org/10.1016/j.proeng.2015.08.1112.
[143] Zou Z, Gao Y, Long F, Wang J, Zhang J. One-pot solvothermal synthesis of wurtzite Cu_2ZnSnS_4 nanocrystals. Mater Lett 2015;158:13–6. https://doi.org/10.1016/j.matlet.2015.05.063.
[144] Patro B, Vijaylakshmi S, Reddy RK, Sharma P. Microwave-assisted solvothermal synthesis of Cu2ZnSnS4 (CZTS) nanocrystals for photovoltaic applications. Mater Today Proc 2016;3:2786–94. https://doi.org/10.1016/j.matpr.2016.06.028. Elsevier Ltd.
[145] Mali SS, Kim H, Shim CS, Patil PS, Hong CK. Polyvinylpyrrolidone (PVP) assisted single-step synthesis of kesterite Cu2ZnSnS4 nanoparticles by solvothermal process. Phys Status Solidi - Rapid Res Lett 2013;7:1050–4. https://doi.org/10.1002/pssr.201308132.
[146] Riha SC, Parkinson BA, Prieto AL. Solution-based synthesis and characterization of Cu2ZnSnS 4 nanocrystals. J Am Chem Soc 2009;131:12054–5. https://doi.org/10.1021/ja9044168.
[147] Jain S, Singh D, Vijayan N, Sharma SN. Time-controlled synthesis mechanism analysis of kesterite-phased Cu 2 ZnSnS 4 nanorods via colloidal route. Appl Nanosci 2018;8:435–46. https://doi.org/10.1007/s13204-018-0781-1.
[148] Lin X, Kavalakkatt J, Kornhuber K, Abou-Ras D, Schorr S, Lux-Steiner MC, et al. Synthesis of Cu 2Zn xSn ySe 1+x+2y nanocrystals with wurtzite-derived structure. RSC Adv 2012;2:9894–8. https://doi.org/10.1039/c2ra21293e.
[149] Agarwal G, Tripathi B. Low cost hot injection synthesis of wurtzite Cu2ZnSnS4 nanocrystals. Mater Today Proc 2020. https://doi.org/10.1016/j.matpr.2020.07.369.
[150] Gong Z, Han Q, Li J, Hou L, Bukhtiar A, Yang S, et al. A solvothermal route to synthesize kesterite Cu2ZnSnS4 nanocrystals for solution-processed solar cells. J Alloys Compd 2016;663:617–23. https://doi.org/10.1016/j.jallcom.2015.12.181.
[151] Lin YH, Das S, Yang CY, Sung JC, Lu CH. Phase-controlled synthesis of Cu2ZnSnS4 powders via the microwave-assisted solvothermal route. J Alloys Compd 2015;632:354–60. https://doi.org/10.1016/j.jallcom.2015.01.254.
[152] Riha SC, Fredrick SJ, Sambur JB, Liu Y, Prieto AL, Parkinson BA. Photoelectrochemical characterization of nanocrystalline thin-film Cu 2ZnSnS4 photocathodes. ACS Appl Mater Interfaces 2011;3:58–66. https://doi.org/10.1021/am1008584.
[153] Riha SC, Parkinson BA, Prieto AL. Compositionally tunable Cu2ZnSn(S1-xSe x)4 nanocrystals: probing the effect of Se-inclusion in mixed chalcogenide thin films. J Am Chem Soc 2011;133:15272–5. https://doi.org/10.1021/ja2058692.
[154] Wei M, Du Q, Wang D, Liu W, Jiang G, Zhu C. Synthesis of spindle-like kesterite Cu 2ZnSnS 4 nanoparticles using thiorea as sulfur source. Mater Lett 2012;79:177–9. https://doi.org/10.1016/j.matlet.2012.03.080.
[155] Dale PJ, Hoenes K, Scragg J, Siebentritt S. A review of the challenges facing kesterite based thin film solar cells. In: Conf Rec IEEE Photovolt Spec Conf; 2009. p. 2080–5. https://doi.org/10.1109/PVSC.2009.5411441.
[156] Repins I, Vora N, Beall C, Wei SH, Yan F, Romero M, et al. Kesterites and chalcopyrites: a comparison of close cousins. Mater Res Soc Symp Proc 2012;1324:97–108. https://doi.org/10.1557/opl.2011.844.
[157] Mitzi DB, Gunawan O, Todorov TK, Wang K, Guha S. The path towards a high-performance solution-processed kesterite solar cell. Sol Energy Mater Sol Cells 2011;95:1421–36. https://doi.org/10.1016/j.solmat.2010.11.028.
[158] Rakitin VV, Novikov GF. Third-generation solar cells based on quaternary copper compounds with the kesterite-type structure. Russ Chem Rev 2017;86:99–112. https://doi.org/10.1070/rcr4633.
[159] Li Z, Ho JCW, Lee KK, Zeng X, Zhang T, Wong LH, et al. Environmentally friendly solution route to kesterite Cu2ZnSn(S, Se)4 thin films for solar cell applications. RSC Adv 2014;4:26888–94. https://doi.org/10.1039/c4ra03349c.
[160] Dalapati GK, Zhuk S, Masudy-Panah S, Kushwaha A, Seng HL, Chellappan V, et al. Impact of molybdenum out diffusion and interface quality on the performance of sputter grown CZTS based solar cells. Sci Rep 2017;7. https://doi.org/10.1038/s41598-017-01605-7.
[161] Romanyuk YE, Fella CM, Uhl AR, Werner M, Tiwari AN, Schnabel T, et al. Recent trends in direct solution coating of kesterite absorber layers in solar cells. Sol Energy Mater Sol Cells 2013;119:181–9. https://doi.org/10.1016/j.solmat.2013.06.038.
[162] Weber A, Mainz R, Schock HW. On the Sn loss from thin films of the material system Cu-Zn-Sn-S in high vacuum. J Appl Phys 2010. https://doi.org/10.1063/1.3273495.
[163] Mitzi DB, Gunawan O, Todorov TK, Wang K, Guha S. The path towards a high-performance solution-processed kesterite solar cell. Sol Energy Mater Sol Cells 2011. https://doi.org/10.1016/j.solmat.2010.11.028.
[164] Green MA, Hishikawa Y, Dunlop ED, Levi DH, Hohl-Ebinger J, Yoshita M, et al. Solar cell efficiency tables (Version 53). Prog Photovoltaics Res Appl 2019. https://doi.org/10.1002/pip.3102.
[165] Kemell M, Ritala M, Leskelä M. Thin film deposition methods for CuInSe2 solar cells. Crit Rev Solid State Mater Sci 2005. https://doi.org/10.1080/10408430590918341.
[166] Katagiri H, Saitoh K, Washio T, Shinohara H, Kurumadani T, Miyajima S. Development of thin film solar cell based on Cu2ZnSnS4 thin films. Sol Energy Mater Sol Cells 2001;65:141–8. https://doi.org/10.1016/S0927-0248(00)00088-X.
[167] Schubert BA, Marsen B, Cinque S, Unold T, Klenk R, Schorr S, et al. Cu2ZnSnS4 thin film solar cells by fast coevaporation. Prog Photovoltaics Res Appl 2011. https://doi.org/10.1002/pip.976.
[168] Shin B, Gunawan O, Zhu Y, Bojarczuk NA, Chey SJ, Guha S. Thin film solar cell with 8.4% power conversion efficiency using an earth-abundant Cu2ZnSnS4 absorber. Prog Photovoltaics Res Appl 2013. https://doi.org/10.1002/pip.1174.
[169] Guo H, Ma C, Zhang K, Jia X, Li Y, Yuan N, et al. The fabrication of Cd-free Cu2ZnSnS4-Ag2ZnSnS4 heterojunction photovoltaic devices. Sol Energy Mater Sol Cells 2018;178:146–53. https://doi.org/10.1016/j.solmat.2018.01.022.
[170] Yan C, Huang J, Sun K, Johnston S, Zhang Y, Sun H, et al. Cu2ZnSnS4 solar cells with over 10% power conversion efficiency enabled by heterojunction heat treatment. Nat Energy 2018;3:764–72. https://doi.org/10.1038/s41560-018-0206-0.

[171] Giraldo S, Saucedo E, Neuschitzer M, Oliva F, Placidi M, Alcobé X, et al. How small amounts of Ge modify the formation pathways and crystallization of kesterites. Energy Environ Sci 2018;11:582–93. https://doi.org/10.1039/c7ee02318a.
[172] Fairbrother A, Fontané X, Izquierdo-Roca V, Espindola-Rodriguez M, Lõpez-Marino S, Placidi M, et al. Single-step sulfo-selenization method to synthesize Cu 2ZnSn(SySe1-y) 4 absorbers from metallic stack precursors. ChemPhysChem 2013. https://doi.org/10.1002/cphc.201300157.
[173] Zhang J, Shao L, Fu Y, Xie E. Cu2ZnSnS4 thin films prepared by sulfurization of ion beam sputtered precursor and their electrical and optical properties. Rare Met 2006;25:315–9. https://doi.org/10.1016/S1001-0521(07)60096-5.
[174] Yoo H, Kim J. Comparative study of Cu2ZnSnS4 film growth. Sol Energy Mater Sol Cells 2011. https://doi.org/10.1016/j.solmat.2010.04.060.
[175] Jimbo K, Kimura R, Kamimura T, Yamada S, Maw WS, Araki H, et al. Cu2ZnSnS4-type thin film solar cells using abundant materials. Thin Solid Films 2007. https://doi.org/10.1016/j.tsf.2006.12.103.
[176] Katagiri H, Jimbo K, Yamada S, Kamimura T, Maw WS, Fukano T, et al. Enhanced conversion efficiencies of Cu2ZnSnS4-based thin film solar cells by using preferential etching technique. Appl Phys Express 2008. https://doi.org/10.1143/APEX.1.041201.
[177] Moriya K, Tanaka K, Uchiki H. Fabrication of Cu2ZnSnS4 thin-film solar cell prepared by pulsed laser deposition. Jpn J Appl Phys Part 1 Regul Pap Short Notes Rev Pap 2007. https://doi.org/10.1143/JJAP.46.5780.
[178] Gansukh M, López Mariño S, Espindola Rodriguez M, Engberg SLJ, Martinho FMA, Hajijafarassar A, et al. Oxide route for production of Cu2ZnSnS4 solar cells by pulsed laser deposition. Sol Energy Mater Sol Cells 2020. https://doi.org/10.1016/j.solmat.2020.110605.
[179] Cazzaniga A, Crovetto A, Yan C, Sun K, Hao X, Ramis Estelrich J, et al. Ultra-thin Cu2ZnSnS4 solar cell by pulsed laser deposition. Sol Energy Mater Sol Cells 2017. https://doi.org/10.1016/j.solmat.2017.03.002.
[180] Schou J, Gansukh M, Ettlinger RB, Cazzaniga A, Grossberg M, Kauk-Kuusik M, et al. Pulsed laser deposition of chalcogenide sulfides from multi- and single-component targets: the non-stoichiometric material transfer. Appl Phys A Mater Sci Process 2018. https://doi.org/10.1007/s00339-017-1475-3.
[181] Wang W, Winkler MT, Gunawan O, Gokmen T, Todorov TK, Zhu Y, et al. Device characteristics of CZTSSe thin-film solar cells with 12.6% efficiency. Adv Energy Mater 2014. https://doi.org/10.1002/aenm.201301465.
[182] Su Z, Sun K, Han Z, Cui H, Liu F, Lai Y, et al. Fabrication of Cu2ZnSnS4 solar cells with 5.1% efficiency via thermal decomposition and reaction using a non-toxic sol-gel route. J Mater Chem A 2014. https://doi.org/10.1039/c3ta13533k.
[183] Tanaka K, Moritake N, Uchiki H. Preparation of Cu2 ZnSnS4 thin films by sulfurizing sol-gel deposited precursors. Sol Energy Mater Sol Cells 2007. https://doi.org/10.1016/j.solmat.2007.04.012.
[184] Sun K, Yan C, Liu F, Hao X. Towards 9% sulfide CZTS solar cells fabricated by a sol-gel process. In: 2018 IEEE 7th world Conf. Photovolt. Energy conversion, WCPEC 2018 - a Jt. Conf. 45th IEEE PVSC, 28th PVSEC 34th EU PVSEC; 2018. https://doi.org/10.1109/PVSC.2018.8548131.
[185] Liu F, Shen S, Zhou F, Song N, Wen X, Stride JA, et al. Kesterite Cu2ZnSnS4 thin film solar cells by a facile DMF-based solution coating process. J Mater Chem C 2015. https://doi.org/10.1039/c5tc01750e.
[186] Xin H, Katahara JK, Braly IL, Hillhouse HW. 8% Efficient Cu2ZnSn(S,Se)4 solar cells from redox equilibrated simple precursors in DMSO. Adv Energy Mater 2014;4:1–5. https://doi.org/10.1002/aenm.201301823.
[187] Ki W, Hillhouse HW. Earth-abundant element photovoltaics directly from soluble precursors with high yield using a non-toxic solvent. Adv Energy Mater 2011;1:732–5. https://doi.org/10.1002/aenm.201100140.
[188] Xin H, Vorpahl SM, Collord AD, Braly IL, Uhl AR, Krueger BW, et al. Lithium-doping inverts the nanoscale electric field at the grain boundaries in Cu2ZnSn(S,Se)4 and increases photovoltaic efficiency. Phys Chem Chem Phys 2015. https://doi.org/10.1039/c5cp04707b.
[189] Haass SG, Diethelm M, Werner M, Bissig B, Romanyuk YE, Tiwari AN. 11.2% efficient solution processed kesterite solar cell with a low voltage deficit. Adv Energy Mater 2015. https://doi.org/10.1002/aenm.201500712.
[190] Schnabel T, Abzieher T, Friedlmeier TM, Ahlswede E. Solution-based preparation of Cu2ZnSn(S,Se)4 for solar cells - comparison of SnSe2 and elemental Se as chalcogen source. IEEE J Photovolt 2015. https://doi.org/10.1109/JPHOTOV.2015.2392935.
[191] Collord AD, Hillhouse HW. Germanium alloyed kesterite solar cells with low voltage deficits. Chem Mater 2016. https://doi.org/10.1021/acs.chemmater.5b04806.
[192] Yang WC, Miskin CK, Carter NJ, Agrawal R, Stach EA. Compositional inhomogeneity of multinary semiconductor nanoparticles: a case study of Cu2ZnSnS4. Chem Mater 2014. https://doi.org/10.1021/cm502930d.
[193] Aziz F, Ismail AF. Spray coating methods for polymer solar cells fabrication: a review. Mater Sci Semicond Process 2015. https://doi.org/10.1016/j.mssp.2015.05.019.
[194] Krebs FC. Fabrication and processing of polymer solar cells: a review of printing and coating techniques. Sol Energy Mater Sol Cells 2009. https://doi.org/10.1016/j.solmat.2008.10.004.
[195] Nakayama N, Ito K. Sprayed films of stannite Cu 2 ZnSnS 4. Appl Surf Sci 1996. https://doi.org/10.1016/0169-4332(95)00225-1.
[196] Courel M, Picquart M, Arce-Plaza A, Pulgarin-Agudelo FA, González-Castillo JR, Montoya De Los Santos I, et al. Study on the impact of stoichiometric and optimal compositional ratios on physical properties of Cu2ZnSnS4 thin films deposited by spray pyrolysis. Mater Res Express 2018. https://doi.org/10.1088/2053-1591/aaa720.
[197] Dermenji L, Curmei N, Guc M, Gurieva G, Rusu M, Fedorov V, et al. Effects of annealing on elemental composition and quality of CZTSSe thin films obtained by spray pyrolysis. Surf Eng Appl Electrochem 2016. https://doi.org/10.3103/S1068375516060041.
[198] Kim S, Kim J. Effect of selenization on sprayed Cu2ZnSnSe4 thin film solar cell. Thin Solid Films 2013. https://doi.org/10.1016/j.tsf.2013.03.094.
[199] Seboui Z, Cuminal Y, Kamoun-Turki N. Physical properties of Cu2ZnSnS4 thin films deposited by spray pyrolysis technique. J Renew Sustain Energy 2013. https://doi.org/10.1063/1.4795399.
[200] Courel M, Andrade-Arvizu JA, Guillén-Cervantes A, Nicolás-Marín MM, Pulgarín-Agudelo FA, Vigil-Galán O. Optimization of physical properties of spray-deposited Cu2ZnSnS4 thin films for solar cell applications. Mater Des 2017. https://doi.org/10.1016/j.matdes.2016.10.068.
[201] Perednis D, Gauckler LJ. Thin film deposition using spray pyrolysis. J Electroceram 2005. https://doi.org/10.1007/s10832-005-0870-x.
[202] Serin T, Serin N, Karadeniz S, Sari H, Tuğluoğlu N, Pakma O. Electrical, structural and optical properties of SnO2 thin

films prepared by spray pyrolysis. J Non Cryst Solids 2006. https://doi.org/10.1016/j.jnoncrysol.2005.11.031.
[203] Larramona G, Levcenko S, Bourdais S, Jacob A, Choné C, Delatouche B, et al. Fine-tuning the Sn content in CZTSSe thin films to achieve 10.8% solar cell efficiency from spray-deposited water-ethanol-based colloidal inks. Adv Energy Mater 2015. https://doi.org/10.1002/aenm.201501404.
[204] Collord AD, Xin H, Hillhouse HW. Combinatorial exploration of the effects of intrinsic and extrinsic defects in Cu2ZnSn(S,Se)4. IEEE J Photovolt 2015. https://doi.org/10.1109/JPHOTOV.2014.2361053.
[205] Colombara D, Crossay A, Vauche L, Jaime S, Arasimowicz M, Grand PP, et al. Electrodeposition of kesterite thin films for photovoltaic applications: quo vadis? Phys Status Solidi Appl Mater Sci 2015. https://doi.org/10.1002/pssa.201431364.
[206] Peter LM. Electrochemical routes to earth-abundant photovoltaics: a minireview. Electrochem Commun 2015. https://doi.org/10.1016/j.elecom.2014.11.012.
[207] Ahmed S, Reuter KB, Gunawan O, Guo L, Romankiw LT, Deligianni H. A high efficiency electrodeposited Cu 2ZnSnS 4 solar cell. Adv Energy Mater 2012. https://doi.org/10.1002/aenm.201100526.
[208] Lehner J, Ganchev M, Loorits M, Revathi N, Raadik T, Raudoja J, et al. Structural and compositional properties of CZTS thin films formed by rapid thermal annealing of electrodeposited layers. J Cryst Growth 2013. https://doi.org/10.1016/j.jcrysgro.2013.06.012.
[209] Araki H, Kubo Y, Jimbo K, Maw WS, Katagiri H, Yamazaki M, et al. Preparation of Cu2ZnSnS4 thin films by sulfurization of co-electroplated Cu-Zn-Sn precursors. Phys Status Solidi Curr Top Solid State Phys 2009. https://doi.org/10.1002/pssc.200881182.
[210] Yuan T, Li Y, Jia M, Lai Y, Li J, Liu F, et al. Fabrication of Cu2ZnSnS4 thin film solar cells by sulfurization of electrodeposited stacked binary Cu-Zn and Cu-Sn alloy layers. Mater Lett 2015. https://doi.org/10.1016/j.matlet.2015.04.101.
[211] Jiang F, Ikeda S, Tang Z, Minemoto T, Septina W, Harada T, et al. Impact of alloying duration of an electrodeposited Cu/Sn/Zn metallic stack on properties of Cu2ZnSnS4 absorbers for thin-film solar cells. Prog Photovoltaics Res Appl 2015. https://doi.org/10.1002/pip.2638.
[212] Jiang F, Ikeda S, Harada T, Matsumura M. Pure Sulfide Cu2ZnSnS4 thin film solar cells fabricated by preheating an electrodeposited metallic stack. Adv Energy Mater 2014. https://doi.org/10.1002/aenm.201301381.
[213] Dale PJ, Malaquias JC, Steichen M. Semiconductors for photovoltaic devices: electrochemical approaches using ionic liquids. ECS Trans 2014. https://doi.org/10.1149/05818.0001ecst.
[214] Steichen M, Malaquias JC, Arasimowicz M, Djemour R, Brooks NR, Van Meervelt L, et al. High-speed electrodeposition of copper-tin-zinc stacks from liquid metal salts for Cu2ZnSnSe4 solar cells. Chem Commun 2017. https://doi.org/10.1039/c6cc09225j.
[215] Clauwaert K, Binnemans K, Matthijs E, Fransaer J. Electrochemical studies of the electrodeposition of copper-zinc-tin alloys from pyrophosphate electrolytes followed by selenization for CZTSe photovoltaic cells. Electrochim Acta 2016. https://doi.org/10.1016/j.electacta.2015.12.013.
[216] Pawar BS, Pawar SM, Shin SW, Choi DS, Park CJ, Kolekar SS, et al. Effect of complexing agent on the properties of electrochemically deposited Cu 2 ZnSnS 4 (CZTS) thin films. Appl Surf Sci 2010. https://doi.org/10.1016/j.apsusc.2010.09.016.
[217] Khalil MI, Bernasconi R, Magagnin L. CZTS layers for solar cells by an electrodeposition-annealing route. Electrochim Acta 2014. https://doi.org/10.1016/j.electacta.2014.09.001.
[218] Perelstein G, Valdes M, Vazquez M. Different routes of fixed pH to electrodeposit Cu2ZnSnS4 for photovoltaic devices. Materialia 2019. https://doi.org/10.1016/j.mtla.2018.100187.
[219] Unveroglu B, Zangari G. Effect of cell configuration on the compositional homogeneity of electrodeposited Cu-Zn-Sn alloys and phase purity of the resulting Cu2ZnSnS4 absorber layers. Electrochim Acta 2017. https://doi.org/10.1016/j.electacta.2017.08.155.
[220] Ge J, Jiang J, Yang P, Peng C, Huang Z, Zuo S, et al. A 5.5% efficient co-electrodeposited ZnO/CdS/Cu2ZnSnS 4/Mo thin film solar cell. Sol Energy Mater Sol Cells 2014. https://doi.org/10.1016/j.solmat.2014.02.020.
[221] Ge J, Yan Y. Controllable multinary alloy electrodeposition for thin-film solar cell fabrication: a case study of kesterite Cu2ZnSnS4. IScience 2018. https://doi.org/10.1016/j.isci.2018.02.002.
[222] Todorov TK, Reuter KB, Mitzi DB. High-efficiency solar cell with earth-abundant liquid-processed absorber. Adv Mater 2010. https://doi.org/10.1002/adma.200904155.
[223] Romanyuk YE, Fella CM, Uhl AR, Werner M, Tiwari AN, Schnabel T, et al. Recent trends in direct solution coating of kesterite absorber layers in solar cells. Sol Energy Mater Sol Cells 2013. https://doi.org/10.1016/j.solmat.2013.06.038.
[224] Burgués-Ceballos I, Stella M, Lacharmoise P, Martínez-Ferrero E. Towards industrialization of polymer solar cells: material processing for upscaling. J Mater Chem A 2014. https://doi.org/10.1039/c4ta03780d.
[225] Panthani MG, Akhavan V, Goodfellow B, Schmidtke JP, Dunn L, Dodabalapur A, et al. Synthesis of CuInS2, CuInSe2, and Cu(In xGa1-x)Se2 (CIGS) nanocrystal "inks" for printable photovoltaics. J Am Chem Soc 2008. https://doi.org/10.1021/ja805845q.
[226] Hages CJ, Koeper MJ, Miskin CK, Brew KW, Agrawal R. Controlled grain growth for high performance nanoparticle-based kesterite solar cells. Chem Mater 2016. https://doi.org/10.1021/acs.chemmater.6b02733.
[227] MacDonald BI, Martucci A, Rubanov S, Watkins SE, Mulvaney P, Jasieniak JJ. Layer-by-layer assembly of sintered CdSe xTe 1-x nanocrystal solar cells. ACS Nano 2012. https://doi.org/10.1021/nn3009189.
[228] Harrison MT, Kershaw SV, Burt MG, Eychmüller A, Weller H, Rogach AL. Wet chemical synthesis and spectroscopic study of CdHgTe nanocrystals with strong near-infrared luminescence. Mater Sci Eng B Solid-State Mater Adv Technol 2000. https://doi.org/10.1016/S0921-5107(99)00254-8.
[229] Ferguson A, Dippo P, Kuciauskas D, Farshchi R, Bailey J, Zapalac G, et al. Optical spectroscopic probes of degradation and metastability in polycrystalline (Ag,Cu)(In,Ga)Se2 absorbers. In: 2018 IEEE 7th world Conf. Photovolt. Energy conversion, WCPEC 2018 - a Jt. Conf. 45th IEEE PVSC, 28th PVSEC 34th EU PVSEC; 2018. https://doi.org/10.1109/PVSC.2018.8548226.
[230] Kim K, Park JW, Yoo JS, Cho JS, Lee HD, Yun JH. Ag incorporation in low-temperature grown Cu(In,Ga)Se2 solar cells using Ag precursor layers. Sol Energy Mater Sol Cells 2016. https://doi.org/10.1016/j.solmat.2015.11.028.
[231] López-Marino S, Sánchez Y, Espíndola-Rodríguez M, Alcobé X, Xie H, Neuschitzer M, et al. Alkali doping strategies for flexible and light-weight Cu2ZnSnSe4 solar cells. J Mater Chem A 2016. https://doi.org/10.1039/c5ta09640e.
[232] Dermenji L, Guc M, Gurieva G, Dittrich T, Rappich J, Curmei N, et al. Thin films of (AgxCu1−x)2ZnSn(S,Se)4 (x = 0.05–0.20) prepared by spray pyrolysis. Thin Solid Films 2019;690. https://doi.org/10.1016/j.tsf.2019.137532.
[233] Li W, Liu X, Cui H, Huang S, Hao X. The role of Ag in (Ag,Cu)2ZnSnS4 thin film for solar cell application. J Alloys Compd

2015;625:277–83. https://doi.org/10.1016/j.jallcom.2014.11.136.
[234] Chagarov E, Sardashti K, Kummel AC, Lee YS, Haight R, Gershon TS. $Ag_2ZnSn(S,Se)_4$: a highly promising absorber for thin film photovoltaics. J Chem Phys 2016. https://doi.org/10.1063/1.4943270.
[235] Mangelis P, Aziz A, Da Silva I, Grau-Crespo R, Vaqueiro P, Powell AV. Understanding the origin of disorder in kesterite-type chalcogenides A2ZnBQ4 (A = Cu, Ag; B = Sn, Ge; Q = S, Se): the influence of inter-layer interactions. Phys Chem Chem Phys 2019. https://doi.org/10.1039/c9cp03630j.
[236] Wei K, Khabibullin AR, Stedman T, Woods LM, Nolas GS. Polaronic transport in Ag-based quaternary chalcogenides. J Appl Phys 2017. https://doi.org/10.1063/1.5001690.
[237] Yuan ZK, Chen S, Xiang H, Gong XG, Walsh A, Park JS, et al. Engineering solar cell absorbers by exploring the band Alignment and defect disparity: the case of Cu- and Ag-based kesterite compounds. Adv Funct Mater 2015;25:6733–43. https://doi.org/10.1002/adfm.201502272.
[238] Gershon T, Sardashti K, Gunawan O, Mankad R, Singh S, Lee YS, et al. Photovoltaic device with over 5% efficiency based on an n-type Ag2ZnSnSe4 absorber. Adv Energy Mater 2016;6:1601182. https://doi.org/10.1002/aenm.201601182.
[239] Saha U, Alam MK. Boosting the efficiency of single junction kesterite solar cell using Ag mixed Cu2ZnSnS4 active layer. RSC Adv 2018. https://doi.org/10.1039/c7ra12352c.
[240] Guchhait A, Su Z, Tay YF, Shukla S, Li W, Leow SW, et al. Enhancement of open-circuit voltage of solution-processed Cu2ZnSnS4 solar cells with 7.2% efficiency by incorporation of silver. ACS Energy Lett 2016;1:1256–61. https://doi.org/10.1021/acsenergylett.6b00509.
[241] Qi Y, Tian Q, Meng Y, Kou D, Zhou Z, Zhou W, et al. Elemental precursor solution processed (Cu 1-x Ag x) 2 ZnSn(S,Se) 4 photovoltaic devices with over 10% efficiency. ACS Appl Mater Interfaces 2017;9:21243–50. https://doi.org/10.1021/acsami.7b03944.
[242] Gershon T, Lee YS, Antunez P, Mankad R, Singh S, Bishop D, et al. Photovoltaic materials and devices based on the alloyed kesterite absorber (AgxCu1-x)2ZnSnSe4. Adv Energy Mater 2016;6:1–7. https://doi.org/10.1002/aenm.201502468.
[243] Maeda T, Kawabata A, Wada T. First-principles study on alkali-metal effect of Li, Na, and K in Cu2ZnSnS4 and Cu2ZnSnSe4. Phys Status Solidi Curr Top Solid State Phys 2015. https://doi.org/10.1002/pssc.201400345.
[244] Yang Y, Kang X, Huang L, Pan D. Tuning the band gap of Cu2ZnSn(S,Se)4 thin films via lithium alloying. ACS Appl Mater Interfaces 2016;8:5308–13. https://doi.org/10.1021/acsami.5b11535.
[245] Cabas-Vidani A, Haass SG, Andres C, Caballero R, Figi R, Schreiner C, et al. High-efficiency (LixCu1−x)2ZnSn(S,Se)4 kesterite solar cells with lithium alloying. Adv Energy Mater 2018. https://doi.org/10.1002/aenm.201801191.
[246] Cabas-Vidani A, Haass SG, Andres C, Caballero R, Figi R, Schreiner C, et al. High-efficiency (LixCu1−x)2ZnSn(S,Se)4 kesterite solar cells with lithium alloying. Adv Energy Mater 2018;8:1–8. https://doi.org/10.1002/aenm.201801191.
[247] Yan C, Sun KKK, Huang J, Johnston S, Liu F, Veettil BP, et al. Beyond 11% efficient sulfide kesterite Cu 2 Zn x Cd 1-x SnS 4 solar cell: effects of cadmium alloying. ACS Energy Lett 2017;2:930–6. https://doi.org/10.1021/acsenergylett.7b00129.
[248] Su Z, Tan JMR, Li X, Zeng X, Batabyal SK, Wong LH. Cation substitution of solution-processed Cu2ZnSnS4 thin film solar cell with over 9% efficiency. Adv Energy Mater 2015. https://doi.org/10.1002/aenm.201500682.
[249] Sun R, Zhuang D, Zhao M, Gong Q, Scarpulla M, Wei Y, et al. Beyond 11% efficient Cu2ZnSn(Se,S)4 thin film solar cells by cadmium alloying. Sol Energy Mater Sol Cells 2018;174:494–8. https://doi.org/10.1016/j.solmat.2017.09.043.
[250] Wang C, Chen S, Yang JH, Lang L, Xiang HJ, Gong XG, et al. Design of I2-II-IV-VI4 semiconductors through element substitution: the thermodynamic stability limit and chemical trend. Chem Mater 2014;26:3411–7. https://doi.org/10.1021/cm500598x.
[251] Sai Gautam G, Senftle TP, Carter EA. Understanding the effects of Cd and Ag doping in Cu2ZnSnS4 solar cells. Chem Mater 2018. https://doi.org/10.1021/acs.chemmater.8b00677.
[252] Peelen Mary. Periodic table of the elements. Antioch Rev 2017. https://doi.org/10.7723/antiochreview.75.2.0169.
[253] Zhang Q, Deng H, Chen L, Yu L, Tao J, Sun L, et al. Cation substitution induced structural transition, band gap engineering and grain growth of Cu2CdxZn1−xSnS4thin films. J Alloys Compd 2017;695:482–8. https://doi.org/10.1016/j.jallcom.2016.11.121.
[254] Xiao ZY, Li YF, Yao B, Deng R, Ding ZH, Wu T, et al. Bandgap engineering of Cu2CdxZn1-xSnS 4 alloy for photovoltaic applications: a complementary experimental and first-principles study. J Appl Phys 2013. https://doi.org/10.1063/1.4829457.
[255] Chen R, Persson C. Electronic and optical properties of Cu2 X SnS4 (X = Be, Mg, Ca, Mn, Fe, and Ni) and the impact of native defect pairs. J Appl Phys 2017. https://doi.org/10.1063/1.4984115.
[256] Liang X, Guo P, Wang G, Deng R, Pan D, Wei X. Dilute magnetic semiconductor Cu2MnSnS4 nanocrystals with a novel zincblende and wurtzite structure. RSC Adv 2012. https://doi.org/10.1039/c2ra20198d.
[257] Chen L, Deng H, Tao J, Cao H, Huang L, Sun L, et al. Synthesis and characterization of earth-abundant Cu2MnSnS4 thin films using a non-toxic solution-based technique. RSC Adv 2015. https://doi.org/10.1039/c5ra14595c.
[258] Chen L, Deng H, Cui J, Tao J, Zhou W, Cao H, et al. Composition dependence of the structure and optical properties of Cu2MnxZn1-xSnS4 thin films. J Alloys Compd 2015. https://doi.org/10.1016/j.jallcom.2014.12.047.
[259] Lie S, Sandi MI, Tay YF, Li W, Tan JMR, Bishop DM, et al. Improving the charge separation and collection at the buffer/absorber interface by double-layered Mn-substituted CZTS. Sol Energy Mater Sol Cells 2018. https://doi.org/10.1016/j.solmat.2018.05.052.
[260] Li X, Hou Z, Gao S, Zeng Y, Ao J, Zhou Z, et al. Efficient optimization of the performance of Mn2+-doped kesterite solar cell: machine learning aided synthesis of high efficient Cu2(Mn,Zn)Sn(S,Se)4 solar cells. Sol RRL 2018. https://doi.org/10.1002/solr.201800198.
[261] Hall SR, Szymanski JT, Stewart JM. Kesterite, Cu2(Zn,Fe)SnS4 and Stannite Cu2(Fe,Zn)SnS4, structurally similar but distinct minerals. Can Mineral 1978.
[262] Kumar MS, Madhusudanan SP, Batabyal SK. Substitution of Zn in Earth-Abundant Cu2ZnSn(S,Se)4 based thin film solar cells – a status review. Sol Energy Mater Sol Cells 2018. https://doi.org/10.1016/j.solmat.2018.05.003.
[263] Meng X, Deng H, He J, Sun L, Yang P, Chu J. Synthesis, structure, optics and electrical properties of Cu2FeSnS4 thin film by sputtering metallic precursor combined with rapid thermal annealing sulfurization process. Mater Lett 2015. https://doi.org/10.1016/j.matlet.2015.03.046.
[264] Chatterjee S, Pal AJ. A solution approach to p-type Cu2FeSnS4 thin-films and pn-junction solar cells: role of electron selective materials on their performance. Sol Energy Mater Sol Cells 2017;160:233–40. https://doi.org/10.1016/j.solmat.2016.10.037.

[265] Shannon RD. Revised effective ionic radii and systematic studies of interatomie distances in halides and chaleogenides. Acta Crystallogr Sect A 1993.
[266] Kevin P, Malik MA, McAdams S, O'Brien P. Synthesis of nanoparticulate alloys of the composition Cu2Zn1-xFexSnS4: structural, optical, and magnetic properties. J Am Chem Soc 2015;137:15085–9. https://doi.org/10.1021/jacs.5b10281.
[267] Pianezzi F, Nishiwaki S, Kranz L, Sutter-Fella CM, Reinhard P, Bissig B, et al. Influence of Ni and Cr impurities on the electronic properties of Cu(In,Ga)Se2 thin film solar cells. Prog Photovoltaics Res Appl 2015. https://doi.org/10.1002/pip.2503.
[268] Eisenbarth T, Caballero R, Kaufmann CA, Eicke A, Unold T. Influence of iron on defect concentrations and device performance for Cu(In,Ga)Se 2 solar cells on stainless steel substrates. Prog Photovoltaics Res Appl 2012. https://doi.org/10.1002/pip.2260.
[269] Ghosh A, Thangavel R, Rajagopalan M. First-principles study of structural stability and optical properties of Cu2XSnY4 (X = Fe, Co, Ni; Y = S, Se) for photovoltaic applications. Energy Environ Focus 2014;3:142–51. https://doi.org/10.1166/eef.2014.1080.
[270] Rondiya S, Wadnerkar N, Jadhav Y, Jadkar S, Haram S, Kabir M. Structural, electronic, and optical properties of Cu2NiSnS4: a combined experimental and theoretical study toward photovoltaic applications. Chem Mater 2017. https://doi.org/10.1021/acs.chemmater.7b00149.
[271] Ghosh A, Chaudhary DK, Biswas A, Thangavel R, Udayabhanu G. Solution-processed Cu2XSnS4 (X = Fe, Co, Ni) photo-electrochemical and thin film solar cells on vertically grown ZnO nanorod arrays. RSC Adv 2016. https://doi.org/10.1039/c6ra24149b.
[272] Hages CJ, Levcenco S, Miskin CK, Alsmeier JH, Abou-Ras D, Wilks RG, et al. Improved performance of Ge-alloyed CZTGeSSe thin-film solar cells through control of elemental losses. Prog Photovolt Res Appl 2015;23:376–84. https://doi.org/10.1002/pip.2442.
[273] Kim S, Kim KM, Tampo H, Shibata H, Matsubara K, Niki S. Ge-incorporated Cu2ZnSnSe4 thin-film solar cells with efficiency greater than 10%. Sol Energy Mater Sol Cells 2016;144:488–92. https://doi.org/10.1016/j.solmat.2015.09.039.
[274] Kim S, Kim KM, Tampo H, Shibata H, Niki S. Improvement of voltage deficit of Ge-incorporated kesterite solar cell with 12.3% conversion efficiency. Appl Phys Express 2016;9. https://doi.org/10.7567/APEX.9.102301.
[275] González-Castillo JR, Pulgarín-Agudelo FA, Rodríguez-González E, Vigil-Galán O, Courel-Piedrahita M, Andrade-Arvizu JA. Influence of Ge content on Cu2Zn(SnGe)Se4 physical properties deposited by sequential thermal evaporation technique. Mater Sci Semicond Process 2018;83:96–101. https://doi.org/10.1016/j.mssp.2018.04.024.
[276] Redinger A, Berg DM, Dale PJ, Siebentritt S. The consequences of kesterite equilibria for efficient solar cells. J Am Chem Soc 2011. https://doi.org/10.1021/ja111713g.
[277] Grazman BL. Handbook of chemistry and physics: a ready-reference book of chemical and physical data. TrAC Trends Anal Chem 1991;10:8–9. https://doi.org/10.1016/0165-9936(91)80034-p.
[278] Litvinchuk AP, Dzhagan VM, Yukhymchuk VO, Valakh MY, Parasyuk OV, Piskach LV, et al. Crystal structure and vibrational properties of Cu2ZnSiSe4 quaternary semiconductor. Phys Status Solidi Basic Res 2016. https://doi.org/10.1002/pssb.201600175.
[279] Shu Q, Yang JH, Chen S, Huang B, Xiang H, Gong XG, et al. Cu2Zn(Sn,Ge)Se4 and Cu2Zn(Sn,Si)Se 4 alloys as photovoltaic materials: structural and electronic properties. Phys Rev B - Condens Matter Mater Phys 2013. https://doi.org/10.1103/PhysRevB.87.115208.
[280] Hamdi M, Lafond A, Guillot-Deudon C, Hlel F, Gargouri M, Jobic S. Crystal chemistry and optical investigations of the Cu2Zn(Sn,Si)S4series for photovoltaic applications. J Solid State Chem 2014. https://doi.org/10.1016/j.jssc.2014.08.030.
[281] Hadke SH, Levcenko S, Lie S, Hages CJ, Márquez JA, Unold T, et al. Synergistic effects of double cation substitution in solution-processed CZTS solar cells with over 10% efficiency. Adv Energy Mater 2018;8:1802540. https://doi.org/10.1002/aenm.201802540.
[282] Yang Y, Kang X, Huang L, Pan D. Tuning the band gap of Cu2ZnSn(S,Se)4 thin films via lithium alloying. ACS Appl Mater Interfaces 2016. https://doi.org/10.1021/acsami.5b11535.
[283] Dai X, Zhou A, Feng L, Wang Y, Xu J, Li J. Molybdenum thin films with low resistivity and superior adhesion deposited by radio-frequency magnetron sputtering at elevated temperature. Thin Solid Films 2014. https://doi.org/10.1016/j.tsf.2014.07.043.
[284] Wang SF, Yang HC, Liu CF, Bor HYY. Characteristics of bilayer molybdenum films deposited using Rf sputtering for back contact of thin film solar cells. Adv Mater Sci Eng 2014. https://doi.org/10.1155/2014/531401.
[285] Su CY, Liao KH, Pan CT, Peng PW. The effect of deposition parameters and post treatment on the electrical properties of Mo thin films. Thin Solid Films 2012. https://doi.org/10.1016/j.tsf.2012.05.027.
[286] Scragg JJ, Wätjen JT, Edoff M, Ericson T, Kubart T, Platzer-Björkman C. A detrimental reaction at the molybdenum back contact in Cu 2ZnSn(S,Se)4 thin-film solar cells. J Am Chem Soc 2012. https://doi.org/10.1021/ja308862n.
[287] Scragg JJ, Kubart T, Wätjen JT, Ericson T, Linnarsson MK, Platzer-Björkman C. Effects of back contact instability on Cu2ZnSnS4 devices and processes. Chem Mater 2013. https://doi.org/10.1021/cm4015223.
[288] Altamura G, Grenet L, Roger C, Roux F, Reita V, Fillon R, et al. Alternative back contacts in kesterite Cu2ZnSn(S 1-xSex)4 thin film solar cells. J Renew Sustain Energy 2014. https://doi.org/10.1063/1.4831781.
[289] Tong Z, Zhang K, Sun K, Yan C, Liu F, Jiang L, et al. Modification of absorber quality and Mo-back contact by a thin Bi intermediate layer for kesterite Cu2ZnSnS4 solar cells. Sol Energy Mater Sol Cells 2016. https://doi.org/10.1016/j.solmat.2015.09.066.
[290] Englund S, Grini S, Donzel-Gargand O, Paneta V, Kosyak V, Primetzhofer D, et al. TiN Interlayers with Varied Thickness in Cu2ZnSnS(e)4 Thin Film Solar Cells: effect on Na Diffusion, Back Contact Stability, and Performance. Phys Status Solidi Appl Mater Sci 2018. https://doi.org/10.1002/pssa.201800491.
[291] Cui H, Lee CY, Li W, Liu X, Wen X, Hao X. Improving efficiency of evaporated Cu2ZnSnS4 thin film solar cells by a thin ag intermediate layer between absorber and back contact. Int J Photoenergy 2015. https://doi.org/10.1155/2015/170507.
[292] Park J, Huang J, Sun K, Ouyang Z, Liu F, Yan C, et al. The effect of thermal evaporated MoO3 intermediate layer as primary back contact for kesterite Cu2ZnSnS4 solar cells. Thin Solid Films 2018. https://doi.org/10.1016/j.tsf.2018.01.012.
[293] Zhou F, Zeng F, Liu X, Liu F, Song N, Yan C, et al. Improvement of Jsc in a Cu2ZnSnS4 solar cell by using a thin carbon intermediate layer at the Cu2ZnSnS4/Mo interface. ACS Appl Mater Interfaces 2015;7:22868–73. https://doi.org/10.1021/acsami.5b05652.
[294] Haight R, Barkhouse A, Wang W, Luo Y, Shao X, Mitzi DB, et al. CdS and Cd-free buffer layers on solution phase grown

Cu 2ZnSn(SxSe1- x)4 :Band alignments and electronic structure determined with femtosecond ultraviolet photoelectron spectroscopy. Mater Res Soc Symp Proc 2014. https://doi.org/10.1557/opl.2014.196.

[295] Barkhouse DAR, Haight R, Sakai N, Hiroi H, Sugimoto H, Mitzi DB. Cd-free buffer layer materials on Cu2ZnSn(SxSe1-x)4: band alignments with ZnO , ZnS , and In2S3. Appl Phys Lett 2012.

[296] Khemiri N, Aousgi F, Kanzari M. Tunable optical and structural properties of Zn(S,O) thin films as Cd-free buffer layer in solar cells. Mater Lett 2017. https://doi.org/10.1016/j.matlet.2017.04.037.

[297] Nguyen M, Ernits K, Tai KF, Ng CF, Pramana SS, Sasangka WA, et al. ZnS buffer layer for Cu2ZnSn(SSe)4 monograin layer solar cell. Sol Energy 2015. https://doi.org/10.1016/j.solener.2014.11.006.

[298] Meng F, Dehouche Z, Ireland TG, Fern GR. Improved photovoltaic performance of monocrystalline silicon solar cell through luminescent down-converting Gd2O2S:Tb3+ phosphor. Prog Photovolt Res Appl 2019;27:640–51. https://doi.org/10.1002/pip.3139.

[299] Colegrove E, Yang JH, Harvey SP, Young MR, Burst JM, Duenow JN, et al. Experimental and theoretical comparison of Sb, As, and P diffusion mechanisms and doping in CdTe. J Phys D Appl Phys 2018;51:075102. https://doi.org/10.1088/1361-6463/aaa67e.

[300] Metzger WK, Grover S, Lu D, Colegrove E, Moseley J, Perkins CL, et al. Exceeding 20% efficiency with in situ group V doping in polycrystalline CdTe solar cells. Nat Energy 2019;4:837–45. https://doi.org/10.1038/s41560-019-0446-7.